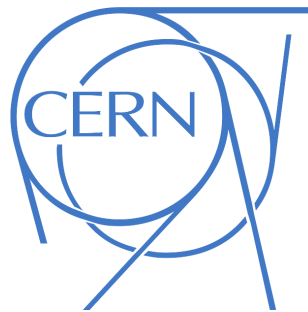


**POLITECNICO DI MILANO**  
Corso di Laurea Magistrale in Ingegneria Nucleare  
Dipartimento di Energia



# **OFF-MOMENTUM COLLIMATION AND CLEANING IN THE ENERGY RAMP IN THE LHC**

**Relatore:**

**Prof. Stefano Luigi Maria GIULINI CASTIGLIONI AGOSTEO**

**Correlatore:**

**Dott. Roderik BRUCE (CERN)**

**Tesi di Laurea di:**

**Elena QUARANTA**  
matr. 770342

**Anno Accademico 2012-2013**



*Alla tutta la mia famiglia...  
...è grazie ad ognuno di loro se sono arrivata fin qui!*



# Abstract

---

This Master thesis work has been carried out at CERN in the framework of the LHC (Large Hadron Collider) Collimation project.

The LHC is a two-beam proton collider, built to handle a stored energy of 360 MJ for each beam. Since the energy deposition from particle losses could quench the superconducting magnets, a system of collimators has been installed in two cleaning insertions in the ring and in the experimental areas. The achievable LHC beam intensity is directly coupled to the beam loss rate and, consequently, to the cleaning efficiency of the collimation system.

This study analyses the collimation cleaning performance in different scenarios inside the accelerator. First, simulations are performed of the transverse losses in the LHC collimation system during the acceleration process. The results are compared with data taken during a dedicated session at the LHC machine. Simulations are also performed to predict the collimation efficiency during future operation at higher energy.

Furthermore, an investigation of the effect of losses of protons, that have slowly lost energy through synchrotron radiation, is carried out. These protons eventually hit the momentum collimators, where the impact coordinates can be used as a starting point for future studies of radiation damage to nearby warm magnets.



# Abstract

(Italian version)

---

Il presente lavoro di tesi è stato condotto presso il Centro Europeo di Ricerca Nucleare CERN nell'ambito del progetto di collimazione per Large Hadron Collider (LHC).

LHC è un acceleratore circolare di due fasci di protoni, progettato per immagazzinare un'energia di 360 MJ prodotta da ciascuno dei due fasci. La deposizione di energia a seguito di perdita di particelle potrebbe indurre fenomeni di quench all'interno dei magneti superconduttori: un sistema di collimatori che ripulisca il fascio è stato quindi installato in due settori dell'anello e in prossimità degli esperimenti. L'intensità di fascio che LHC può raggiungere è strettamente correlata al tasso di perdita di particelle e, di conseguenza, all'efficienza di pulizia (cleaning) del sistema di collimazione.

In questo studio sono analizzate le prestazioni di cleaning dei collimatori in differenti scenari all'interno dell'acceleratore. Inizialmente sono illustrate simulazioni di perdite trasversali di particelle nel sistema di collimazione di LHC durante il processo di accelerazione. I risultati sono poi comparati con i dati prelevati direttamente dalla macchina durante dedicate sessioni di misura. Ulteriori simulazioni sono poi effettuate al fine di prevedere l'efficienza di collimazione per un futuro funzionamento della macchina a più alta energia.

Viene indagato, inoltre, l'effetto dovuto alla perdita di protoni che, a seguito dell'emissione di radiazione di sincrotrone, perdono lentamente energia. Essi alla fine arrivano a colpire i collimatori nella regione di "momentum cleaning" dell'acceleratore: la conoscenza delle coordinate d'impatto delle particelle costituisce il punto di partenza per studi futuri sul danneggiamento indotto da radiazione nelle zone limitrofe ai magneti non superconduttori in LHC



---

# Contents

---

<b>Abstract</b>	<b>i</b>
<b>Abstract (Italian version)</b>	<b>iii</b>
<b>1 Introduction</b>	<b>1</b>
<b>2 Accelerator and Collimation Theory</b>	<b>5</b>
2.1 Basic elements of accelerator beam dynamics . . . . .	5
2.1.1 Betatron oscillations . . . . .	6
2.1.2 Synchrotron oscillations . . . . .	11
2.1.3 Dispersion . . . . .	17
2.2 Beam halo and collimation . . . . .	17
2.2.1 Machine aperture . . . . .	18
2.2.2 Generation of beam halo . . . . .	19
2.2.3 Collimation cleaning performance . . . . .	20
2.2.4 Beam losses and interaction with collimator materials	22
<b>3 The CERN Large Hadron Collider</b>	<b>25</b>
3.1 Overview of the LHC: accelerator chain, experiments and performance . . . . .	25
3.2 The LHC collimation system . . . . .	29
3.2.1 General design of a LHC collimator . . . . .	30
3.2.2 The multi-stage LHC collimation system . . . . .	31
3.2.3 Towards the future of LHC collimation system . . . . .	38
<b>4 SixTrack Simulation Setup for Cleaning Inefficiency Studies</b>	<b>39</b>
4.1 SixTrack for collimation . . . . .	39
4.1.1 Particle tracking . . . . .	39
4.1.2 Sixtrack input files . . . . .	40
4.1.3 Sixtrack output files and post processing . . . . .	42
4.2 Cleaning inefficiency and beam loss maps . . . . .	44
4.3 Benchmarks of SixTrack code . . . . .	46
<b>5 Collimation Cleaning Performance in the LHC Energy Ramp</b>	<b>51</b>
5.1 SixTrack simulatios: setup and procedure . . . . .	51
5.1.1 Energy and Collimator Setting Changing . . . . .	51
5.1.2 Collimator Positions Changing Only . . . . .	58
5.1.3 Energy Changing Only . . . . .	58

---

CONTENTS

---

5.2	Beam loss measurements in the LHC energy ramp . . . . .	62
5.3	Looking towards 7 TeV scenario after LS1 . . . . .	68
<b>6</b>	<b>Simulation of Off-Momentum Cleaning in IR3 Insertion</b>	<b>73</b>
6.1	Synchrotron motion in the LHC: basic check of longitudinal particle motion in SixTrack . . . . .	73
6.2	Off-momentum simulation setup for 7 TeV scenario . . . . .	75
6.3	Main results . . . . .	77
6.3.1	Particle loss distribution in the ring . . . . .	77
6.3.2	Particles distribution in the IR3 TCP jaw . . . . .	77
6.3.3	Choice of the initial $\delta$ distribution . . . . .	80
6.4	Further studies . . . . .	82
<b>7</b>	<b>Conclusions</b>	<b>91</b>
	<b>Bibliography</b>	<b>IV</b>
	<b>Appendix A</b>	<b>V</b>
	<b>Appendix B</b>	<b>XIII</b>
	<b>Acknowledgement</b>	

---

---

# List of Figures

---

2.1	Right-handed moving reference system. . . . .	6
2.2	The phase space ellipse of particle motion in the $x$ - $x'$ plane. . . . .	9
2.3	Energy variation of two circulating particles passing by the RF cavity. . . . .	12
2.4	Relative motion of A and B in the longitudinal phase space. . . . .	12
2.5	Motion of particle inside and outside the bucket limit. . . . .	15
2.6	Mechanical pendulum motion. . . . .	15
2.7	RF potential well in the longitudinal phase space. . . . .	16
2.8	The phase space ellipse in the $x$ - $x'$ plane of a particle with momentum offset $\delta$ . . . . .	18
2.9	Geometrical and dynamic aperture in an accelerator. . . . .	19
2.10	Inner view of two collimator jaws. . . . .	21
3.1	CERN site in Geneva area. . . . .	26
3.2	LHC injectors chain, for proton and ion run. . . . .	27
3.3	Layout of the LHC. . . . .	29
3.4	Scheme of the LHC collimator. . . . .	30
3.5	Top view of an opened collimator. . . . .	31
3.6	Top view of a carbon-carbon jaw. . . . .	32
3.7	Sketch of the multi-stage collimation system to intercept the different halo types. . . . .	33
3.8	General layout of the LHC collimation system. . . . .	34
3.9	Azimuthal angle $\psi$ for skew collimators. . . . .	35
3.10	Example of collimators position in IR7. . . . .	36
4.1	The thin lens formalism. . . . .	40
4.2	Particle tracking parameters definition. Extract from <i>fort.3</i> . . . . .	41
4.3	Input to the SixTrack collimation routine. Extract from <i>fort.3</i> . . . . .	42
4.4	Particle distribution in different spaces . . . . .	43
4.5	Example of a trajectory of a particle lost in IR8 in the LHC. . . . .	44
4.6	SixTrack simulation path. . . . .	45
4.7	Simulated beam loss map at 4 TeV for Beam 1 in the horizontal plane. . . . .	47
4.8	Measured and simulated SPS Beam Loss responses along the full ring. . . . .	48
4.9	Simulated beam losses from SixTrack (top) and measured BLM signals on April 2011 (bottom). . . . .	49
4.10	Comparison of proton losses on horizontal and vertical TCTs respect to the TCPs between measurements in 2011 and SixTrack simulations, including and not including FLUKA results. . . . .	50

---

LIST OF FIGURES

---

5.1	Collimator settings during the energy ramp. . . . .	52
5.2	Simulated beam loss map at 2 TeV for Beam 1 in the horizontal plane. . . . .	54
5.3	Highest local cleaning inefficiency in the cold parts of the machine, found in the IR7 DS, as function of energy. In the SixTrack simulation, $6.4 \times 10^6$ particles were tracked. . . . .	55
5.4	Highest local cleaning inefficiency in the cold parts of the machine, found in the IR7 DS, as function of energy. In the SixTrack simulation, $64 \times 10^6$ particles were tracked. . . . .	55
5.5	Average impact parameter $b$ on the horizontal TCP as function of energy from SixTrack simulations done using the settings shown in Table 5.1 . . . . .	56
5.6	Distribution of the impact parameter $b$ along the IR7 TCP at 450 GeV and 4 TeV. . . . .	56
5.7	Distribution of the impact parameter $b$ along the IR7 TCP at 450 GeV (halo smear: $0.0015 \sigma$ ) and at 4 TeV (halo smear: $0.4957 \sigma$ ). . . . .	57
5.8	Simulated beam loss map at 4 TeV for Beam 1 in the horizontal plane with different halo smear parameter. . . . .	59
5.9	Cleaning inefficiency at IR7 DS (Q8) during the energy ramp with standard simulations shown in Fig. 5.3 (blue) and keeping the energy constant but the collimators moving like in a normal ramp (green) . . . . .	60
5.10	Cleaning inefficiency at IR7 DS (Q8) during the energy ramp with standard simulations (blue) shown in Fig. 5.3 and keeping collimator half-gap in mm constant but the energy changing (red). . . . .	61
5.11	Comparison of cleaning inefficiency at IR7 DS (Q8) during the energy ramp in different simulated conditions. . . . .	61
5.12	Inside of one ionisation chamber of the LHC BLM system . . . . .	62
5.13	Beam loss map at 2 TeV from BLMs signal taken in the LHC in October 2012. . . . .	63
5.14	Beam intensity as function of time during the ADT excitations in the energy ramp. . . . .	64
5.15	Signal from selected BLMs during the energy ramp for Beam 1. . . . .	65
5.16	Comparison between loss map at 2 TeV from BLMs data taken in the LHC in November 2012 and SixTrack simulations. . . . .	66
5.17	Cleaning inefficiency for selected collimators in the energy ramp: measurements and simulation compared. . . . .	67
5.18	Cleaning inefficiency in the IR7 DS (Q8) as function of energy up to 7 TeV. . . . .	70

---

---

5.19	Simulated beam loss maps for two possible 7 TeV scenarios. . . . .	71
5.20	Cleaning inefficiency for selected collimators in the energy ramp up to 7 TeV: measurements and simulation compared. . . . .	72
6.1	Longitudinal phase space motion from analytical formula and SixTrack simulations, without radiation damping. . . . .	74
6.2	Uniform distribution assumed for the initial energy offset $\delta$ . . . . .	76
6.3	Beam loss map from SixTrack simulations at 7 TeV with synchrotron radiation effect. . . . .	78
6.4	Distribution of the turn when the first hit at IR3 TCP occurs. . . . .	79
6.5	Distribution of the longitudinal position along IR3 TCP jaw where the first impact occurs. . . . .	79
6.6	Distribution of the impact parameter in IR3 TCP jaw. . . . .	80
6.7	Distribution of the impact angle in IR3 TCP jaw. . . . .	80
6.8	Density plot of coordinates of particle inelastic interactions as function of longitudinal coordinate in IR3 TCP right jaw. . . . .	81
6.9	Correlation between the initial energy offset $\delta$ and the impact parameter $b$ at IR3 TCP. . . . .	82
6.10	Correlation between the initial energy offset $\delta$ and the impact angle at IR3 TCP. . . . .	83
6.11	Beam loss map from SixTrack simulations at 7 TeV with synchrotron radiation effect (faster simulations). Statistics: $9.5 \times 10^6$ particles. . . . .	84
6.12	Distribution of the turn when the first hit at IR3 TCP occurs (faster simulations). . . . .	85
6.13	Distribution of the longitudinal position along IR3 TCP jaw where the first impact occurs (faster simulations). . . . .	86
6.14	Distribution of the impact parameter in IR3 TCP jaw (faster simulations). . . . .	86
6.15	Distribution of the impact angle in IR3 TCP jaw (faster simulations). . . . .	87
6.16	Density plot of particle impact parameter as function of longitudinal coordinate in IR3 TCP right jaw (faster simulations). . . . .	88
6.17	Correlation between the initial energy offset $\delta$ and the impact parameter $b$ at IR3 TCP (faster simulations). . . . .	89
6.18	Correlation between the initial energy offset $\delta$ and the impact angle at IR3 TCP (faster simulations). . . . .	89
7.1	Simulated beam loss map at 450 GeV for Beam 1 in the horizontal plane. . . . .	V
7.2	Simulated beam loss map at 1 TeV for Beam 1 in the horizontal plane. . . . .	VI
7.3	Simulated beam loss map at 1.5 TeV for Beam 1 in the horizontal plane. . . . .	VII

---

LIST OF FIGURES

---

7.4	Simulated beam loss map at 2 TeV for Beam 1 in the horizontal plane. . . . .	VIII
7.5	Simulated beam loss map at 2.5 TeV for Beam 1 in the horizontal plane. . . . .	IX
7.6	Simulated beam loss map at 3 TeV for Beam 1 in the horizontal plane. . . . .	X
7.7	Simulated beam loss map at 3.5 TeV for Beam 1 in the horizontal plane. . . . .	XI
7.8	Simulated beam loss map at 4 TeV for Beam 1 in the horizontal plane. . . . .	XII
7.9	Measured beam loss map at 450 GeV for Beam 1 in the horizontal plane. . . . .	XIII
7.10	Measured beam loss map at 1 TeV for Beam 1 in the horizontal plane. . . . .	XIV
7.11	Measured beam loss map at 1.5 TeV for Beam 1 in the horizontal plane. . . . .	XIV
7.12	Measured beam loss map at 2 TeV for Beam 1 in the horizontal plane. . . . .	XV
7.13	Measured beam loss map at 2.5 TeV for Beam 1 in the horizontal plane. . . . .	XV
7.14	Measured beam loss map at 3 TeV for Beam 1 in the horizontal plane. . . . .	XVI
7.15	Measured beam loss map at 3.5 TeV for Beam 1 in the horizontal plane. . . . .	XVI
7.16	Measured beam loss map at 4 TeV for Beam 1 in the horizontal plane. . . . .	XVII

---

---

# List of Tables

---

3.1	LHC main parameters. . . . .	28
3.2	Collimator settings for the different families in the cleaning hierarchy. . . . .	37
3.3	Collimator settings of the TCTs during injection, flat top and squeeze. . . . .	37
5.1	Collimator settings used in SixTrack simulations. . . . .	52
5.2	Main parameters of the LHC ionization chambers. . . . .	63
5.3	Comparison between collimator half-gaps at injection, 4 TeV (2012 settings) and 7 TeV (nominal and relaxed settings). . .	69
6.1	Main parameters used for SixTrack simulation. . . . .	76
6.2	Impact angle at TCP.6L3.B1 at 7 TeV. . . . .	81

---

## LIST OF TABLES

---

---

# 1

## Introduction

---

Particle collisions allow scientists to study the fundamental forces of nature. The higher the energy of the colliding beams and the higher the event rate, the wider is the spectrum of the generated particles that can be observed. Machines, called particle colliders, are used to create particle collisions in a controlled environment.

The world's largest and highest energy particle accelerator ever built is the Large Hadron Collider (LHC) [1] at CERN. It is designed to accelerate and store proton beams with energies up to 7 TeV and bring them into collision in experimental detectors. It was commissioned by the European Organization for Nuclear Research (CERN) in collaboration with more than 10000 scientists and engineers from over 100 countries and hundreds of universities and laboratories; the construction of this accelerator lasted from 1998 to 2008. The LHC is designed to accelerate two counterrotating beams of  $3.2 \times 10^{14}$  protons or  $4.1 \times 10^{10}$  lead ions up to 7 TeV and 574 TeV respectively. Consequently, it can handle a stored energy of 360 MJ for each proton beam in the nominal scenario.

To bend and focus the circulating high-energy beams, superconducting (SC) magnets are placed around the ring. They require a low-temperature environment (between 1.8 K and 4.5 K) and if the magnets are heated and leave their superconducting state, a so-called quench occurs. Such a heating could be induced by local beam losses of  $4 \times 10^7$  protons at 7 TeV with an energy deposited of  $30 \text{ mJ cm}^3$  into the superconducting coils.

In order to prevent that unavoidable beam losses bring the magnets to the quench limits, a sophisticated system of collimators [1, 2, 3] is needed to provide beam cleaning and passive machine protection. LHC collimators consist of two parallel, fully movable jaws of special materials. The two jaws define a gap for free passage of the beam core. The particles in the beam tails are intercepted and cleaned by the jaw material to prevent them from being lost somewhere in the magnets.

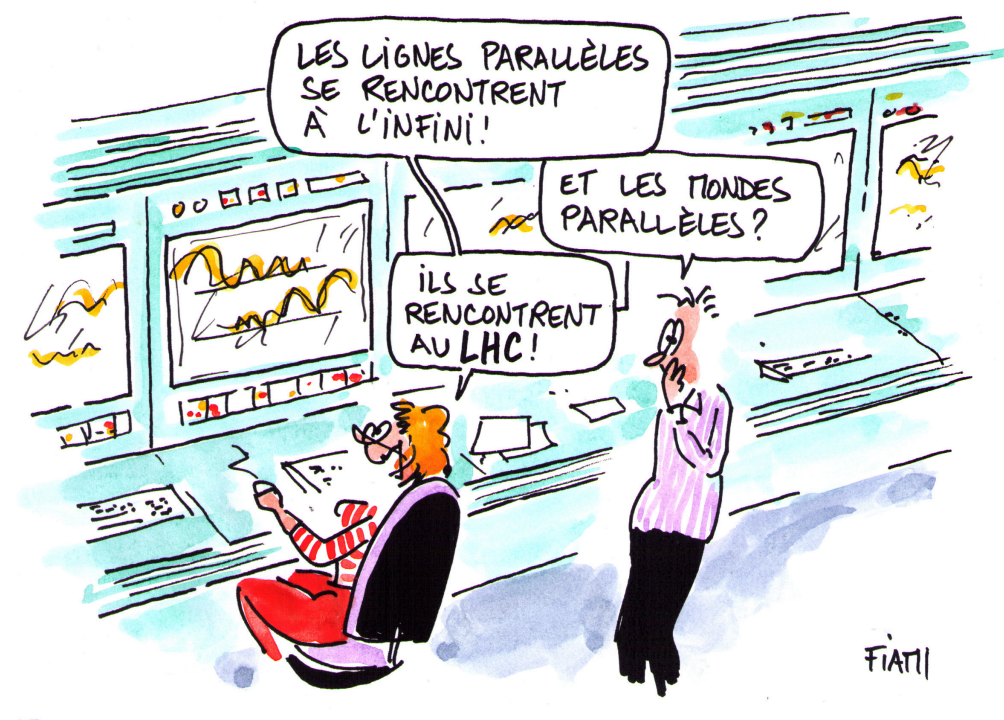
Two insertions in the LHC ring are dedicated to host this system: in the first interaction region, labelled IR3, collimators are used for the cleaning of off-momentum particles and the second one, named IR7, intercepts particles with too large transverse oscillation amplitudes.

The design goal of the system is not only to avoid quenches of SC magnets but also to protect other equipment in the ring from radiation damage

and minimize the background in the LHC experiments. The cleaning performance of the collimation system is expressed by the *cleaning efficiency*. This parameter refers to the fraction of particles that hit a primary collimator and are stopped in the cleaning insertion. For the 7 TeV protons the cleaning efficiency must be above 99.99%.

This work describes studies of the collimator performance in different operating conditions of the LHC machine. A simulation code, SixTrack [4], has been used to simulate the particle motion in the LHC and extract information about the cleaning performance of the collimation system. The results will help in benchmarking the energy dependence of the simulated inefficiency in SixTrack to predict the collimator performance at higher energy configurations. Moreover, studies of losses in IR3 of protons that have lost energy through synchrotron radiation have been carried out, based on a new modified version of the SixTrack code. The results will be provided as input for further energy deposition and radiation studies on magnets and collimator jaws and can also be used as a starting point for other future applications.

To have a better understanding of the topics covered in the thesis, three chapters are dedicated to the explanation of some important concepts: Chapter 2 reviews basic principles of particle beam dynamics, focusing on transversal and longitudinal motion, a brief introduction of the LHC and its collimation system is given in Chapter 3 and finally the main parameters for SixTrack code setup, used to simulate the particles tracking into the ring for the aims of this study, is the aim of Chapter 4. Then, the cleaning performance of the LHC collimation system is discussed more in detail starting from Chapter 5. Here the cleaning inefficiency at intermediate energies, from injection to 2012 top energy is analysed: simulation results and measured provoked loss in the machine are compared. Additional simulations are shown for the extrapolation of the performance of the collimation system up to nominal 7 TeV. Chapter 6 investigates, instead, the cleaning efficiency for off-momentum particles in the IR3 insertion, an aspect not extensively studied so far. Results are presented of SixTrack simulations, performed at 7 TeV taking into account the energy lost turn by turn due to synchrotron radiation by the protons.





## 2

# Accelerator and Collimation Theory

---

Particles are held in a storage ring by the combined effect of the forces from electrical and magnetic fields. The particle motion either in the transverse plane (horizontal and vertical) and in the longitudinal plane is discussed in the first part of this chapter, according to the main principles of beam dynamics. To simplify the study, a linear approximation is assumed of the magnetic field that guides the particles in their designed trajectories. Several processes, ranging from slow diffusion to fast scattering events, cause particles to deviate from the wanted trajectory and energy. These particles, called *halo*, risk to hit the aperture of the machine releasing their energy there. Thus, an efficient collimation system that intercepts the halo particles is required. Some general characteristics of the collimators are in the focus of the second part of the chapter.

## 2.1 Basic elements of accelerator beam dynamics

The electrical and magnetic fields are the essential ingredients that allow particles to move inside an accelerator. The former is generated by a Radio Frequency (RF) system, in which a sinusoidal potential is applied to resonant cavities. This system provides the energy to accelerate the particles in addition to the fraction needed to compensate the energy lost through synchrotron radiation. Since the RF cavity is a resonating structure at a specific RF frequency, there will be standing waves generated within this cavity. These standing wave 'pockets' are the RF buckets. When beam is captured by the RF system, it is contained in the buckets, inside which particles are grouped in bunches.

In addition, several orders of magnetic fields can be identified: dipoles, quadrupoles, sextupoles, octupoles and so on. Dipole magnets bend charged particles and define the ideal machine a closed orbit on which a proton can move infinitely. The quadrupoles instead, focus the circulating beam around the closed orbit, as an optical lens does with the rays of the sun. The energy and the arrival point of the protons inside these magnets have a

strong impact on the particle focusing, defocusing and deflection: there are the chromaticity effect. Higher order magnets, like sextupoles and octupoles, are installed in the accelerator to correct these effects.

On a particle circulating in the ring, a Lorentz force acts, given by:

$$\frac{d\vec{p}}{dt} = q(\vec{E} + \vec{v} \wedge \vec{B}), \quad (2.1)$$

where  $\vec{p}$  is the relativistic momentum,  $q$  and  $\vec{v}$  are the charge and the velocity of the particle,  $\vec{E}$  and  $\vec{B}$  refer respectively to the electrical and the magnetic acting on the proton. The Lorentz force is applied as bending force to guide the particle along the design orbit which in principle all particles should follow but from which most of them will unavoidably deviate.

In the next sections the transverse and longitudinal particle motion will be discussed separately.

### 2.1.1 Betatron oscillations

In this section, we are interested in the transverse motion[5, 6, 7, 8] of a charged particle in a circular accelerator in steady state, that means not in injecting, extracting or accelerating conditions.

Using a fixed and right-handed Cartesian reference system[5] it would be difficult to express deviations of individual particle trajectories from the design orbit. Because of that, it is more useful to introduce a right-handed orthogonal and moving system  $(x, y, s)$ , as Fig. 2.1 shows, that follows an ideal particle travelling along the design orbit. The blue line represents the ideal orbit and the black arrow  $r_0$  shows the orbital radius. The red arrow labelled  $s$  is the tangential vector to that orbit,  $x$  and  $y$  are respectively the horizontal and vertical position of the particle relative to the orbit.

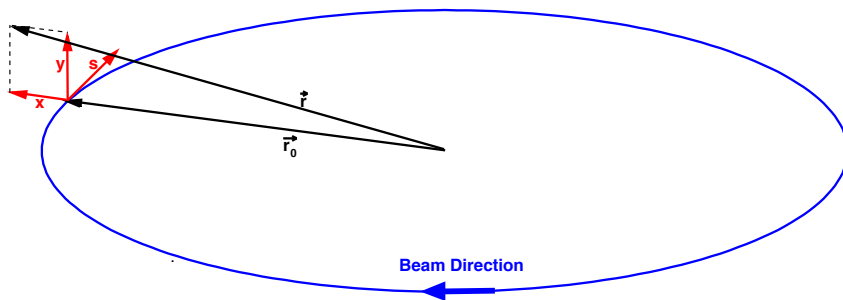


Figure 2.1: Right-handed moving reference system.

In the following, we briefly discuss the derivation of the general equation of particle motion in the transverse plane related to the design orbit using

the moving coordinate system. Since  $\vec{E} = 0$  in transverse linear dynamics, it has been neglected in the following discussion and, in Eq. 2.1, only the magnetic field  $\vec{B}$  will be taken into account.

Vertical and orthogonal dipoles force protons to curve in the horizontal plane with a local bending radius equal to:

$$\varrho = \frac{p}{qB}. \quad (2.2)$$

From that, the definition of the *magnetic rigidity*  $R$  can be derived:

$$R = B\varrho = \frac{p}{q}. \quad (2.3)$$

As the particle travels through the magnet structure, its path length  $s$  along the ideal trajectory is uniquely defined for any time  $t$ . This allows to make a transformation in Eq. 2.1 from the independent variable  $t$  to the  $s$  coordinate [8]. In a particle accelerator, usually only the transverse components of the magnetic field are non-zero, i.e.  $\vec{B} = (B_x, B_y, 0)$ . If  $B_{x,y}$  are the components of the magnetic field along  $x$  and  $y$ , from small deviations from the design orbit they may be expanded in series to the first order [5]:

$$B_x(x, y, s) = B_{x0} + \frac{\partial B_x}{\partial x} x + \frac{\partial B_x}{\partial y} y, \quad (2.4)$$

$$B_y(x, y, s) = B_{y0} + \frac{\partial B_y}{\partial x} x + \frac{\partial B_y}{\partial y} y, \quad (2.5)$$

From the Maxwell equations we also know that:

$$\frac{\partial B_x}{\partial x} = -\frac{\partial B_y}{\partial y}, \quad \frac{\partial B_y}{\partial x} = \frac{\partial B_x}{\partial y} \quad (2.6)$$

Since the particle is bent only in the horizontal plane by a constant vertical field,  $B_{x0} = 0$  and  $\frac{\partial B_y}{\partial y} = 0$ . Moreover we also assume no skew quadrupolar fields ( $\frac{\partial B_x}{\partial x} = 0$ ), then Eq. 2.4 and Eq. 2.5 become [5]:

$$B_x = \frac{\partial B_y}{\partial x} y = B_1 y, \quad (2.7)$$

$$B_y = -B_0 + \frac{\partial B_y}{\partial x} x = -B_0 + B_1 x, \quad (2.8)$$

where  $B_0$  and  $B_1$  are the coefficients of dipole and quadrupole respectively. Furthermore, we consider only particles with design momentum (for linear expansion in momentum see Section 2.1.3) and we retain only linear terms

in  $x, x', y, y'$ . Taking into account all these assumptions, the so-called *Hill's equations* for the transverse motion are given by[5] :

$$x'' + K_x(s)x = 0, \quad K_x(s) = \frac{1}{\varrho(s)^2} - \frac{B_1(s)}{B\varrho(s)} = \frac{1}{\varrho(s)^2} + K_y(s) \quad (2.9)$$

$$y'' - K_y(s)y = 0, \quad K_y(s) = -\frac{B_1(s)}{B\varrho(s)} \quad (2.10)$$

Inside a magnetic element,  $\varrho(s)$  and  $K_y(s)$  can be considered constant in  $s$ , so the solution of Eq. 2.9 and 2.10 gives respectively an harmonic oscillator or an exponential function depending on the sign of  $K_y$ . In the whole accelerator, the general solution of Hill's equation along  $x$ , assuming  $\varrho(s)$  and  $K_y(s)$  piecewise constant functions with the same periodicity as the lattice, is [7]:

$$x(s) = A\sqrt{\beta_x(s)} \cos(\varphi_x(s) + \varphi_0). \quad (2.11)$$

$\beta_x(s)$  is a periodic function, known as betatron function, that modulates the amplitude of the oscillation in the transversal plane, i.e. *betatron oscillations*,  $\varphi_0$  is an arbitrary constant phase, which can be considered as an integration constant, and  $\varphi_x(s)$  is the phase advance, given by:

$$\varphi(s) = \int_0^s \frac{ds'}{\beta(s')}. \quad (2.12)$$

$A$  is an integration constant referred to the oscillation amplitude of a single particle. A different value of  $A$  characterizes each particle of the beam and its square root is commonly called single-particle emittance  $\epsilon_x$ . Then, Eq. 2.11 can be re-written as:

$$x(s) = \sqrt{\epsilon_x \beta_x(s)} \cos(\varphi_x(s) + \varphi_0). \quad (2.13)$$

Therefore, as a particle travels around a ring, its motion is a kind of distorted cosine-like trajectory with a varying amplitude  $\epsilon_x \sqrt{\beta_x(s)}$ , which is modulated in proportion to the root of the betatron function, and with a phase  $\varphi_x(s) + \varphi_0$  which advances with  $s$  at a varying rate proportional to  $1/\beta$ .

We can define some quantities related to the  $\beta$  function [8]:

$$\alpha(s) = -\frac{\beta'(s)}{2} \quad (2.14)$$

$$\gamma = \frac{1 + \alpha(s)^2}{\beta(s)}. \quad (2.15)$$

$\alpha(s)$ ,  $\beta(s)$  and  $\gamma(s)$  as called *Twiss parameters* and they completely define the machine optics.

Using these parameters, the single-particle emittance can be seen as the quantity that satisfies the following equation [8]:

$$\epsilon_x = \gamma x^2 + 2\alpha x x' + \beta x'^2. \quad (2.16)$$

Eq. 2.16 is the general equation of an ellipse, describing the particle motion in the  $x$ - $x'$  phase space plane (see Fig. 2.2). For the full set of particles composing the beam, a statistical quantity  $\epsilon$  can be defined: it represents the so-called geometrical beam emittance, i.e. the rms value of the single-particle emittances. The emittance  $\epsilon$  has now a more physical interpretation:  $\epsilon^2$ , to within a factor  $\pi$ , is the area of this phase ellipse.

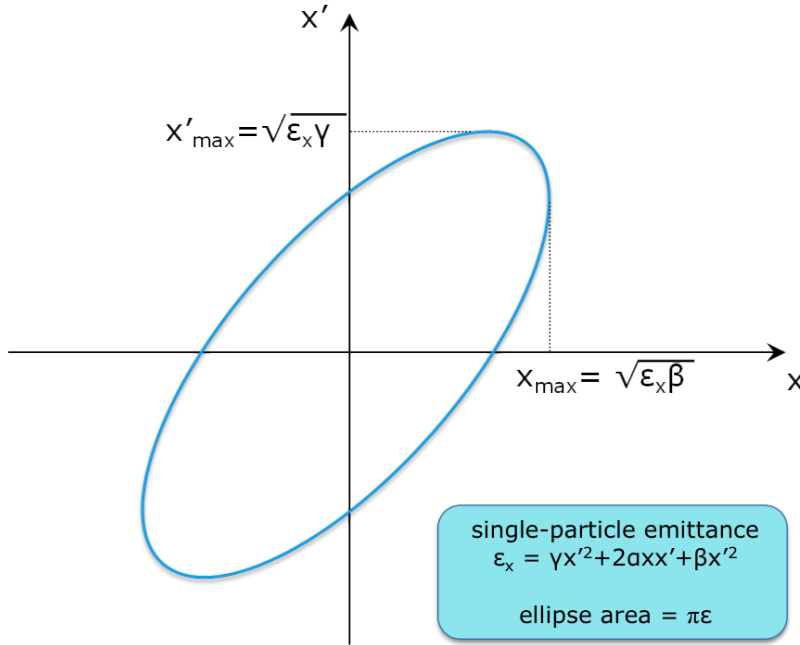


Figure 2.2: The phase space ellipse of particle motion in the  $x$ - $x'$  plane.

One other important feature that comes from Eq. 2.13 is that at each  $s$  position in the machine, the displacement  $x$  of the circulating particle lies always below a limit value  $X(s)$  obtained by setting  $\cos(\varphi_x(s) + \varphi_0) = 1$ , then [8]:

$$X(s) = \sqrt{\epsilon_x \beta_x(s)} \quad (2.17)$$

The complete trajectory of a particle will fall within an envelope defined by  $\pm X(s)$ .

Statistically, a bunch can often be represented as a Gaussian distribution of particles in the transversal plane of the phase space. Hence, using the emittance definition, the rms betatronic beam size  $\sigma(s)$  can be expressed [5]:

$$\sigma(s) = \sqrt{\epsilon \beta(s)} \quad (2.18)$$

In particular,  $\sigma(s)$  includes at each  $s$  the 66.6% of the circulating particles. Therefore, with good approximation a Gaussian distribution inside the  $3\sigma(s)$  can be identified. This part usually represents the *core* of the beam, while the remaining tails create the beam *halo*.

The number of betatron oscillations in one machine revolution, that means the number of turns in the phase space performed by a proton in one complete turn around the machine, is the *tune*. It mainly depends from the quadrupoles and is mathematically defined as:

$$Q_x = \frac{1}{2\pi} \varphi(C) = \frac{1}{2\pi} \int_{s_0}^{s_0+C} \frac{ds}{\beta(s)} \quad (2.19)$$

At some fixed value  $s_0$ , since  $\beta(s)$  is periodic, the amplitude in Eq. 2.13 will be constant ( $\sqrt{\epsilon_x \beta_x(s_0)}$ ). The only variable changing is the phase  $\varphi_x$ , which increases by  $2\pi Q_x$  on every turn. As said, the motion in  $x$  resembles a harmonic oscillation. If  $Q_x$  were an integer, the motion in Eq. 2.13 would be periodic and  $x(s_0)$  would have the same value on every revolution. In that case, any imperfections in the magnetic field around the ring act as perturbations, which are synchronous with the oscillation frequency. This will excite resonances, causing an increasing amplitude and unstable motion provoking a consequent loss of the beam. Therefore, integer values of the tune must be avoided. Similarly, resonances appear also for rational fractions. Thus, it is preferred that the tune is an irrational to avoid resonances that would make the machine unstable .

Now all the main ingredients to introduce the transport matrix have been presented. This matrix allows, known  $x$  and  $x'$  of a particle in any point of the machine, to calculate their value in all the other points of the accelerator. To get the matrix to transport particles from  $s_1$ , where  $x$  and  $x'$  are assumed to be known, to a downstream location  $s_2$ , we firstly rewrite Eq. 2.11 as the following:

$$x(s) = a\sqrt{\beta(s)} \sin(\varphi(s)) + b\sqrt{\beta(s)} \cos(\varphi(s)). \quad (2.20)$$

The coefficients  $a$  and  $b$  can be expressed as function of  $x$  and  $x'$ :

$$a = x(s_1) \left[ \frac{\sin(\varphi(s_1)) - \alpha(s_1) \cos(\varphi(s_1))}{\sqrt{\beta(s_1)}} \right] + x'(s_1) \sqrt{\beta(s_1)} \cos(\varphi(s_1)) \quad (2.21)$$

$$b = x(s_1) \left[ \frac{\cos(\varphi(s_1)) - \alpha(s_1) \sin(\varphi(s_1))}{\sqrt{\beta(s_1)}} \right] - x'(s_1) \sqrt{\beta(s_1)} \sin(\varphi(s_1)) \quad (2.22)$$

Replacing (2.21) and (2.22) in Eq. 2.20, we can write the solution for  $x(s_2)$  and  $x'(s_2)$  in matrix form as:

$$\begin{pmatrix} x(s_2) \\ x'(s_2) \end{pmatrix} = M(s_1|s_2) \begin{pmatrix} x(s_1) \\ x'(s_1) \end{pmatrix} \quad (2.23)$$

where:

$$M(s_1|s_2) = \begin{pmatrix} \sqrt{\frac{\beta_2}{\beta_1}}(\cos \varphi_{21} + \alpha_1 \sin \varphi_{21}) & \sqrt{\beta_2 \beta_1} \sin \varphi_{21} \\ -\frac{1+\alpha_1 \alpha_2}{\sqrt{\beta_2 \beta_1}} \sin \varphi_{21} + \frac{\alpha_1 - \alpha_2}{\sqrt{\beta_2 \beta_1}} \cos \varphi_{21} & \sqrt{\frac{\beta_1}{\beta_2}}(\cos \varphi_{21} - \alpha_2 \sin \varphi_{21}) \end{pmatrix}, \quad (2.24)$$

where the subscripts 1 and 2 indicate the Twiss parameters in  $s_1$  and  $s_2$ , while  $\varphi_{21}$  is the phase advance between the two points in the machine. Consequently, it can be immediately demonstrated that:

$$M(s_3|s_1) = M(s_3|s_2)M(s_2|s_1) \quad (2.25)$$

Eq. 2.24 is known as *Transport Matrix*. What has been said so far is strictly valid only for particles with nominal momentum  $p_0$ , which are called *on-momentum*.

### 2.1.2 Synchrotron oscillations

As already said at the beginning of this chapter, to accelerate the beam and reach the nominal energy a longitudinal electric field is needed. Magnetic fields cause deflections to the particle trajectory but they do not change the particle momentum. So a longitudinal sinusoidal voltage is applied across isolated gaps (RF cavities) to the passing beam. The RF frequency is an integer multiple of the revolution frequency in the ring:

$$f_{RF} = h f_{REV} \quad (2.26)$$

where  $h$  is called the harmonic number. A *synchronous particle* will circulate forever on the design orbit, always passing the RF at the same phase without changing its energy. All the other protons in the accelerator will oscillate in energy and in  $s$  around the synchronous particles under the influence of the RF system. This means that instead of being spread uniformly around the circumference of the accelerator the particles get "clumped" around the synchronous particle in bunch inside the RF bucket.

To qualitatively explain the oscillations the particles perform, we consider two particles: particle A, which is synchronous with the RF voltage and a second one, particle B, whose momentum is slightly higher than A's. In Fig. 2.3, particle A always passes through the cavity when there is no RF voltage (neither accelerating nor decelerating), assuming to neglect the radiation damping effect. Particle B, instead, arrives at the same time as A but with a higher energy, therefore on the second turn it arrives later than A and sees a decelerating RF voltage, which reduces its energy to exactly that of A. On the third turn it still arrives later than A as it has exactly the same energy/frequency, B is decelerated still more and now has a lower

energy than A. On the fourth turn B now arrives at the same time as A, as its energy is lower and its revolution frequency is higher, so B sees no acceleration or deceleration and is still at a lower energy than A. On the fifth turn B now arrives before A and sees an accelerating voltage, which means it now has the same energy and revolution frequency as A again. In the sixth turn B still arrives before A and is accelerated again. Now B has a higher energy and a lower revolution frequency than A. At the last turn B arrives at the same time as A but with a higher energy. This is just the situation that we had at the beginning. These oscillations are called *synchrotron oscillations*. Fig. 2.4 shows the motion of the two particles in the longitudinal phase space.

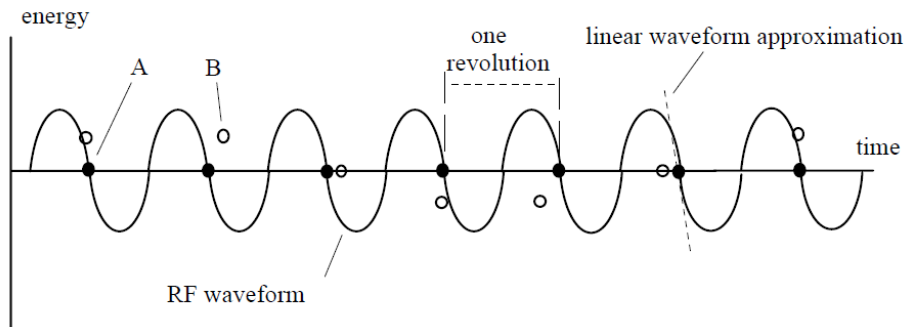


Figure 2.3: Energy variation of two circulating particles passing by the RF cavity [9].

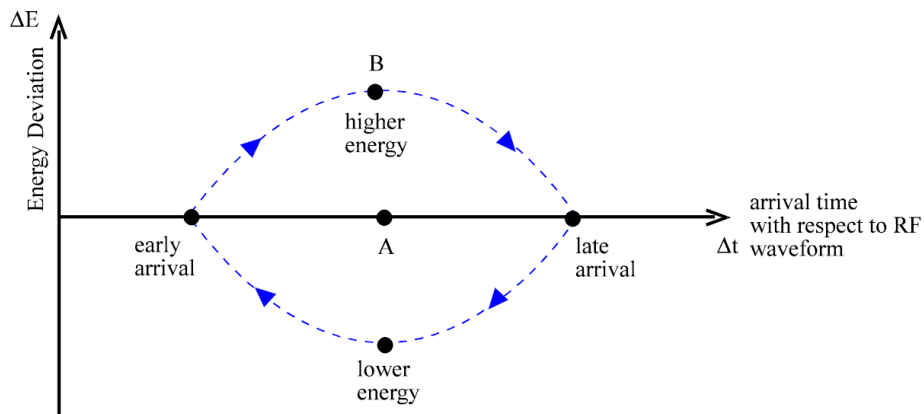


Figure 2.4: Relative motion of A and B in the longitudinal phase space [9].

The RF cavities are normally kept active also after the nominal energy is reached in order to provide a focussing in energy, since an ensemble of

particles always has a momentum spread. Particles with an energy smaller than the nominal one ( $p < p_0$ ) are accelerated by the cavities, while particles with a higher energy ( $p > p_0$ ) are decelerated.

Moreover, a circulating particle loses energy continuously through synchrotron radiation when it bends, as described in [6]. The RF cavities serve then to replenish this energy loss on every turn.

The RF system uses with good approximation a sinusoidal voltage  $V(t) = V \sin(\varphi(t))$  and, for a particle with charge  $q$ , the energy gained at each passage across the cavity to compensate the energy loss turn by turn is:

$$\Delta E = qV \sin(\varphi(t)) \quad (2.27)$$

with  $V$  maximum amplitude of the RF accelerating potential and  $\varphi(t)$  relative phase between the particle and the RF phase as function of time.

The *momentum offset* is related to the energy deviation by:

$$\delta = \frac{\Delta p}{p} = \frac{1}{\beta^2} \frac{\Delta E}{E} \quad (2.28)$$

where  $\beta = v/c$  is the relativistic beta. Similarly, the length of the orbit followed by the particle will also be modified according to [7]:

$$\frac{\Delta L}{L} = \alpha_c \delta, \quad (2.29)$$

where  $\alpha_c$  is the *momentum compaction* factor, which is a fixed property of the lattice depending only on the bending radius of the particle orbit and the dispersion. It represents the difference in path length travelled by a particle at a given relative momentum deviation  $\delta$  within one revolution of the reference particle, as explained in more detail in [7].

The phase focusing principle determines the longitudinal stability of the bunch by:

$$\frac{\Delta T}{T} = \left( \alpha_c - \frac{1}{\gamma^2} \right) \delta, \quad (2.30)$$

with  $T$  revolution period of the proton in the ring and  $\gamma = E/mc^2$  is the relativistic gamma. According to the value of  $\left( \alpha_c - \frac{1}{\gamma^2} \right)$ ,  $\Delta T/T$  can be either positive and negative, depending on the particle energy. The energy at which it changes sign is the *transition energy*  $\gamma_{tr}$ :

$$\gamma_{tr} = \sqrt{\frac{1}{\alpha_c}} \quad (2.31)$$

The synchronous RF phase  $\varphi_s$ , at which the synchronous particles passes the RF cavities on every turn, must be chosen depending on the particle relativistic  $\gamma$ , being below or above the transition. Two different regimes can, hence, be identified:

1.  $\gamma < \gamma_{tr}$
2.  $\gamma > \gamma_{tr}$

In case 1,  $0 < \varphi_s < \frac{\pi}{2}$  ensures the bunch stability, that corresponds to the particle which is on the positive slope of Eq. 2.27. More energetic protons will reach the RF earlier than the reference particle ( $\varphi(t) < \varphi_s$ ), they will lose energy and in the next turn they will get closer to the synchronous proton when they will pass by the cavities again. Less energetic particles, instead, will arrive late in the RF ( $\varphi(t) > \varphi_s$ ), receiving a larger kick by the system that allows them to approach the reference proton in the following turn. Similarly, above transition (case 2) a particle with a higher energy has a longer revolution time and arrives later, meaning that the decelerating voltage should be later in time. Hence, the stable motion occurs on the negative slope of Eq. 2.27, or for  $\frac{\pi}{2} < \varphi_s < \pi$ .

Particles with small longitudinal amplitude, which occurs as long as they are close to the center of the bucket and not at the edges, even if the motion is still stable, perform synchrotron oscillations around the nominal particle (see Fig. 2.5). In the approximation of small oscillations, the equation of motion in the longitudinal phase can be expanded to first order in energy and phase. It becomes [7]:

$$\ddot{\varphi} + 2\alpha_z \dot{\varphi} + \Omega^2 \varphi = 0 \quad (2.32)$$

with:

$$\Omega^2 = \frac{\omega_{rev}^2 h \alpha_c e V_{max}}{c \beta p_0 2\pi} \cos \varphi_s \quad (2.33)$$

$\alpha_z$  and  $\Omega$  are respectively the damping decrement and the synchrotron angular frequency. It means that a particle circulating in a ring performs harmonic oscillation with angular frequency  $\Omega$ , that can be damped or antidamped according to the sign of  $\alpha_z$ . Damping occurs only if there is an energy loss depending on the particle energy, as it is for the synchrotron radiation emission. As for the betatron oscillation tune, we can also define the synchrotron oscillation tune as:

$$Q_s = \frac{\Omega}{\omega_{rev}}. \quad (2.34)$$

For larger oscillation amplitudes, which correspond to higher energy spread, the approximation  $\sin \varphi \approx \varphi$  is no more valid and the equation of the motion is expressed by:

$$\ddot{\varphi} + \Omega^2 \sin \varphi = 0 \quad (2.35)$$

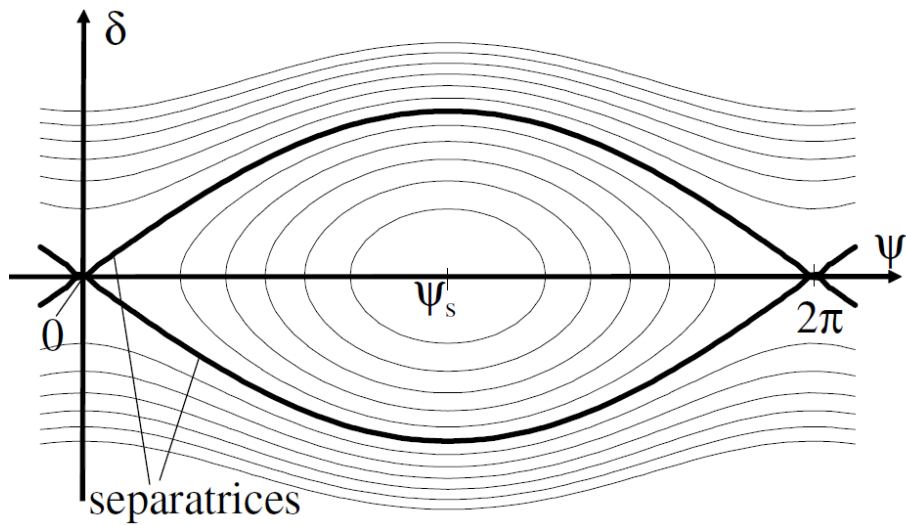


Figure 2.5: Motion of particle inside and outside the bucket limit [7].

The particle oscillation in the longitudinal phase space is mathematically similar to the motion of the mechanical pendulum of Fig. 2.6. Unless the pendulum reaches the point H, it goes back and forth around the equilibrium point. When the pendulum reaches its non-equilibrium point (separatrix), then it goes down again. But if the energy is high enough to reach H, once the pendulum reaches the top, it does not go back, but it goes on in a never-ending motion like a wheel (unstable motion for particle with energy larger than the RF potential).

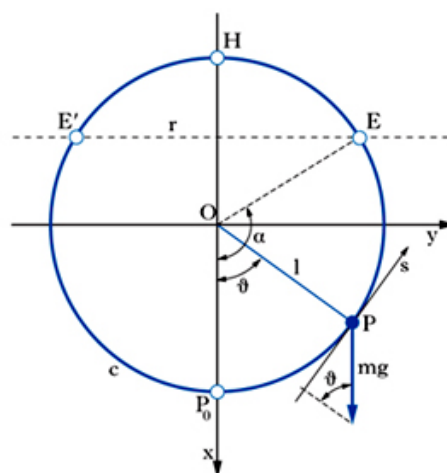


Figure 2.6: Mechanical pendulum motion.

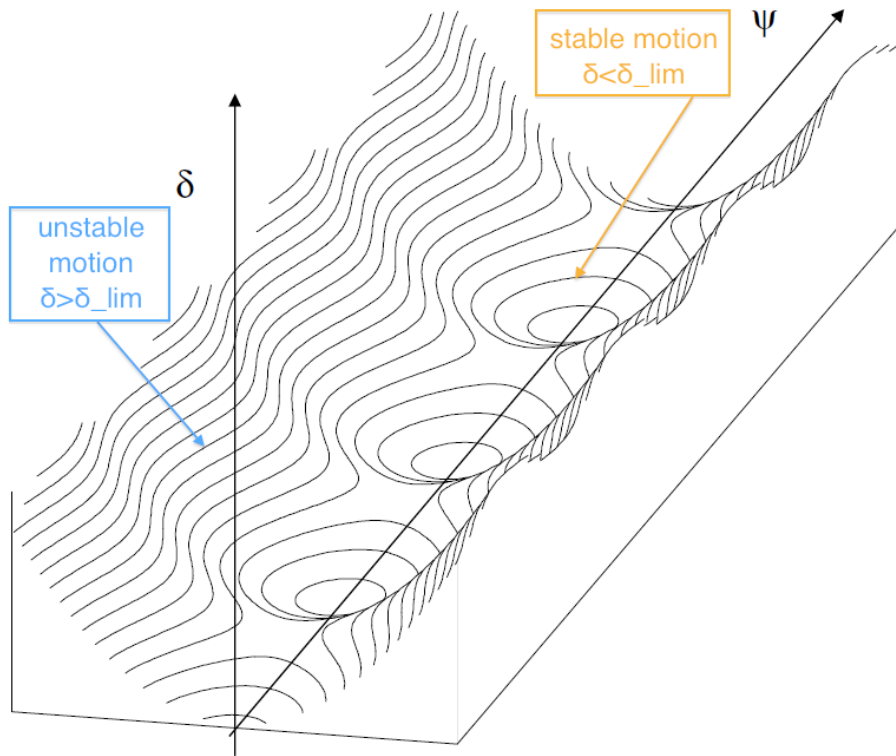


Figure 2.7: RF potential well in the longitudinal phase space [7].

Therefore, as shown in Fig. 2.7, particle trajectories in phase space can be distinguished in two different types: closed orbits inside the RF-bucket in which particles perform stable motion and unstable motion outside for those particles having an energy large enough to go beyond the bucket limit. The specific trajectories in phase space which separate the stable region from the region where the motion is unstable leading the particle away from the synchronous phase and from the ideal momentum are called *separatrices*. If a proton injected in a storage ring has an energy corresponding to a point outside the separatrix, it will perform unbounded motion.

The energy deviation that matches the separatrix determines the *energy aperture* of the ring. Now we take a particle starting outside of the energy aperture, considering also the radiation damping effect (that means the particle is losing energy through emission of synchrotron radiation): its motion starts outside the stable region and it will stay outside forever. Moreover, the energy loss moves the particle further away from the nominal energy and, then, from the synchronous particle. When the accumulated energy deviation is large enough, the particle could hit the aperture of the machine and be lost.

### 2.1.3 Dispersion

In the previous paragraph, we introduced the effect that a momentum offset produces in the longitudinal space. In the transverse plane, an energy offset is manifested by a new distorted closed orbit, around which the particles can perform betatron oscillations. For small deviations in momentum, Eq. 2.9 becomes:

$$x'' + K(s)x = \frac{\delta}{\varrho(s)} \quad (2.36)$$

The solution of this equation is:

$$x(s) = x_\beta(s) + x_\delta(s) \quad (2.37)$$

where  $x_\beta$  is the betatron oscillation around the off-momentum orbit and  $x_\delta(s)$  is the displacement due to the energy error.  $x_\delta(s)$  is the particular solution of the inhomogeneous equation (2.36) and it is generally expressed as:

$$x_d(s) = D(s)\delta \quad (2.38)$$

where  $D(s)$  is the *dispersion function* which is a particular solution that satisfies the equation:

$$D'' + K(s)D = \frac{1}{\varrho(s)} \quad (2.39)$$

The displacement in  $x'(s)$  can be also computed by:

$$x'_d(s) = D'(s)\delta \quad (2.40)$$

then the total displacement in angle becomes:

$$x'(s) = x'_\beta(s) + x'_d(s) \quad (2.41)$$

So, taking also into account the dispersion effect, the center of the ellipse of Fig 2.2 will be modified and shifted, as shown in Fig 2.8)

The same procedure can be followed for the solution in  $y$ .

## 2.2 Beam halo and collimation

Ideally the electromagnetic fields in a ring ensure the particles, once injected, perform stable motion as the forces are conservative. Different effects, however, increase the emittance and, as a consequence, some particles slowly drift towards the walls of the machine where sooner or later they are lost. The mechanical aperture of the machine is now discussed more in details. In addition, a brief explanation of how the beam halo is generated, why it can be dangerous for an accelerator and how the beam cleaning performance of collimators can be expressed will follow in the section.

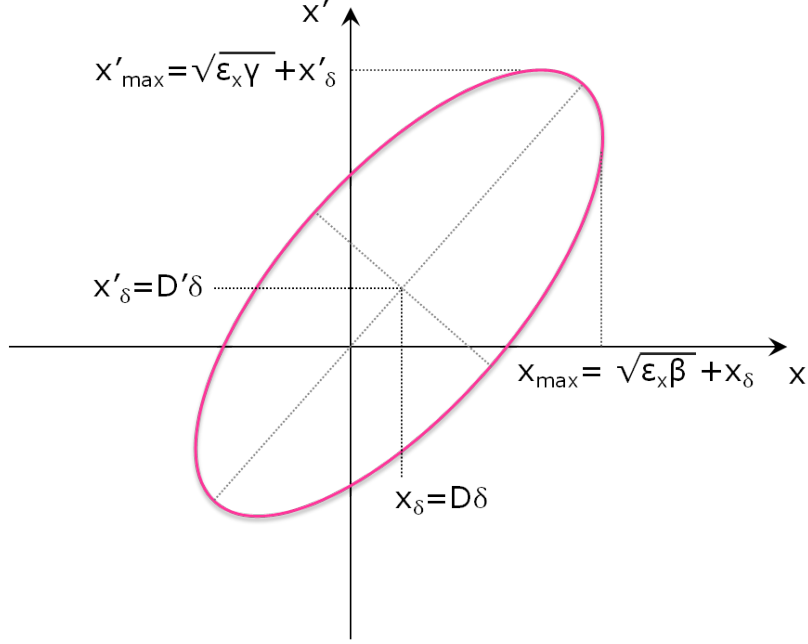


Figure 2.8: The phase space ellipse in the  $x$ - $x'$  plane of a particle with momentum offset  $\delta$ .

### 2.2.1 Machine aperture

The physical space set by the vacuum chamber in which the particle beam moves and by the equipments installed all along the ring (e.g. screens, collimators, other diagnostic instrumentation) is called *geometrical aperture*  $A_{geo}$ . The aperture is commonly expressed in units of the standard deviation of the real beam size in a certain plane, which in plane  $i$  is derived by:

$$\sigma_i^{real}(s) = \sqrt{\beta_i(s) \cdot \epsilon + (D_i(s) \cdot \delta)^2} \quad (2.42)$$

Therefore, at any location of the machine, the geometric aperture must be larger than the maximum oscillation amplitude of the particles to avoid that particles hit the opening. The maximum area of the phase space ellipse that a particle can safely cover in  $i$  plane defines the *beam acceptance*  $A_i$ :

$$A_i(s) = \frac{(A_{geo}(s) \cdot \sigma_i^{real}(s))^2}{\beta_i(s)} \quad (2.43)$$

As soon as  $A_i \geq A_{geo} \cdot \sigma_i^{real}$  the particle is lost at that location.

Moreover, in a real accelerator the presence of non-linear elements (i.e. sextupole magnets, used for machine chromaticity correction, or higher order correctors), introduce unavoidable non-linearities in the magnetic fields

that act on all the beam particles. Therefore, a particle with an oscillation amplitude larger than a certain value, called *dynamic aperture*  $A_{dyn}$ , will no longer perform stable oscillation but be lost after some turns. An idea of the geometrical and dynamic aperture is shown in Fig. 2.9.

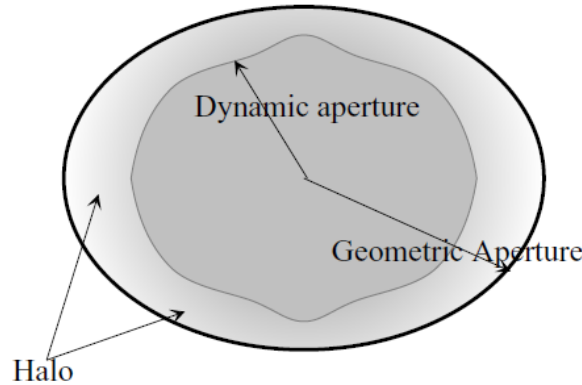


Figure 2.9: Geometrical and dynamic aperture in an accelerator [10].

### 2.2.2 Generation of beam halo

Particles inside the beam core are ideally stable with an oscillation amplitude  $A \lll A_{geo}$ . However, there are several processes that move some particle out of the core, populating the so-called beam halo which diffuses towards  $A_{dyn}$ . Some mechanism that influences the distribution of the circulating beam and give rise to the halo are listed below [11, 10]:

- *Intrabeam scattering* (IBS): particles belonging to the same bunch perform elastic Coulomb scattering with a small deflection angle [12]. A continuous exchange of energy between the interacting particles induces the coupling of components of the emittance in the horizontal, vertical and longitudinal direction.
- *Elastic and inelastic scattering* between the particles and the nuclei of the gas molecules left in the beam pipe: losses of particles are generated and the beam emittance grows.
- *Beam-beam effects*: after a bunch-bunch collision, particles that have performed elastic scattering, can populate the halo provoking a transversal emittance growth.
- *Radiation damping*: ultra-relativistic particles emit, transversally to their trajectory, electromagnetic radiation when they are bent by electromagnetic fields [6]. That means that an amount of their initial

energy is lost in the same direction. The RF cavities have to compensate this energy loss but the acceleration is purely longitudinal: the transverse components of the momentum are not increased after the passage through the cavities and the motion in the x-y plane is damped. On the other hand, particles outside the RF bucket continue to lose energy turn by turn, drifting transversally from the centre of the beam.

Why is the halo so dangerous for the operation of an accelerator? Several reasons can explain that: far away from the centre of the beam, in fact, the magnet non-linearities or any other processes showed before become more important: the particle motion becomes unstable and the risk that the beam halo is lost in the machine increases. High energy deposition of the particle impacting in the matter causes life reduction and radiation damage of the accelerator components hit. In particular, uncontrolled particle loss in the superconducting magnets can lead them to quench if the energy deposition overcomes the quench limit. From the experiment point of view, the halo also determines a background signal that have to be always monitored to avoid errors in the measurements.

The halo particles must be effectively cleaned by a dedicated system to avoid, or at least reduce, they are lost somewhere in the accelerator. Thus, a collimation system is needed: its main task should be to intercept the halo particles in a controlled way and remove the beam losses on the aperture.

### 2.2.3 Collimation cleaning performance

Most collimators consist of two jaws, facing one another, which are placed between the beam and the mechanical aperture of the machine (Fig. 2.10). The distance between the center of beam and the surface of the jaws defines the collimator half-gap, an important parameter required to align the entire system in a proper way.

Different parameters are often used to quantify the cleaning performance of the collimation system. One of them is the *Global Cleaning Inefficiency*  $\eta_g$  given by:

$$\eta_g(A_i) = \frac{N_p(A > A_i)}{N_{abs}} \quad (2.44)$$

where  $N_p$  is the number of particle escaping the cleaning insertion with a betatron oscillation amplitude  $A$  bigger than a certain amplitude  $A_i$  and  $N_{abs}$  is the total number of particles absorbed in the collimation system. Inefficiency  $\eta_g(A_i)$  should be as small as possible to can have an efficient cleaning system.

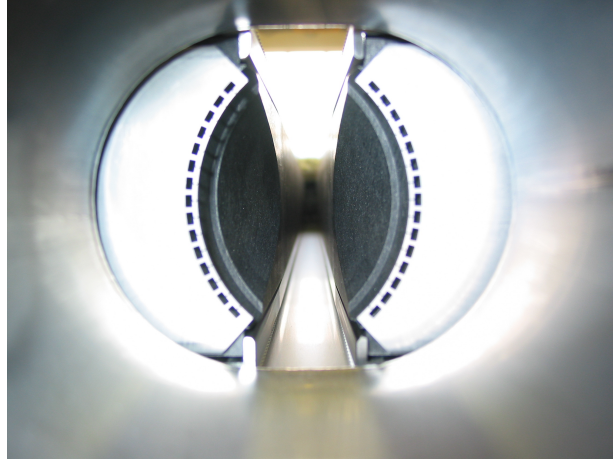


Figure 2.10: Inner view of two collimator jaws [13].

However, it is also important to know the distribution of the losses along the ring, because the surviving particles not stopped in the collimator material are lost locally in the machine and could cause quenches in the magnets. For this reason, a second parameter must be introduced, the *Local Cleaning Inefficiency*  $\eta_c$ :

$$\eta_c = \frac{N_{loss}}{\Delta s \cdot N_{abs}} \quad (2.45)$$

where  $N_{loss}$  refers to the particles lost in a  $\Delta s$  length.

As already said, the magnets, especially if they are superconducting, are one of the most critical part in a circular storage accelerator. In order to keep them in safe operating conditions and avoid quench, the value of  $\eta_c$  must be compared and stayed below the *Local Cleaning Inefficiency at the quench limit*  $\eta_c^q$ :

$$\eta_c^q = \frac{R_q \tau}{N_{tot}} \quad (2.46)$$

in which  $R_q$  identifies the maximum allowed particle loss per meter to not quench the magnets,  $\tau$  is the beam lifetime and  $N_{tot}$  is the total beam intensity. The beam lifetime  $\tau$  is a parameter that quantifies the evolution of the beam loss in a storage ring. If a beam contains  $N$  particles,  $\tau$  is defined through:

$$\frac{1}{\tau} = -\frac{1}{N} \frac{dN}{dt} \quad (2.47)$$

Then,  $\tau$  represents the time needed to reduce the number of particles to a fraction  $1/e$  of the initial intensity. In linear approximation, the loss rate from the beam is thus  $N_{tot}/\tau$ .

### 2.2.4 Beam losses and interaction with collimator materials

When halo particles impact on a collimator jaw, several different processes may take place [14]:

- *Ionization and excitation*: when particles pass through matter, they lose energy by ionizing or exciting the atoms of the material. The Bethe-Bloch equation defines the stopping power  $-\frac{dE}{dx}$  as the average energy lost by a particle per unit of crossed length, i.e. [15]:

$$-\frac{dE}{dx} = Kz^2 \frac{Z}{A} \frac{1}{\beta_{rel}^2} \left[ \frac{1}{2} \ln \frac{2m_e c^2 \beta_{rel}^2 \gamma^2 T_{max}}{I^2} - \beta_{rel}^2 - \frac{\delta}{2} \right] \quad (2.48)$$

where  $K$  is a constant,  $Z$  and  $A$  are respectively the atomic number and the atomic mass of the target material,  $m_e$  is the electron mass while  $z$ ,  $\beta_{rel}^2$  and  $\gamma$  are respectively the charge, the velocity and the relativistic factor of the incident particle.  $I$  is the mean excitation energy,  $T_{max}$  is the maximum kinetic energy that an electron can gain in one single collision and finally  $\delta$  is a correction term depending on the density of the material.

- *Multiple Coulomb Scattering* (MCS): a charged particle travelling through matter faces numerous small angle deflections, most of them due to Coulomb scattering on the nuclei and electrons. The deflection angle  $\theta$  after crossing a thickness  $s$  of material is given by[16] :

$$\theta(s) = \frac{13.6MeV}{\beta_{rel}cp} z \sqrt{\frac{s}{X_0}} \left[ 1 + 0.038 \ln\left(\frac{s}{X_0}\right) \right] \quad (2.49)$$

with  $p$  momentum of the incident particle.  $X_0$  is the radiation length and it is a characteristic of the material: it can be explained as the mean length to be crossed by the particle inside the material to reduce its energy by a factor  $1/e$ .

- *Rutherford Scattering* (RS): an incoming proton coming very close to a nucleus is deflected away from it by a large electrostatic (Coulomb) force due to the positive charge of the nucleus, inducing large scattering deflection angle.
- *Point-like interactions*: unlike the previous mechanisms which occur over a certain length of material, proton-matter interaction can also involve an incoming proton and one of the components of the atomic structure of the crossed material (proton, neutron or even an entire nucleus). The proton-nucleon interactions can be elastic, inelastic or

inelastic-diffractive. In the case of elastic or *single diffractive* scattering, the proton has a non-zero probability to survive the interaction with the collimator jaw, escaping from the material and populating the off-momentum halo.



# The CERN Large Hadron Collider

---

## 3.1 Overview of the LHC: accelerator chain, experiments and performance

The Large Hadron Collider (LHC) is a circular accelerator designed with the aim of testing the predictions of different theories of particle and high energy physics, particularly looking for the theorized Higgs boson [17] and other new particles predicted by supersymmetric theories [18]. The LHC is installed in a 27 km long circular tunnel at a depth ranging from 50 to 175 m underground and it is situated at the border between Switzerland and France (see Fig. 3.1).

This accelerator has been designed [1] to accelerate and provide proton-proton and lead ion collisions with a centre-of-mass energy of 14 TeV and 1.15 PeV respectively. Design parameters are not yet achieved: operation started at 3.5 TeV in 2010-2011 and the beam energy was raised to 4 TeV in 2012. A maximum stored energy of 147 MJ has been used. On March 2013, the LHC has started a shutdown period (LS1) for upgrades to increase energy to 6.5 TeV per beam, with the restart planned for early 2015. The goal is still to achieve the design parameters.

Two counter-rotating beams are bent to stay on their circular orbits by SC magnets cooled in a bath of superfluid helium and brought into collision in four detectors. Before entering the LHC, the particles pass through several smaller accelerators, called injectors, as shown in Fig. 3.2, to be accelerated up to the operation energy. After the extraction from the hydrogen source at about 50 keV, the protons enter in the 35 m long LINear ACcelerator (LINAC), where their energy is increased up to 50 MeV. The Proton Synchrotron Booster (PSB) brings them to 1.4 GeV and then they are ready to be injected in the Proton Synchrotron (PS). Here the particles are grouped into trains of bunches with 25 or 50 ns spacing and receive a further acceleration up to 26 GeV/c. In the last step before the LHC, the protons are transferred to the SPS (Super Proton Synchrotron), where they reach an energy of 450 GeV. The protons are now injected in the LHC and

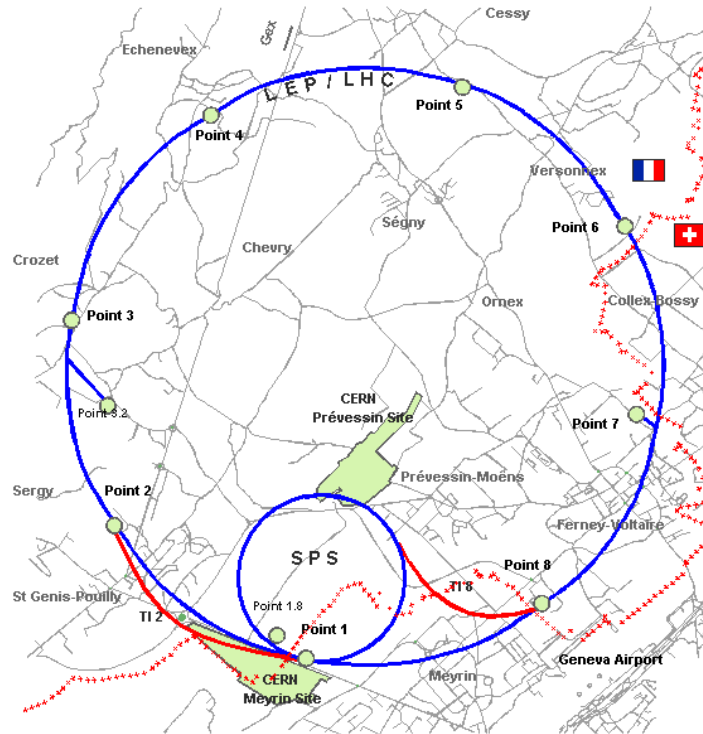


Figure 3.1: CERN site in Geneva area [19]. The blue lines reproduce the position of the two underground rings of the accelerating chain: LHC and its injector SPS (injection transfer lines in red).

split in the two beams.

The LHC is divided in eight arcs and eight straight sectors, called insertion regions (IRs), where the experiments and the utility insertions are installed. As shown in Fig. 3.3, the two beams are injected into the machine in IR2 (Beam 1) and IR8 (Beam 2) and accelerated up to the nominal top energy by the radio frequency cavities located in IR4. The collisions occur at the four interaction points (IPs) which host the detectors: the two biggest experiments are *ATLAS* (A Toroidal LHC ApparatuS) [20] (Point 1) and *CMS* (Compact Muon Solenoid) [21] (Point 5). *LHCb* (Large Hadron Collider beauty) [22] (Point 8) is dedicated to study the decay of B mesons and *ALICE* (A Large Ion Collider Experiment) [23] (Point 2) is optimized for heavy ions collisions. During the normal operation of the machine the beams are stored and kept colliding for many hours and once the "Physics" period ends or in case of a failure, the beams are extracted from the ring by the dump system located in IR6. IR3 and IR7 are dedicated to respectively the momentum and betatron cleaning of the beam.

The goal of The LHC is to observe the products of hadron collisions

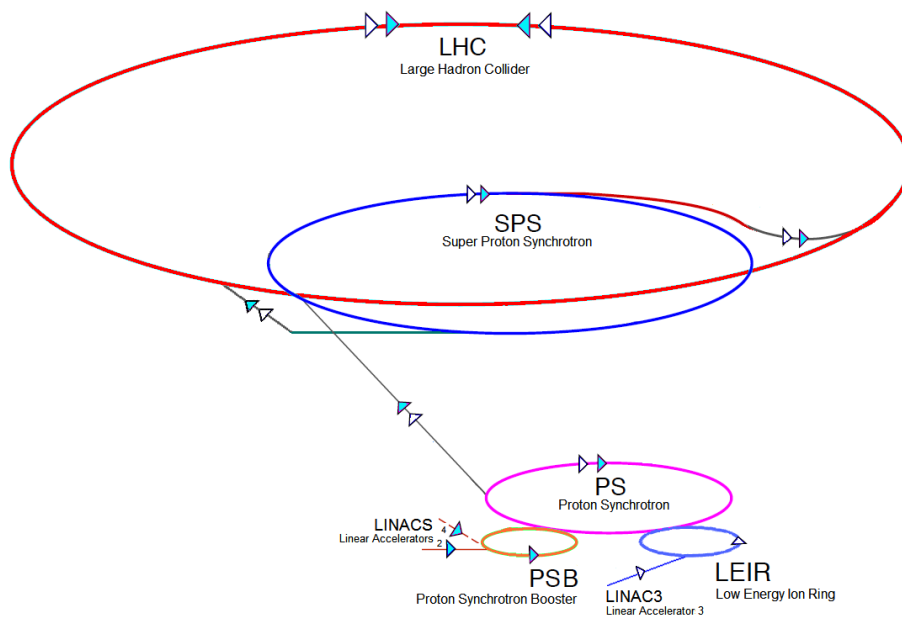


Figure 3.2: LHC injectors chain, for proton and ion run [13].

with particle detectors. A sufficient amount of events has to be accumulated before reaching a conclusion. Therefore, one of the most critical parameters for a particle collider is the collision frequency per interaction cross section, which is called the *Luminosity*  $\mathcal{L}$ . For two head-on colliding beams with an identical Gaussian beam distribution (ideal case), the luminosity can be expressed as:

$$\mathcal{L} = \frac{N_b^2 n_b f_{rev} \gamma_{rel}}{4\pi \epsilon_n \beta^*} F \quad (3.1)$$

with  $N_b$  number of particles per bunch,  $n_b$  number of bunches per beam,  $f_{rev}$  revolution frequency,  $\gamma_{rel}$  relativistic gamma,  $\beta^*$  the beta function at the collision points and  $F$  the geometric luminosity reduction factor due to the crossing angle that is imposed to the colliding bunches in order to avoid parasitic collisions at the IP.  $\epsilon_n = \epsilon \beta_{rel} \gamma_{rel}$  is called normalized transverse beam emittance and it stay constant with the energy. If  $\beta_{rel}$  is close to one (that is the case of the LHC were particles are very close to the speed of light), the emittance is approximately inversely proportional to the energy and so the physical width of the beam will vary inversely to the square root of the energy. This approximation has been made in Eq. 3.1. About 1 billion proton-proton interactions per second are expected with the nominal LHC design luminosity. It is achieved thanks to 2808 circulating bunches of  $1.15 \times 10^{11}$  protons each. The main parameters for the nominal proton beam operation are summarized in Table 3.1.

Table 3.1: LHC main design parameters from [1]. The table show the design values of the parameters (at injection and collision). The last column contains the values used during the 2012 physics operation.

	<b>Injection</b>	<b>Design collision</b>	<b>2012 collision</b>
<b>Beam data</b>			
Energy [GeV]	450	7000	4000
Relativistic gamma	479.6	7461	4263
Number of particles per bunch	$1.15 \times 10^{11}$		$1.4 \times 10^{11}$
Number of bunches	2808		1380
Bunch spacing [ns]	25		50
Transversal normalized emittance [ $\mu\text{m rad}$ ]	3.75		2.5
Stored energy per beam [MJ]	23.3	362	146.5
Energy loss per turn [eV]	$1.15 \times 10^{-1}$	$6.71 \times 10^3$	$0.72 \times 10^3$
<b>Peak luminosity related data</b>			
RMS bunch length [cm]	11.4	7.55	9.73
Geometry luminosity reduction factor F	-	0.836	0.79
Peak luminosity in IP1 and IP5 [ $\text{cm}^{-2}\text{s}^{-1}$ ]	-	$1.0 \times 10^{34}$	$0.77 \times 10^{34}$
<b>Geometry</b>			
Ring circumference [m]	26658.883		
Ring separation in arcs [mm]	194		
<b>Magnets</b>			
Number of main bends [m]	1232		
Length of main bends [m]	14.3		
Bending radius [m]	2803.95		
Field of main bends [T]	0.535	8.33	4.76
<b>Lattice</b>			
Horizontal tune	64.28	64.31	64.31
Vertical tune	59.31	59.32	59.32
Momentum compaction $\alpha_c$	$3.225 \times 10^{-4}$		
Gamma transition $\gamma_{tr}$	55.68		
<b>RF system</b>			
Revolution frequency [kHz]	11.245		
RF frequency [MHz]	400.8		
Harmonic number h	35640		
Total RF voltage [MV]	8	16	12
Synchrotron frequency [Hz]	61.8	21.4	26.3

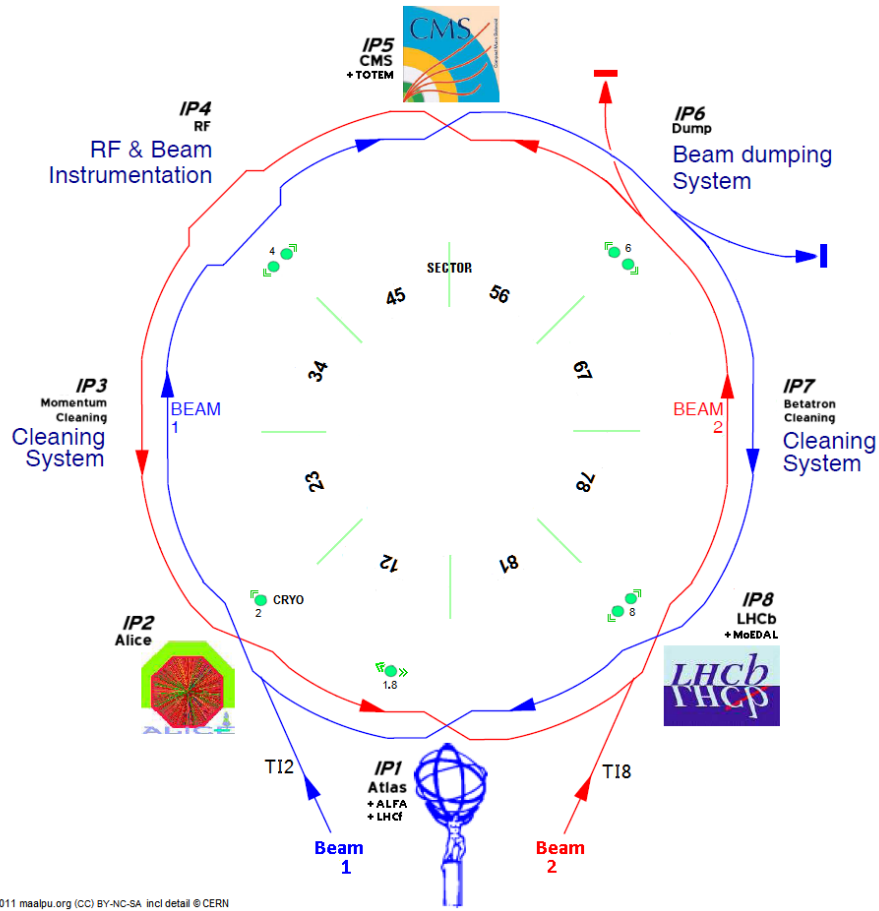


Figure 3.3: Layout of the LHC [13]. Beam 1 circulates clockwise and Beam 2 counterclockwise. Four sections host the experiments and the other four the collimation, the RF and the dump system.

## 3.2 The LHC collimation system

The high beam energy stored in the LHC (362 MJ at 7 TeV) implies that the beams are highly destructive. At the same time, the superconducting magnets would quench at 7 TeV even if a small amount of energy (around  $30 \text{ mJ/cm}^{-3}$ , corresponding to a local loss of  $4 \times 10^7$  protons) is deposited into the superconducting magnet coils. Therefore, the handling of the high intensity beams and their relative loss requires a very efficient collimation system[1], that can intercept and absorb any beam losses in a safe and controlled way in order to protect the magnets.

### 3.2.1 General design of a LHC collimator

Fig. 3.4 shows a general configuration of an LHC collimator. In Fig. 3.5 and Fig. 3.6 more detailed views are shown.

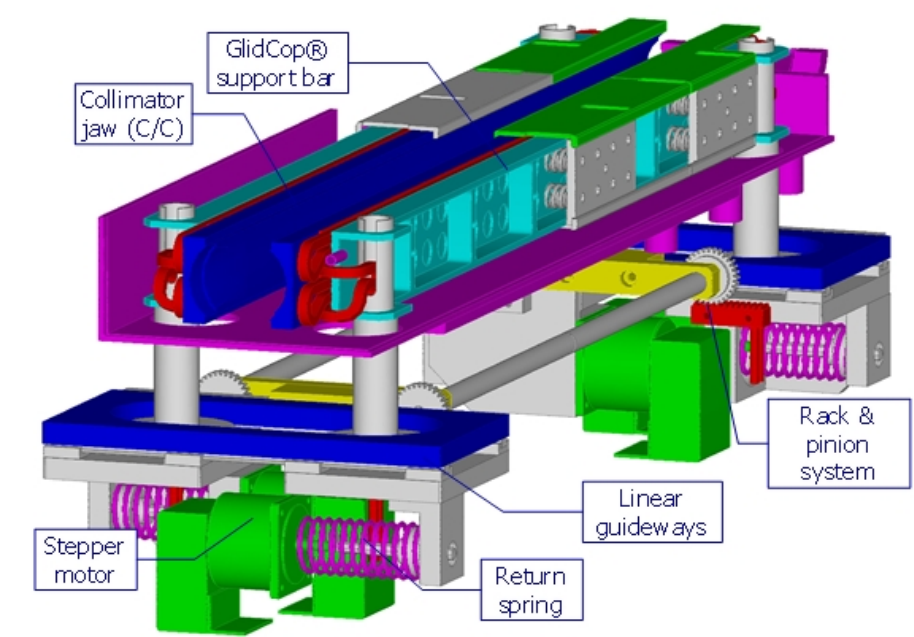


Figure 3.4: Scheme of the LHC collimator [13].

Most of collimator consist of two jaws, independently movable, with the beam passing in the centre between them. The jaws are the parts closest to the beam, which should intercept the halo particles, and they are made of different materials, according to their role in the hierarchy (see Section 3.2.2). The surface of each jaw is constituted by a flat part, determining the active length (different for each collimator type) and by a 10 cm tapering part at both ends to minimize geometrical impedance effects. One of the major requirement for the LHC collimators is that they are movable in order to efficiently intercept the halo: the collimator jaws must always be centered and aligned with respect to the beam envelope and the actual orbit, which change longitudinally along the ring and also during the ramp in energy. Precise stepping motors are used to move the jaws. Four motors are installed per collimator, one at each jaw end. They are used to set the aperture and the tilt angle. A fifth motor shifts transversally the whole collimator tank for some special collimators. Two collimator jaws are put in a vacuum tank. The cooling of jaws and tanks is provided by a heat exchanger with copper-nickel pipes. A GlidCop support bar presses the cooling pipes against the jaw material by means of clamping springs: this system avoids mechanical

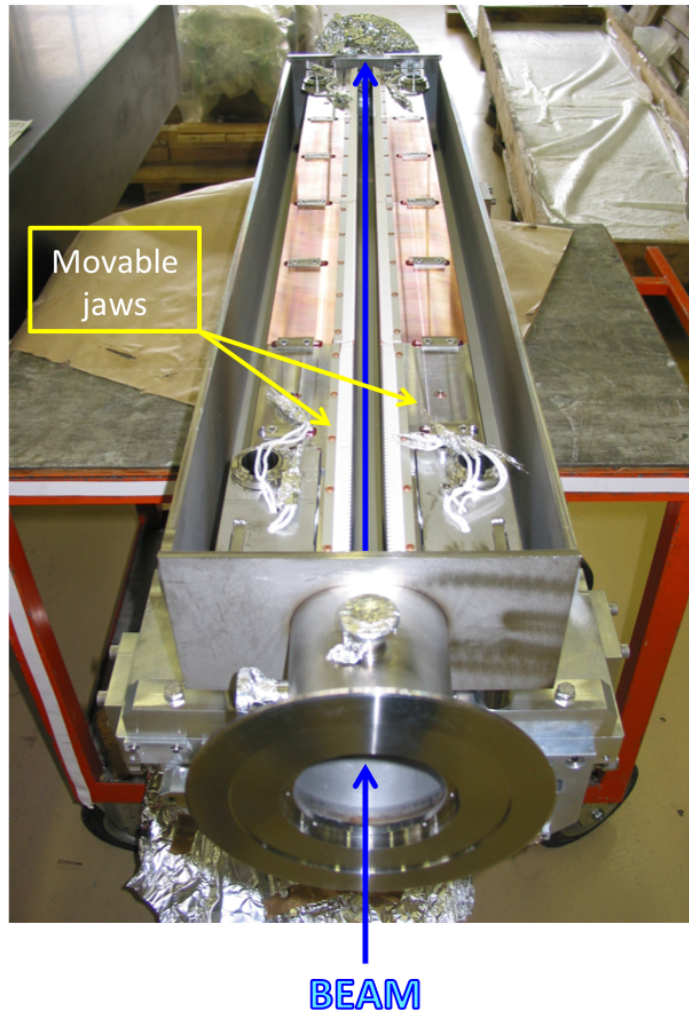


Figure 3.5: Top view of an opened collimator [13].

stress caused by the contact between materials (jaws and heat exchanger) having different thermal expansion coefficient and, at the same time, it enhances the thermal contact between them.

### 3.2.2 The multi-stage LHC collimation system

Considering the high demands on beam cleaning, a multi-stage collimation system in which collimators are set with different aperture settings, is required (see Fig. 3.7). The main goals of the LHC collimation system are beam cleaning, passive machine protection and minimization of the background signal at the experiments. Different collimator designs are used to better achieve these tasks and the collimators are grouped in different fam-

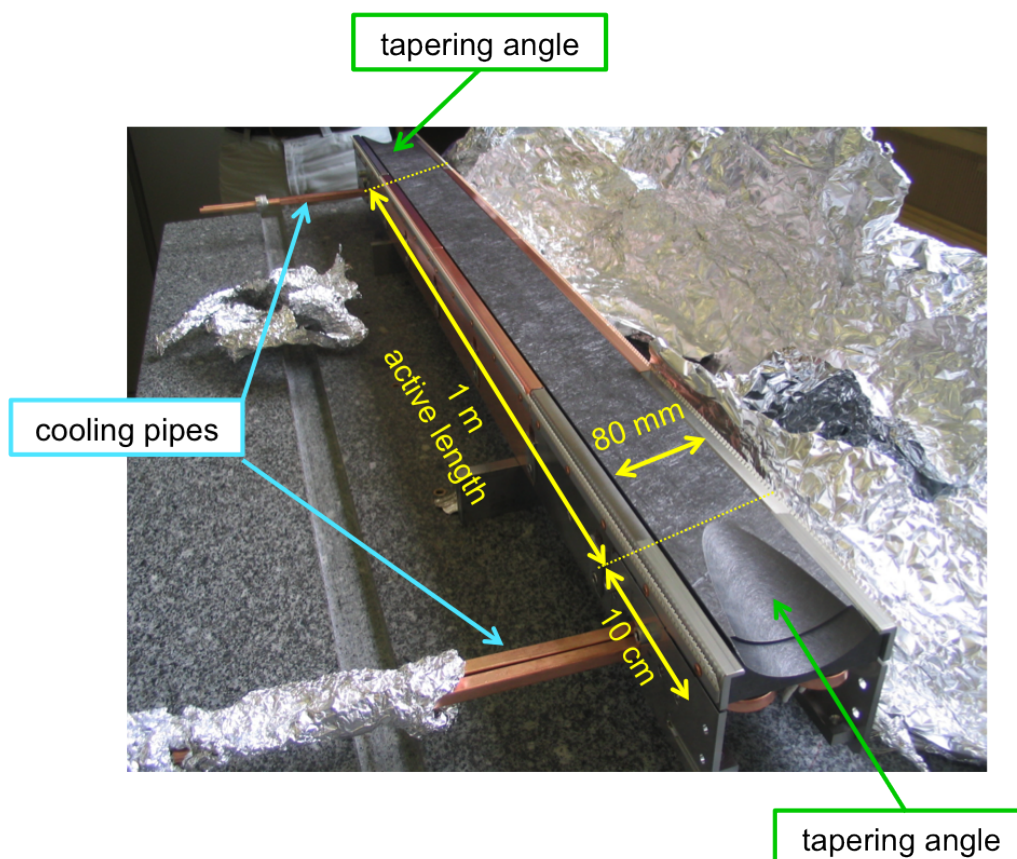


Figure 3.6: Top view of a carbon-carbon jaw [13].

ilies. A strict position hierarchy is imposed on these families, as explained below. Fig. 3.8 shows a complete layout (not to scale) of all installed collimators in the LHC.

Depending on their orientation in the space, collimators can be horizontal, vertical or skew. The azimuthal angle for the skew ones is defined by starting from the positive x-axis and rotating clockwise in the x-y plane (see Fig. 3.9). The aperture of each collimator is expressed in units of the standard deviation of the beam in the collimator plane, which is given by:

$$\sigma_i = \sqrt{\beta_{x,i}\epsilon \cos^2 \theta_i + \beta_{y,i}\epsilon \sin^2 \theta_i}, \quad (3.2)$$

where  $\beta_{x,i}$  and  $\beta_{y,i}$  are the betatron functions at collimator  $i$ ,  $\theta_i$  is the azimuthal angle of the  $i$ -th collimator and  $\epsilon$  being the nominal geometrical emittance, given by  $\epsilon = \epsilon_n/\gamma_{rel}$ , with  $\epsilon_n = 3.5\mu\text{m rad}$  the normalized emittance at 7 TeV LHC operation. Therefore, the jaws of collimator  $i$  are positioned on each side of the beam, with a distance of:

$$\pm n_i \cdot \sigma_i, \quad (3.3)$$

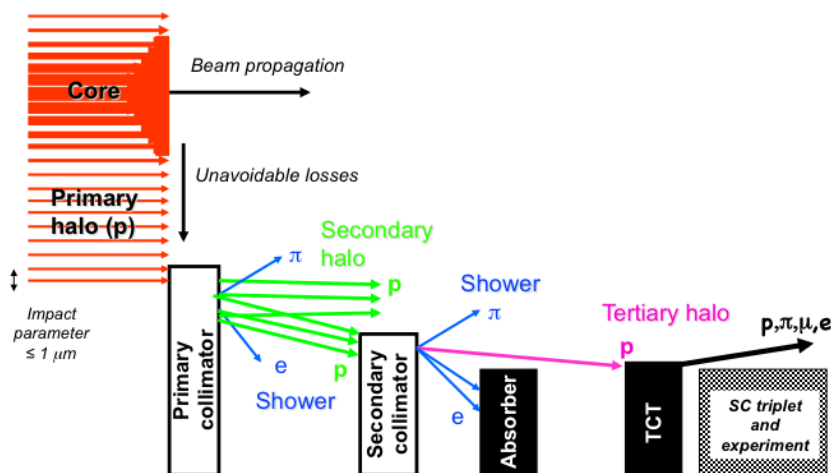


Figure 3.7: Sketch of the multi-stage collimation system to intercept the different halo types [24].

from the beam center. The opening  $n_i$  is different for every collimator type (see below). The settings of the collimators must be carefully adjusted in order to minimise the leakage rates of the insertions.

### Collimators for beam cleaning

From Eq. 2.41, the transverse motion of a particle in a ring can be seen as the linear superposition of two independent components: the transverse betatron motion and the synchrotron oscillation. Particles with high betatron amplitude or with large momentum deviation must be cleaned if they risk to perturb the operation of the accelerator, e.g. through magnet quenches or radiation damage. Then, thanks to the linearity of Eq. 2.41, we can have a collimation system that fulfils the two tasks separately. This is exactly the case of the LHC, where there are two different insertions dedicated to collimation:

- *Betatron Cleaning insertion* (IR7): this insertion is characterized by low dispersion value, where the particles with large distance from the beam center are characterized by high betatronic amplitude, while the transversal displacement due to the momentum offset is negligible.
- *Momentum Cleaning insertion* (IR3): here the dispersion is higher and the halo particles are characterized by a high momentum offset. In the

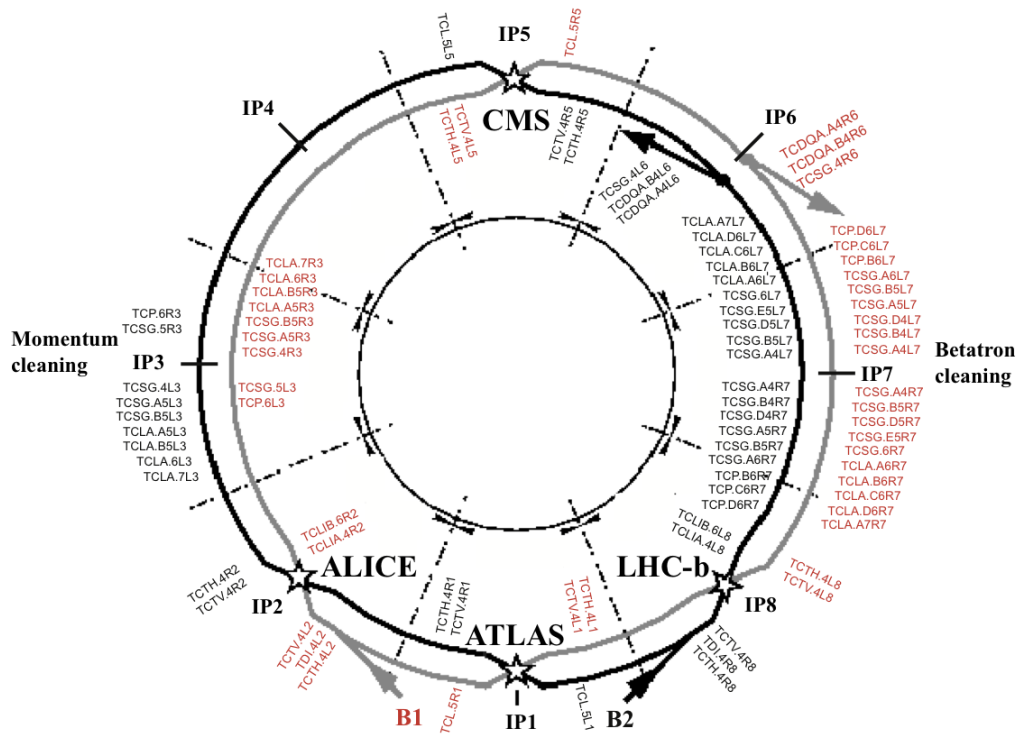


Figure 3.8: General layout of the LHC collimation system [11].

reality, due to constraints of the optics, the  $\beta$ -function is not negligible in IR3.

The layout of the system in the two insertions is quite similar (see Fig. 3.10: it consists of primary (TCP) and secondary (TCSG) collimators plus absorbers (TCLA). TCPs remove particles that have left the core of the beam. At LHC energies, the TCP cannot absorb all protons from the primary halo and a secondary halo leaks out. Secondary collimators (TCSGs), downstream of the TCPs and more open, intercept it. These are two sided collimators with fiber-reinforced graphite (CFC) jaws.

One of the most discussed point of the collimator design concerns the choice of the material of the jaws. In principle, a performing collimator material should have different characteristics that can often be conflicting. In order to reach a sufficient absorption rate for cleaning task, materials with high atomic number  $Z$ , like tungsten, are preferable. However, they are much less robust against mechanical damage for which low  $Z$  materials (graphite for example) are preferred to reduce the power deposition in the jaw. Furthermore, the impedance of the collimators should be kept low, in order to reduce the risk of beam instabilities [1]. A system with sufficiently low impedance, like a copper based one, would induce a risk of material

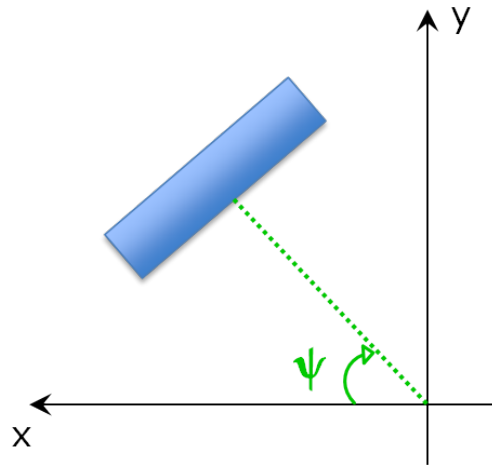


Figure 3.9: Azimuthal angle  $\psi$  for skew collimators. It is defined rotating clockwise from the positive x-axis to the y-axis. By default, x-values are considered positive in the outgoing direction with respect to the center of the ring. The figure shows the case of Beam 1.

damage to the collimator jaws in case of high beam losses, resulting in a reduction of the cleaning performance of the collimation system.

The choice of a low  $Z$  material for TCPs and TCSGs reduces the energy deposition in the jaws and makes the collimator robust. The primary collimators have an active length of 60 cm, while a 1 m length was chosen for the secondaries. In addition, downstream of the TCSG some active absorbers are installed: they are also two-sided but made of a high  $Z$  material (tungsten) to increase the absorption rate. The TCLAs are more open than the TCSGs and must intercept the particles even farther away from the core (tertiary halo) and the showers produced by inelastic interactions of the protons inside the TCP and the TCSG jaws. The settings of the different families are shown in Table 3.2. After the energy ramp, the position of these collimators does not change during the following parts of the operation.

### Collimators for machine protection

In order to protect the LHC against possible losses following equipment failures or wrong operation, some special collimators are installed in the most critical location of the ring.

The injector beam stoppers (TDIs) are vertical collimators with 4.2 m long carbon-carbon jaws. They are installed to ensure a correct beam injection setup even in case some of the injector kickers fails: the upper jaw,

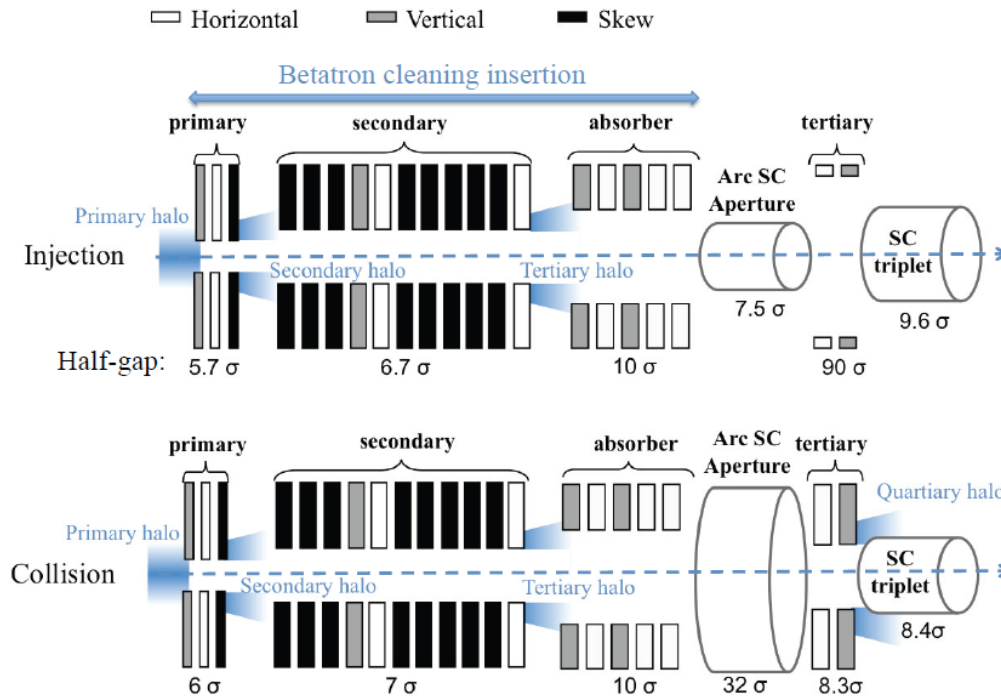


Figure 3.10: Example of collimators position in IR7 [11].

in fact, should intercept bunches not sufficiently deflected by the kickers, while the lower jaw should catch miskicked beam. Additional two-sided vertical collimators are located downstream of the LHC injection point (IR2 for Beam 1 and IR8 for Beam 2). They are moved in when the beam is injected and then retracted before the acceleration of the particles starts.

In IR6, a dump protection collimator, called TCDQs, is placed, followed by a TCSG. They should protect the machine in case of malfunctioning of the beam exaction system. The TCDQ is a one-side horizontal collimator of 3 m length. For the collimator settings see Table 3.2. These collimators are only moved from injection to flat top. Then, they keep the same position as at flat top until the beams are dumped.

### Collimators for experiments

Horizontal and vertical tertiary collimators (TCTH and TCTV respectively) are installed upstream of the triplet magnets near the experimental points. The triplets are quadrupoles used to reduce the beta function at the collision points (IR1, IR2, IR5 and IR8). The TCTs provide protection during the squeeze of the beam and the collision and reduce the halo-related background in the detectors. They are two-sided collimators with 1 m tungsten jaws.

Copper absorbers (TCL) protect the machine from particle showers (debris) coming from the collisions in IR1 and IR5, where a high luminosity is reached. After the energy ramp, the beam is squeezed in preparation of the physics operation. Unlike the other collimators, the TCTs are also moved in during the squeeze. Table 3.3 shows in detail the TCTs settings at injection, flat top and squeeze.

Table 3.2: Collimator settings for the different families in the cleaning hierarchy, expressed in units of the beam size  $\sigma$ , at different energies: 450 GeV (injection), 4 TeV (top energy in 2012), 7 TeV (expected top energy after long shutdown). The length and material for each collimator type is also stated; W stands for tungsten and CFC for Carbon Fiber Composite.

Location	Coll. type	Material	Length [m]	Half-gap [ $\sigma$ ]		
				450 GeV	4 TeV	7 TeV
IR7	TCP	CFC	0.6	5.7	4.3	5.7
	TCSG	CFC	0.6	6.7	6.3	6.7
	TCLA	W	1.0	10	8.3	10.0
IR3	TCP	CFC	0.6	8.0	12.0	12.0
	TCSG	CFC	1.0	9.3	15.6	15.6
	TCLA	W	1.0	10.0	17.6	17.6
IR6	TCSG	CFC	1.0	7.0	7.1	7.5
	TCDQ	CFC	3.0	8.0	7.6	8.0
IR1	TCT	W	1.0	13.0	26.0	26.0
IR2	TCT	W	1.0	13.0	26.0	26.0
IR5	TCT	W	1.0	13.0	26.0	26.0
IR8	TCT	W	1.0	13.0	26.0	26.0

Table 3.3: Collimator settings, expressed in units of the beam size  $\sigma$ , of the TCTs during injection, flat top and squeeze (for both 2012 and nominal operation)

Location	Coll. type	Half-gap [ $\sigma$ ]				
		450 GeV	4 TeV		7 TeV	
			Flat top	Squeeze	Flat top	Squeeze
IR1	TCT	13.0	26.0	9.0	26.0	8.3
IR2	TCT	13.0	26.0	12.0	26.0	8.3
IR5	TCT	13.0	26.0	9.0	26.0	8.3
IR8	TCT	13.0	26.0	12.0	26.0	8.3

### **3.2.3 Towards the future of LHC collimation system**

A future upgrade foresees to increase the LHC beam intensity. From there, the need of new collimators which can withstand even higher power loads from beam losses comes out and further improvements to achieve a higher cleaning efficiency are also required.

New techniques are under study and new proposals for the collimation system upgrade are under study, as for example the installation of crystal collimators [25, 26], electron lens [27], non-linear [28] or cryogenic [29] collimators.

# 4

## SixTrack Simulation Setup for Cleaning Inefficiency Studies

---

This chapter is dedicated to the main simulation tool which has been used for the single particle tracking studies: SixTrack[4]. In the next sections the extended version of SixTrack for collimation studies [30] is briefly introduced, describing the required inputs, the outputs and the other programs used to post-process the data. Then, it is described how SixTrack is used to assess the inefficiency of the LHC collimation system and to localize the area which is most exposed to proton losses.

### 4.1 SixTrack for collimation

SixTrack is a code written in Fortran 77. It tracks six-dimensional vectors of coordinates  $(x, x', y, y', s, E)$  and has a magnet system model which takes into account non-linearities up to the 20th order. At the very beginning, the purpose of SixTrack was to study non linearities and dynamic aperture in circular machines: then, it tracked pairs of particles through an accelerator structure over a large number of turns. Later the code was extended for tracking large numbers of halo particles which interact with collimators, thanks to the implementation of a new routine [30]. This version of the software became the standard tool for collimation studies at CERN.

#### 4.1.1 Particle tracking

In a SixTrack run, particles are tracked through the lattice element by element and their coordinates are transformed according to the type of element using a map derived from the electromagnetic field [10]. The definition of the beam line elements is read in from the output of the MAD-X [31] program, which is the standard tool for LHC beam optics calculations. The tracking method features a particular model to define the lattice, called *thin lens*. In Fig. 4.1 a comparison is shown between how an element looks like in the real lattice (top) and how it is sketched in the thin lens model (bottom). A marker is placed at the center of the element itself and a drift space replaces its whole length. The distance between two consecutive components is equal to the real distance between them plus the half length

of the two elements. Then, the elements have no longitudinal extension and the effect of a magnetic element on the beam is represented by an equivalent kick at the thin element location. It should be noted that in some cases, one thick element is split in several thin lenses for increased precision. The

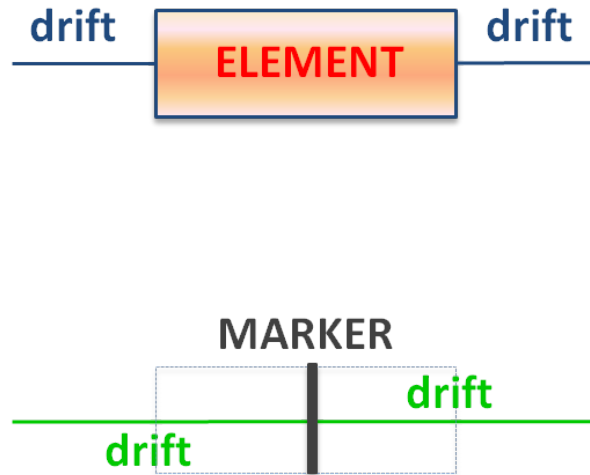


Figure 4.1: The thin lens formalism. On the top, an element in the lattice. On the bottom, the same element in the thin lens scheme.

main advantage of this formalism is to reduce the CPU computing effort that would occur as a results of thick-lens tracking.

When a particle hits a collimator jaw, it can undergo a number of different physical interactions. These effects are modelled by the scattering routine called K2 [31], based on the Monte Carlo method, which was implemented in an earlier code, called COLLTRACK. This code allows to track few millions of particles over hundreds of turn, with different halo and diffusion models, and simulate the proton-matter interactions inside the collimator materials, including ionization, multiple Coulomb scattering, point-like elastic and inelastic interactions and single-diffractive scattering (see Section 2.2.4). The program computes the distance between two consecutive interactions and evaluates if and where the particle left the collimator jaw. Particles showers due to inelastic processes are not followed: the code considers particles as "absorbed" at the position where an inelastic interaction occurs and removes them from the tracking. COLLTRACK is now implemented as a part of the source code of SixTrack.

### 4.1.2 Sixtrack input files

To perform SixTrack simulations, at least three different input files are needed:

- *fort.2*, generated by MAD-X, which defines the lattice of the machine and the normalized field strengths of the elements
- *Coll\_DB* (Collimator database) includes the details of each collimator (name, opening, material, geometry, etc)
- *fort.3* in which most of the tracking parameters (turns, number of particle, energy, etc) and collimator settings are found. A more detailed analysis of the file follows below.

Fig. 4.2 and Fig. 4.3 show some extracts of the *fort.3* file, which are relevant for the collimation studies. In particular, the block referring to the collimation routine is shown in Fig. 4.3.

```

-----
TRACKING
200 0 32 0 17 0 1
  1 1 0 0 0
0 0 1 1 1 20000 2
NEXT
-----

```

number of the turns to be tracked

Figure 4.2: Particle tracking parameters definition. Extract from *fort.3*.

If line (1) is set to TRUE, the routine is turned on. The number of particles to be tracked is given as a multiple of 64 particles. This number is defined in (2), together with the beam energy. In line (3) different initial distributions of the particles can be chosen. To generate the type of distribution to be tracked, a simplified approach is used: to reduce the computing time, the tracking can be performed only for an annulus distribution in phase space of the chosen plane (horizontal or vertical) representing the halo particles (see Fig. 4.4). The halo is generated at  $\pm\delta A_{x,y}$  around the amplitude  $A_{x,y}$ , in  $\sigma$  units (see Eq. 3.2), respectively in the horizontal and vertical planes.  $\pm\delta A_{x,y}$  is the smear and gives information about the "thickness" of the halo. Therefore, no computing time is lost tracking the beam core, which never hits any collimator. Diffusion effects are not included, instead the initial distribution relies on assumptions on the impact parameters on the collimators [32].

In the performed simulations (discussed in Chapter 5 and 6), the particles are distributed as a Gaussian cut at  $3\sigma$  in the other plane, perpendicular to the chosen collimation plane, between  $A_x \pm \delta A_x$  and  $A_y \pm \delta A_y$ ). Other types of distributions can also be read from external files. It is possible to

```

-----
COLLIMATION
(1) .TRUE.
(2) 100 450000
(3) 2 5.7 .0015 0. 0. "nothing" 1.129E-4 75.5
(4) .TRUE. 8. 9.3 15.6 10. 5.7 6.7 8.5 10. 900. 999.0 8. 7. 999.0
(5) 13. 13. 13. 13. 13. 13. 13. 13.
(6) 0 19789.0 20150.0 1 1
(7) -1.3899e-6 -9.345e-5 5.05324e-3 -1.6595e-2 2.15955e-2 -9.96261e-3 1.0
(8) -1.3899e-6 -9.345e-5 5.05324e-3 -1.6595e-2 2.15955e-2 -9.96261e-3 1.0
(9) 7.298e-9 7.298e-9
(10) .FALSE. .FALSE. 0 .TRUE. TCP.C6L7.B1 .FALSE. .TRUE. .TRUE. .TRUE.
(11) 0 0 0 0
(12) 0 0 0 0 0 0 0 0 0 .FALSE.
(13) .FALSE. 6.003 .0015
(14) 0 0 .FALSE. .FALSE.
(15) 0 .00213 0 0.288e-3 1
(16) "CollIDB_V6.503_lowb_st.b1.data" 1
(17) .TRUE. .FALSE. WAbsVertLowbcoll 101 1 1.
NEXT
-----

```

Packs of particles to be tracked

Particle energy [MeV]

Particle distribution parameters

Energy offset

Collimator half-gap

Emittance in H and V plane

Collimator database

Figure 4.3: Input to the SixTrack collimation routine. Extract from *fort.3*.

generate a distribution of particles with an initial energy spread, as better explained in Chapter 6. The collimators settings in  $\sigma$  units are defined in lines (4) and (5) for all collimators. Finally, line (9) hosts the value of the emittance in the horizontal and vertical planes.

### 4.1.3 Sixtrack output files and post processing

Using the required input files, SixTrack computes the trajectories of the halo particles along the machine. Scattered particle trajectories, in the 6-D phase space, are stored in the *tracks2.dat*. The particles are followed until they undergo an inelastic interaction with the collimator jaw and then it is considered absorbed. The output file *FLUKA\_impacts.dat* contains information about the transverse coordinates of these interactions along the jaw length. The ingoing and outgoing, transverse and longitudinal, coordinates hitting the collimator for the first time are listed in *FirstImpacts.dat*. From this file and *coll\_summary.dat*, which summarizes the number of impacting and absorbed protons for each collimator, an estimation of the impact

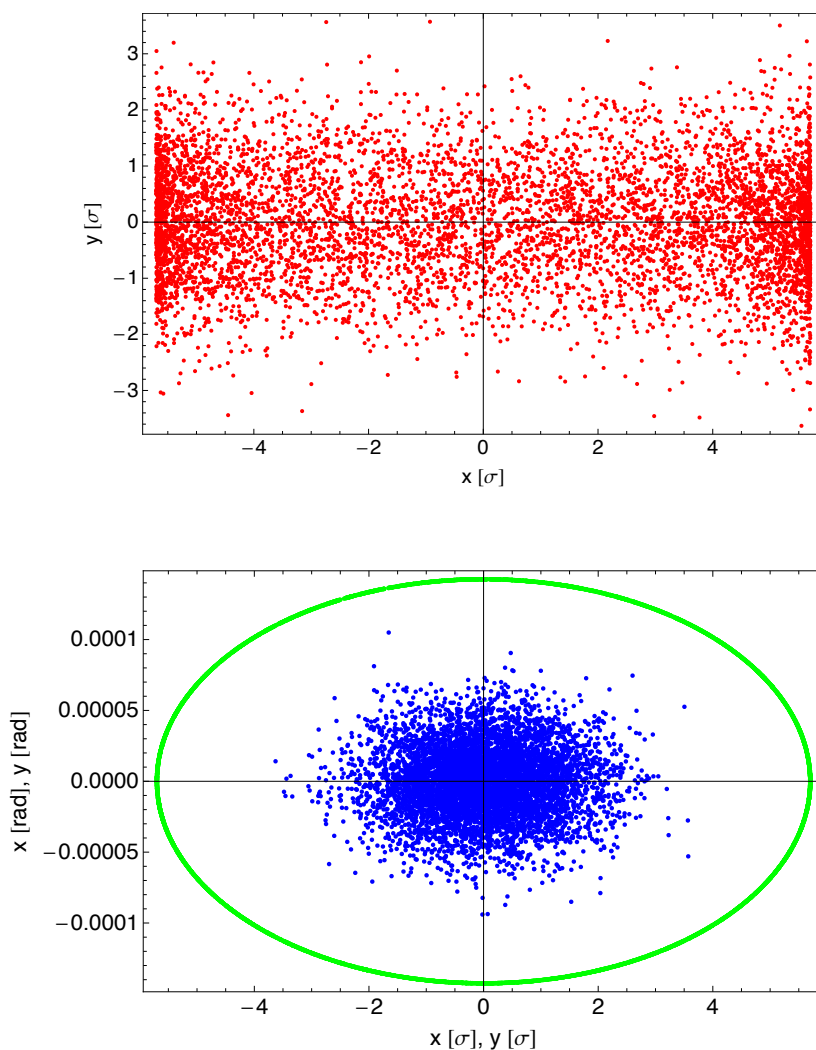


Figure 4.4: Particle distribution in different spaces: horizontal halo in the  $x$ - $y$  phase space (top) with annular distribution in the  $x$ - $x'$  (green) and Gaussian distribution in the  $y$ - $y'$  (in blue) phase space (bottom).

parameter  $b$  can be done:  $b$  is defined as the transverse offset between the impact location and the edge of the jaw. In addition, *collgaps.dat* includes the the optics and the opening of the collimators and, finally, an idea of the global cleaning inefficiency at different normalized amplitudes is contained in *efficiency.dat*.

Since SixTrack does not have an aperture model embedded in the code (due to CPU limits), post processing of the data is required to identify the particles which are lost in the machine outside collimators and localize the losses. The comparison between the particle trajectories from the SixTrack output file *tracks2.dat* and the aperture model is performed by the Beam-

LossPattern program [33]. This code looks for the elements where particles are lost and then tracks back their position until the loss point is found with an arbitrary resolution  $\Delta s$ . An example is shown in Fig. 4.5. One of the outputs coming out from this program is *LPI\_PartLost.dat*, where the 6-D phase space coordinates are stored for each particle that hits an aperture. This file provides the input for another program, called *CleanInelastic*: it cleans up the *FLUKA\_impacts.dat* from the fake absorptions due to particles formerly lost in the machine aperture, keeping only the information about particles absorbed in the jaw through inelastic interactions that have not hit the aperture before. The new results are written in the *impacts\_real.dat*. Energy deposition studies based on the analysis of this file are usually performed by FLUKA code [34, 35, 36]: it calculates the showers of particles generated by the inelastic interaction of the primary protons with the different collimator jaw materials. A sketch of the simulation chain, including the main inputs and output is showed in Fig. 4.6.

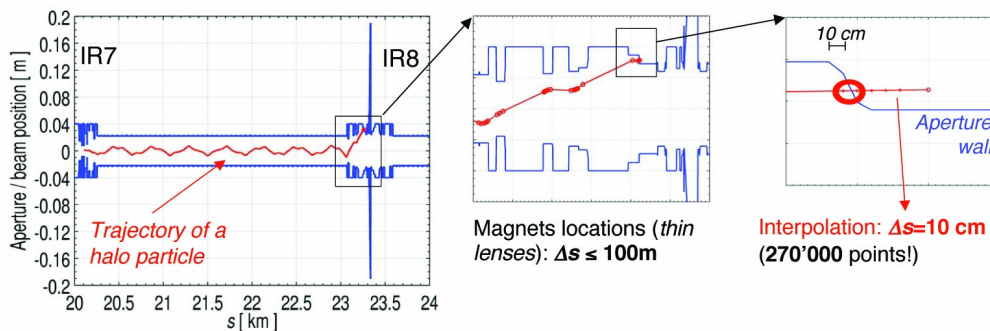


Figure 4.5: Example of a trajectory of a particle lost in IR8 in the LHC [30].

## 4.2 Cleaning inefficiency and beam loss maps

Particle losses can limit the normal machine operation or even damage some equipment, especially in accelerators with superconducting magnets, which are particularly sensitive to even small amounts of energy deposition, that could make them quench. Therefore, it is important to provide a realistic estimation of the expected beam losses along the ring.

Thus, Sixtrack code can thus be used to draw detailed maps of loss location along the whole LHC ring for different optics and collimator settings. These plots, called *beam loss maps*, are built applying the definition of local cleaning inefficiency  $\eta_c$ , introduced in Eq. 2.45, with a  $\Delta s=10$  cm resolution. Fig. 4.7 (a) shows an example of a typical loss map around the ring; a zoom of the betatron cleaning insertion (IR7) is shown in Fig. 4.7

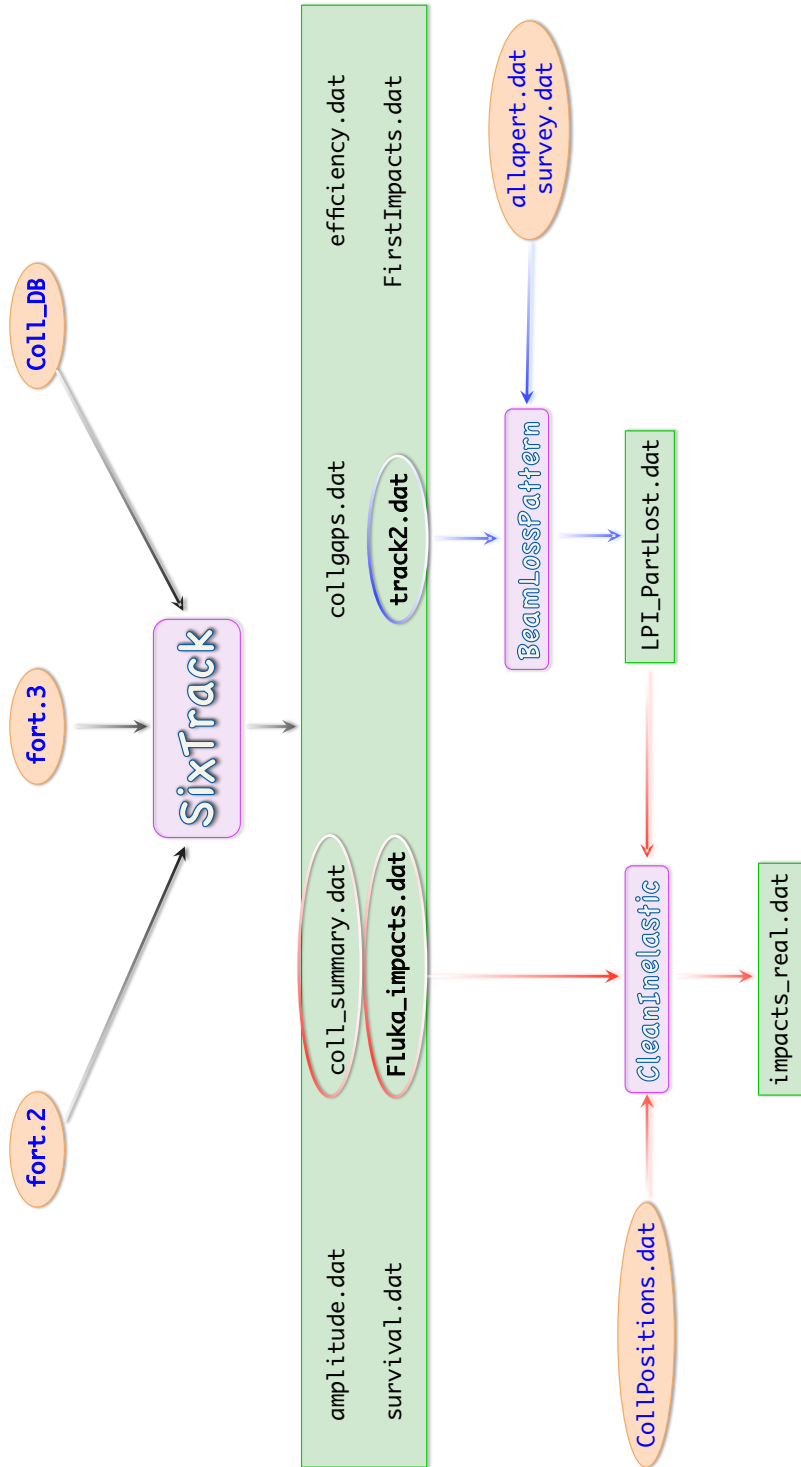


Figure 4.6: SixTrack simulation path.

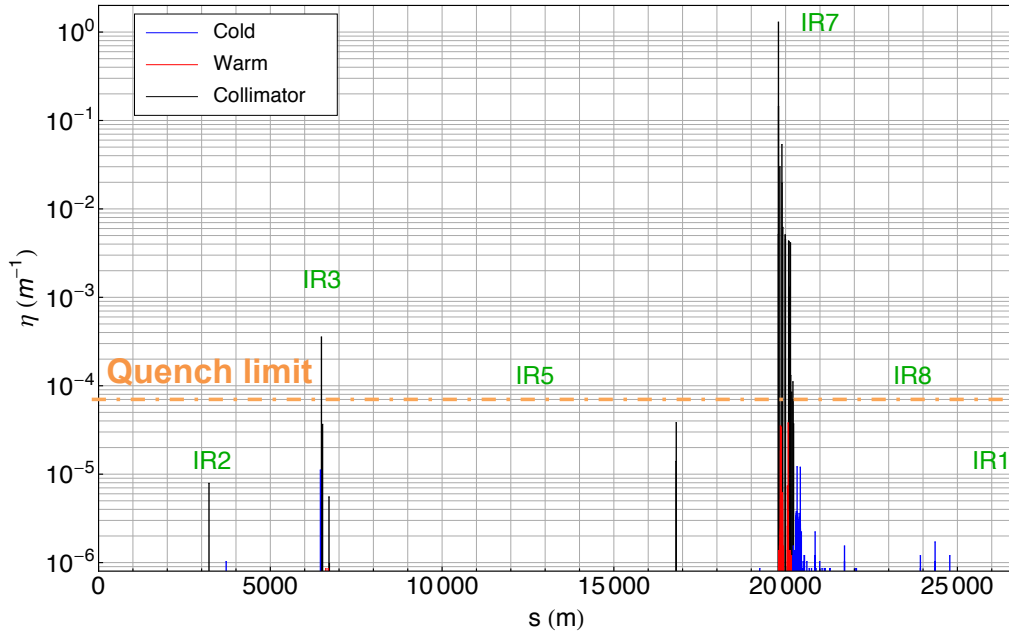
(b): the blue peaks refer to the location of proton losses in superconducting elements (cold losses), while the red ones identify losses in normal conducting magnets (warm losses). In order to prevent possible quench in the SC magnets following high beam loss, the blue bars must not exceed the quench limit line. To determine the quench limit at 4 TeV, Eq. 2.46, with  $R_q = 1.9 \times 10^7 \text{ps}^{-1} \text{m}^{-1}$  [11],  $\tau=0.2 \text{h}$  and  $N_{tot}$  calculated from Table 3.1. Using these values, a quench limit of  $7 \times 10^{-5}$  is obtained. The gray peaks in Fig. 4.7 (a) show the particles which are performed inelastic interactions in the collimators. From Fig. 4.7 (b) it can be seen that the most critical area in terms of losses is the region downstream of IP7 (for Beam 1): this area is called *Dispersion Suppressor* (DS): it consists in a lattice cell with one dipole magnet missing and reduces the dispersion function (see Section 2.1.3) inside the insertion regions.

### 4.3 Benchmarks of SixTrack code

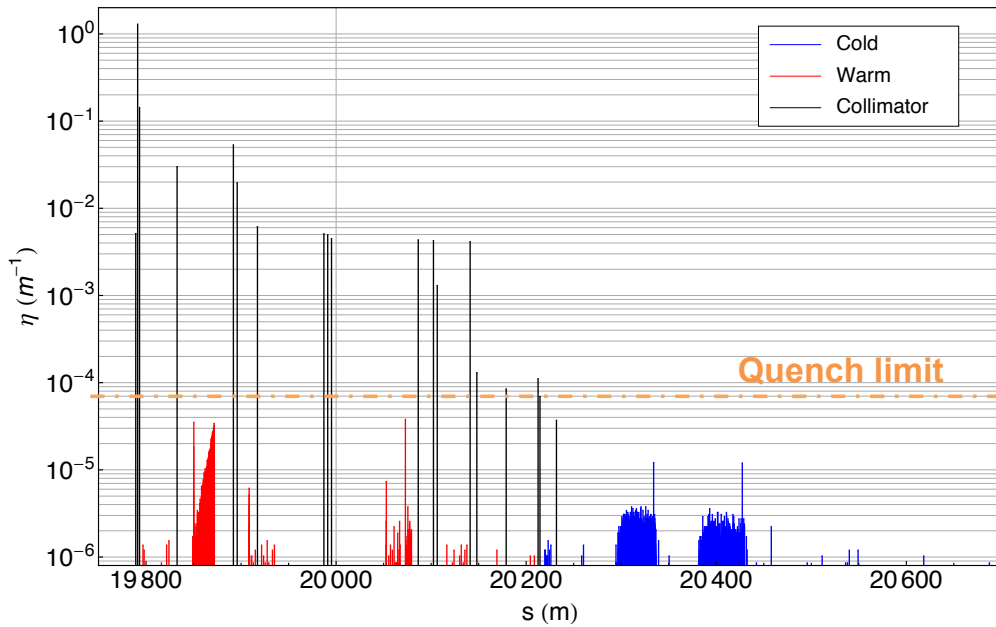
A first benchmark of SixTrack code was done with beam tests in 2004 [37]. The beam tests were performed in the SPS with an LHC prototype collimator. In Fig. 4.8 the results of Beam Loss Monitor (BLM) measurements in the SPS and the comparison with beam loss simulations are shown. Although a good agreement between measurements and simulation can be established, a longitudinal shift between them is anyhow observed. It has a fully expected reason, due to the fact that only inelastic impacts by primary halo are considered in the simulations (neglecting the showers), while the BLMs record mainly the signal of the showers generated by the inelastic interactions in the elements.

To have new evidence to support the reliability of the simulations, another study was performed in 2011, this time involving the LHC during the operation at 3.5 TeV [38]. Fig. 4.9 shows the losses around the ring of Beam 1 in the horizontal plane as simulated by SixTrack (top) and measured during a qualification loss map on April 2011 (bottom).

Qualitatively, an excellent agreement can be established between simulations and measurements. The main losses occur in the collimator cleaning insertions (IR7 and IR3) and decay along the insertion itself. However, as already said for the 2004 SPS tests, quantitative deviations in the height of the peaks can be observed comparing simulated and measured data: the BLMs do not measure the direct proton losses shown for the simulation, instead they record the showers produced by them. Therefore, in order to allow also the quantitative comparison between SixTrack results and BLMs signal, Monte-Carlo simulations with the program FLUKA [34, 35, 36] have been done to simulate the showers at some selected locations [38]. The re-



(a) Full ring



(b) Betatron cleaning insertion IR7

Figure 4.7: Simulated beam loss map at 4 TeV for Beam 1 in the horizontal plane. Simulation done using the injection optics at flat top and the standard 2012 collimator settings as defined in Table 3.2 and 3.3

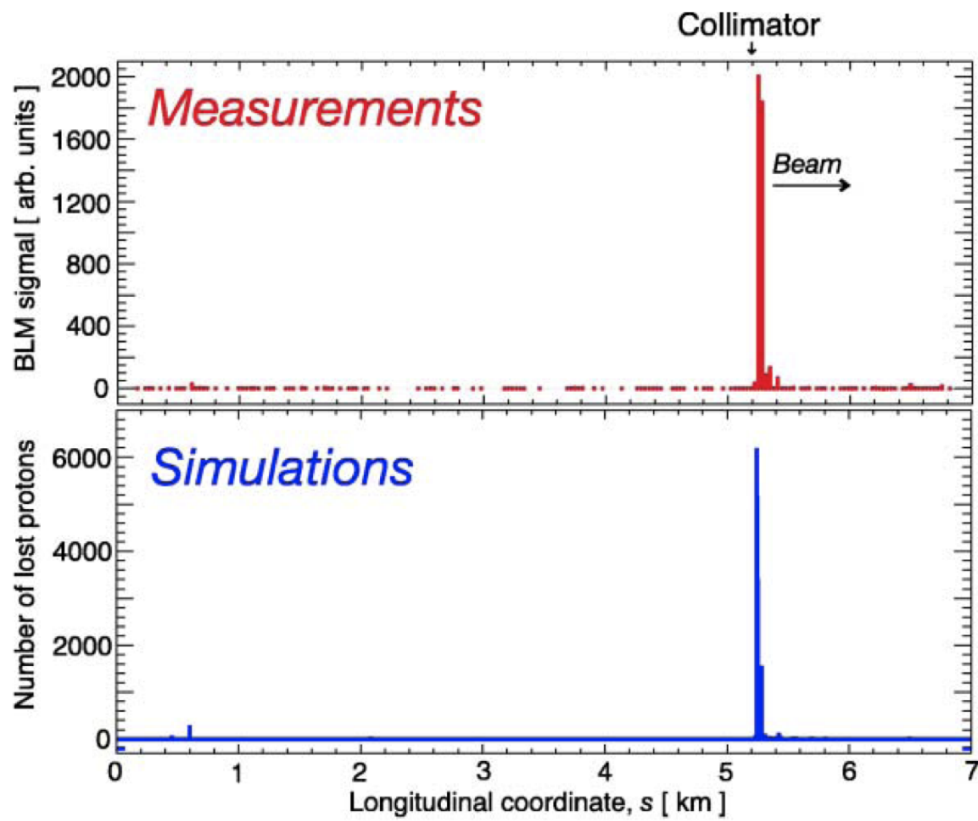


Figure 4.8: Measured and simulated SPS Beam Loss responses along the full ring [37].

sults from the combined simulations (SixTrack + FLUKA) are now closer to the measured losses and they also well reproduce the loss pattern, as the example of the TCTs in Fig. 4.10 shows.

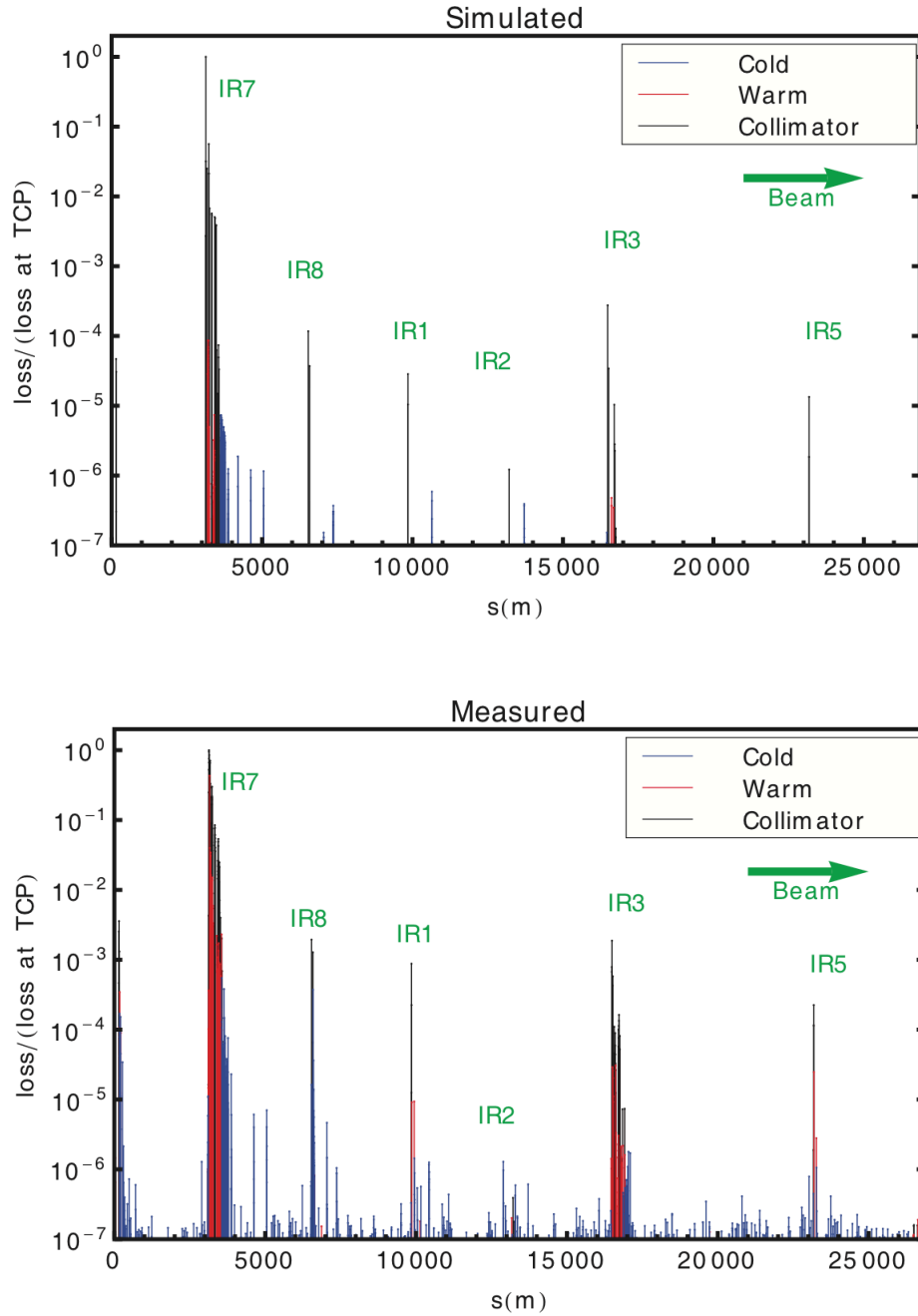


Figure 4.9: Simulated beam losses from SixTrack (top) and measured BLM signals on April 2011 (bottom). Only losses from Beam 1 in the horizontal plane are shown. The initial losses occur in both cases in the horizontal plane in B1. Both simulations and measurements are normalized to the highest loss [38].

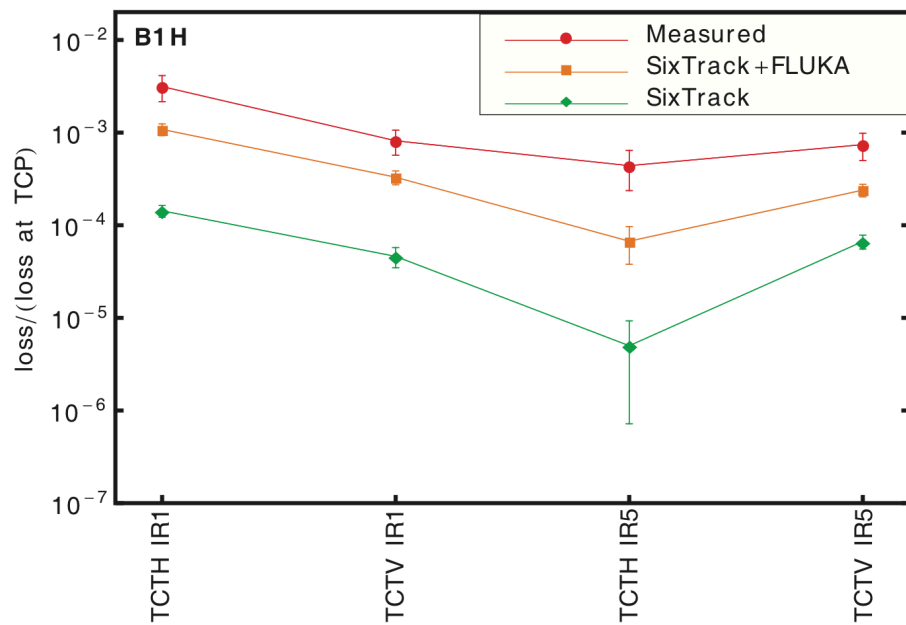


Figure 4.10: Comparison of proton losses on horizontal and vertical TCTs respect to the TCPs between measurements in 2011 and SixTrack simulations, including and not including FLUKA results [38].

# Collimation Cleaning Performance in the LHC Energy Ramp

---

The cleaning inefficiency of the LHC collimation system for the operational scenarios in 2010-12 has already been studied in detail at injection and top energy, 450 GeV and 7 TeV respectively [10, 11] and also at the operational top energy during the first part of the first LHC run in physics conditions [38]. In this chapter, the results are presented for the cleaning inefficiency at intermediate energies, simulated using the SixTrack code. The first comparisons with measured provoked losses at these energies are also discussed. This study helps in benchmarking the energy dependence of the simulated inefficiency and to estimate the uncertainties in the simulation. This helps when to predicting the cleaning performance of the collimation system for future operation at higher energies and, consequently, the 7 TeV scenario is the focus of the last part of this chapter.

## 5.1 SixTrack simulatios: setup and procedure

### 5.1.1 Energy and Collimator Setting Changing

A first set of simulations has been run considering eight different energies between 450 GeV and 4 TeV at steps of 500 GeV, in which the positions of the collimators follow the same function of energy as in the machine [39]. To speed up the preparation of the SixTrack input, a Mathematica script has been implemented to automatically generate the *fort.3* input for each energy.

In the simulations, 2012 settings [40], summarized in Table 5.1 for injection and top energy, have been used to set the collimator half gap at the start and end points. The collimator half gaps (in  $\sigma$ ) at intermediate energies are obtained by linear interpolation of the values from injection to flat top, as shown in Fig. 5.1. The collimators are at all times assumed centered around the ideal orbit and the LHC injection optics was used at all points (the squeeze to smaller  $\beta$ -functions in the experiments occurs later).

As a first study,  $6.4 \times 10^6$  particles were tracked for 200 turns for each

Table 5.1: Collimator settings used in SixTrack simulations. The collimator half-gap at injection, 1 TeV, 2 TeV, 3 TeV and 4 TeV are listed.

Location	Collimator type	Half-gap [ $\sigma$ ]				
		450 GeV	1 TeV	2 TeV	3 TeV	4 TeV
IR3	TCP	8.0	8.62	9.75	10.9	12.0
	TCSG	9.3	10.3	12.1	13.8	15.6
	TCLA	10.0	11.2	13.3	15.5	17.6
IR7	TCP	5.7	5.48	5.09	4.69	4.3
	TCSG	6.7	6.64	6.53	6.41	6.3
	TCLA	10.0	9.74	9.26	8.78	8.3
IR6	TCSG	7.0	7.02	7.04	7.07	7.1
	TCDQ	8.0	7.94	7.83	7.71	7.6
experiments	TCT	13.0	15.0	18.7	22.3	26

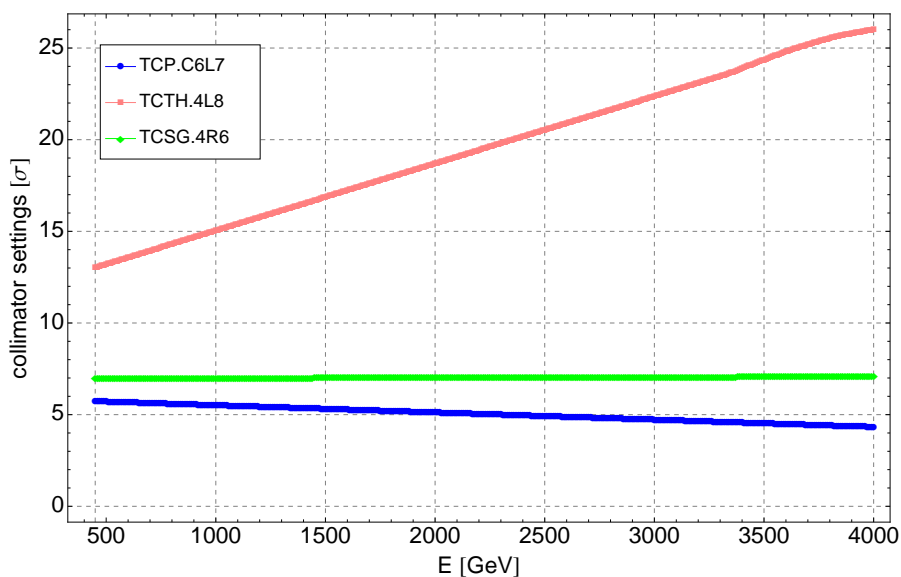


Figure 5.1: Collimator settings during the energy ramp.

energy. The beam halo was generated as described in Chapter 4 and Fig. 4.4 by defining a particle distribution with an amplitude high enough to hit the primary collimators installed in the betatron cleaning insertion in IR7. Therefore, the amplitude of this distribution is equal to the TCP half-gap with a uniform spread of  $0.0015 \sigma$  (smear) around this value. Simulations have been performed for both beams and with the initial loss in both the horizontal and vertical planes. In the next pages, only the results for Beam 1 and horizontal losses are shown in order to compare with the data available

from the measurements.

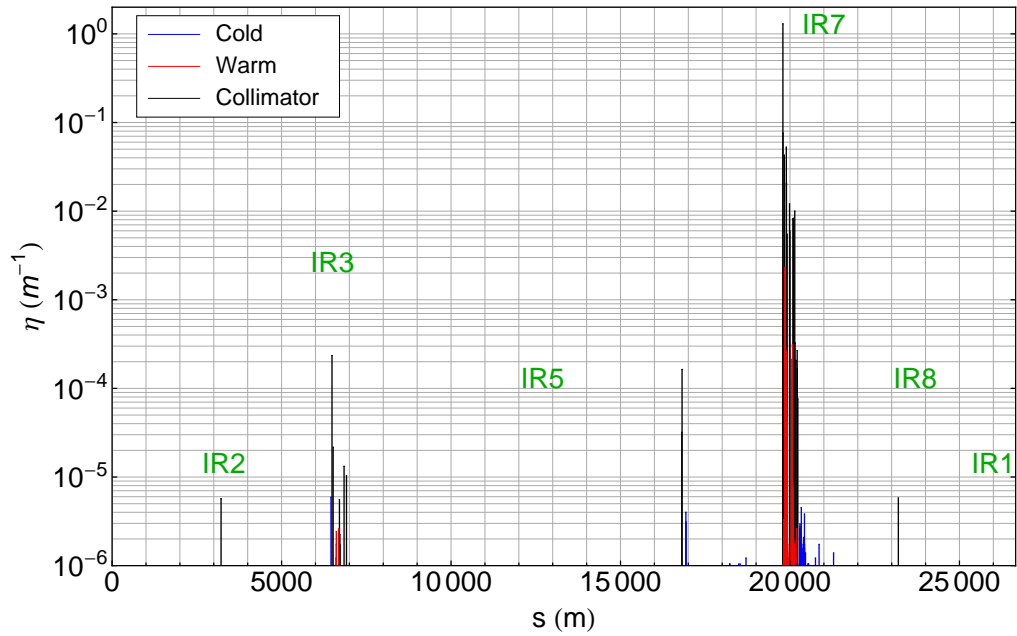
An example of the distribution of the losses along the ring obtained by a SixTrack simulation at 2 TeV is shown in Fig. 5.2. In Appendix A the loss maps at all the simulated energies are shown. As for the example shown in Fig. 4.7, the highest losses occur on the collimators in IR7; important losses appear also in the off-momentum insertion IR3 and in IR6, where the local ratio of particles lost is above  $10^{-4}$  of the level in IR7. The highest losses in cold magnets occur in the dispersion suppressor (DS) downstream of IR7.

The most important part for evaluating the collimation performance is the leakage of losses to cold magnets that could risk to quench. Therefore, the simulated highest local cleaning inefficiency (for the definition see Eq. 2.45) in the cold parts of the machine, as function of energy and taken over 10 cm bins, is shown in Fig. 5.3. This highest value of  $\eta_c$  in the cold regions occurs in each simulation in the DS downstream the IR7 cleaning insertion. For each point, the statistical error from the simulation is also shown. This error has been calculated by assuming that the number of particles lost in a certain bin in the simulation follow a Poisson distribution, where the standard deviation is the square root of the expectation value.

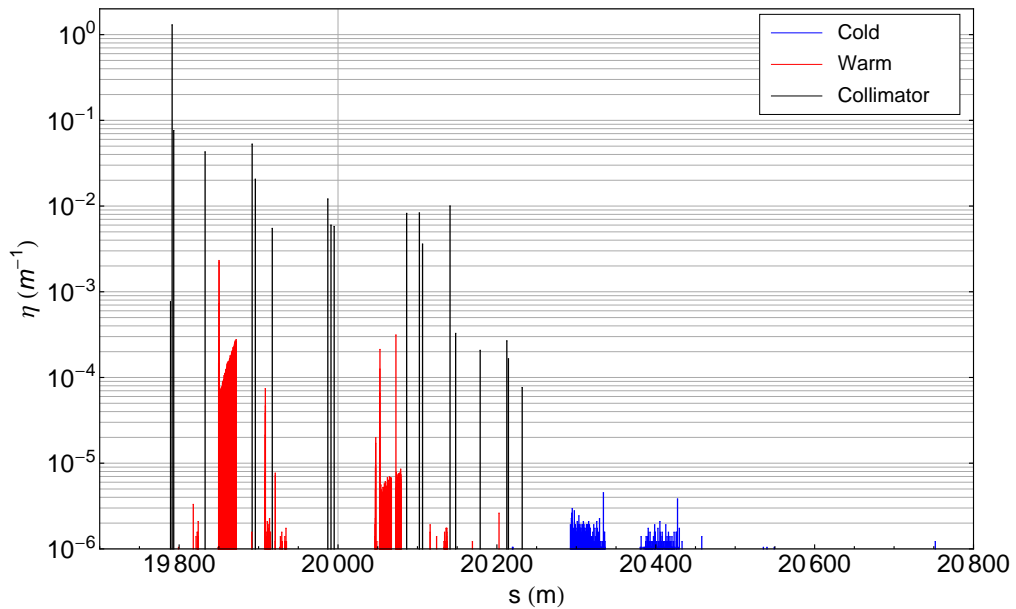
In order to decrease the statistical error, the simulations have been re-launched using the same parameters, but with one order of magnitude more particles tracked ( $64 \times 10^6$  per energy). Fig. 5.4 shows the cleaning inefficiency for this case: the trend is similar to the one in Fig. 5.3 within the statistical errors. The most pronounced difference is that the inefficiency seems to increase slower between 3 and 4 TeV with respect to the previous case. Obviously, a reduction of the error bars for each point can be easily established.

Various factors may affect the efficiency of the collimation system: the proton energy, the collimator positions and the impact parameters of the particles inside the jaw. In order to have a more complete understanding of the quantitative influence of these aspects on the collimation performance and the inefficiency trend in Fig. 5.3, several simulations have been run, varying different parameters.

Fig. 5.5 shows the average impact parameter as function of the energy, obtained from the above simulations, where the smear parameter (in  $\sigma$ ) was unchanged. In Fig. 5.6, instead, the distribution of  $b$  at injection and 2012 flat top energy is presented. From this plot the different distribution in the two cases is evident: the large spread at 450 GeV, which leads to an average impact parameter of about  $58 \mu\text{m}$  is much smaller at 4 TeV, where the particles hit the collimator within the first  $10 \mu\text{m}$ . As the real impact distribution in the machine is not well known, the difference in impact parameters might risk to introduce potentially unphysical results.



(a) Full ring



(b) Betatron cleaning insertion IR7

Figure 5.2: Simulated beam loss map at 2 TeV for Beam 1 in the horizontal plane.

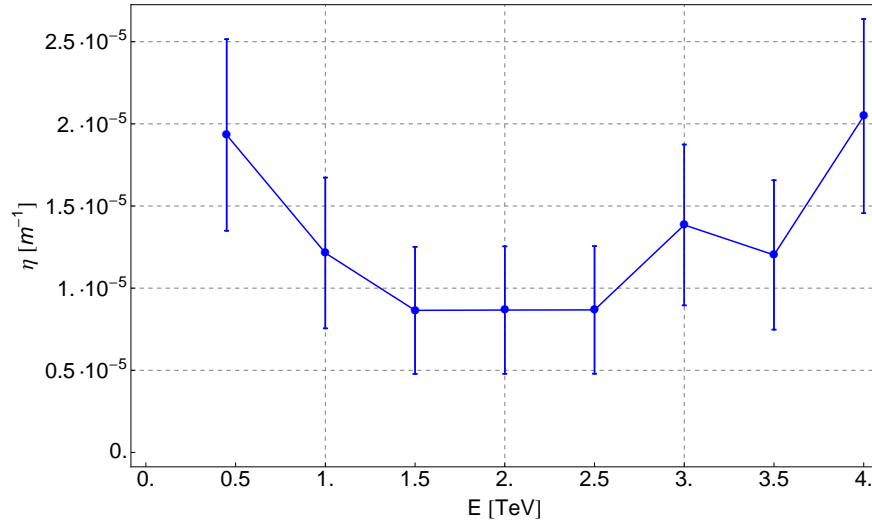


Figure 5.3: Highest local cleaning inefficiency in the cold parts of the machine, found in the IR7 DS, as function of energy. In the SixTrack simulation,  $6.4 \times 10^6$  particles were tracked.

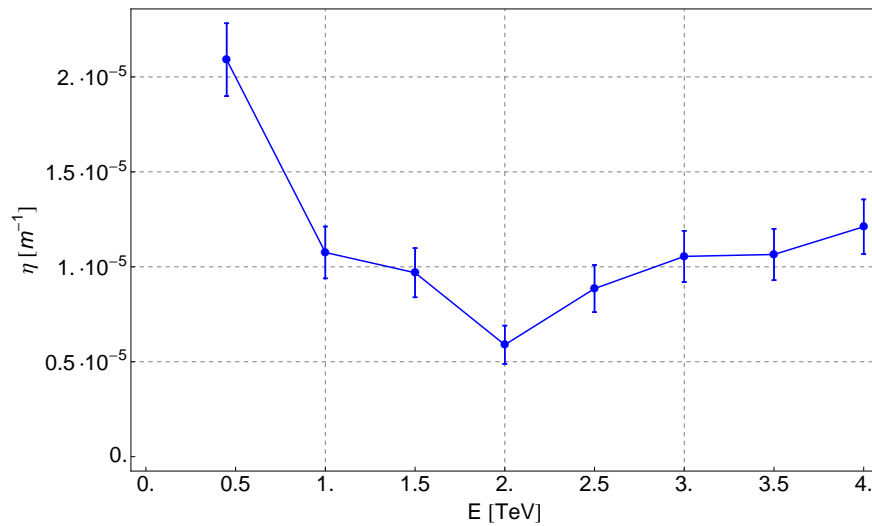


Figure 5.4: Highest local cleaning inefficiency in the cold parts of the machine, found in the IR7 DS, as function of energy. In the SixTrack simulation,  $64 \times 10^6$  particles were tracked.

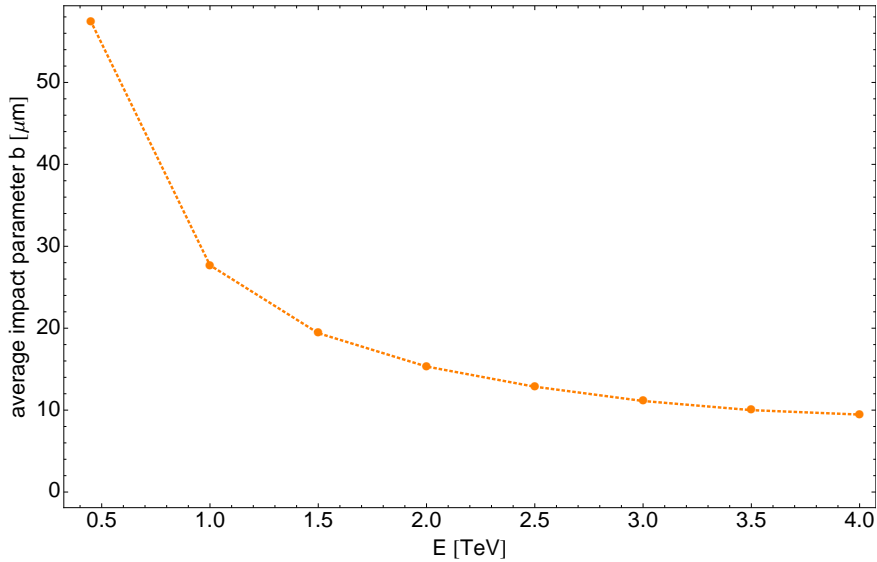


Figure 5.5: Average impact parameter  $b$  on the horizontal TCP as function of energy from SixTrack simulations done using the settings shown in Table 5.1

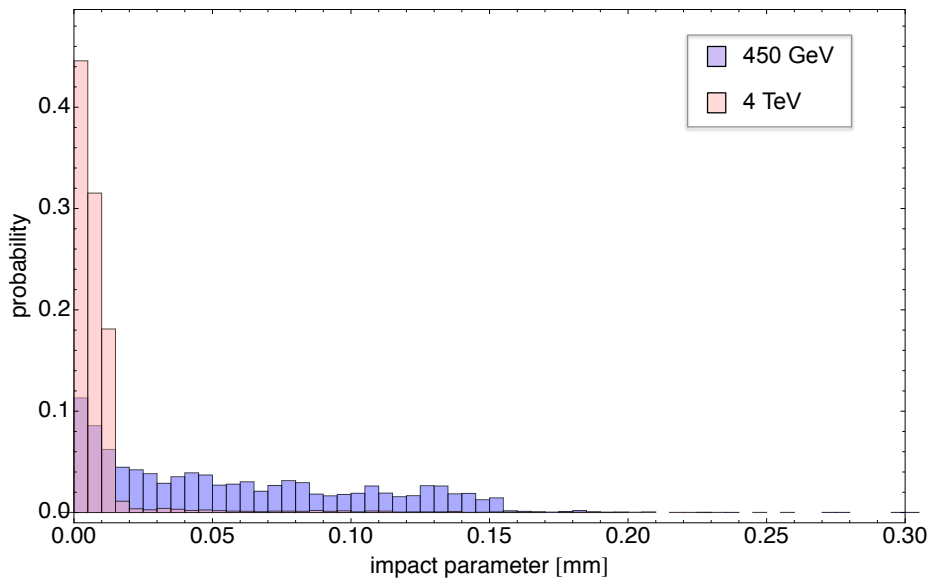


Figure 5.6: Distribution of the impact parameter  $b$  along the IR7 TCP at injection and top energy. In the histogram the blue bars refer to the distribution of  $b$  at 450 GeV and the pink ones at 4 TeV.

Therefore, the influence of the impact parameter has to be studied in detail.

In order to understand the influence of  $b$  on the collimation cleaning inefficiency, a new simulation has been run at 4 TeV, modifying the smear

of the beam halo (in SixTrack *fort.3* input file) to keep the same impact distribution as at injection. Several tries have been done to find the new smear to be used and at the end the value of  $0.4957 \sigma$  has been chosen: with this value, the new distribution obtained for  $b$  at flat top follows rather well the behaviour at 450 GeV (see Fig. 5.7). It should be pointed out that the impact parameters cannot easily be calculated directly, as the non-linear fields of the sextupoles in the machine are important at the high amplitudes considered. They deform the linear phase space over the turns it takes for the tracked particles to reach the collimators. Therefore, a trial-and-error method was used to find a the smear parameter that reproduces the 450 GeV distribution. For the same reasons, it is non-trivial to analytically estimate the needed smear parameter as a function of energy that would keep the impact distribution on the collimators unchanged.

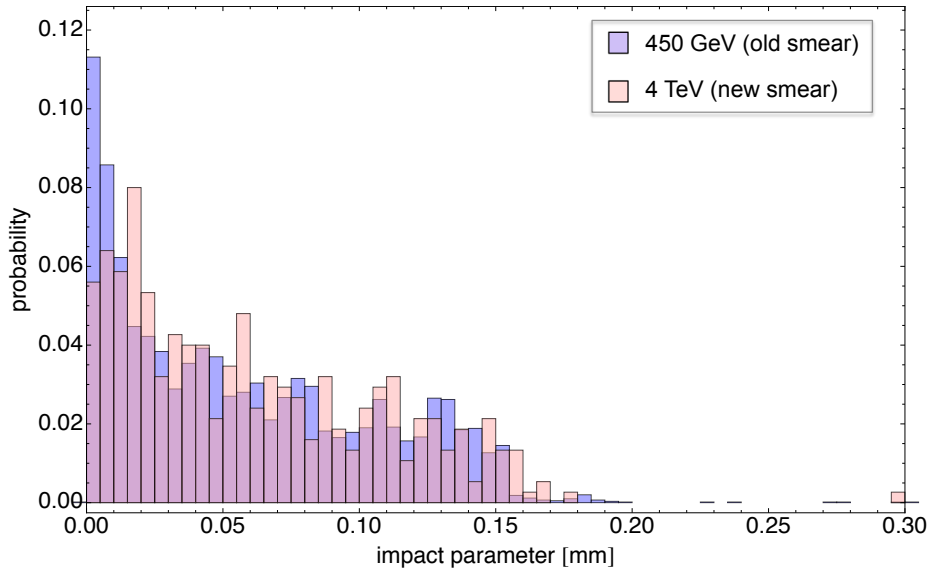


Figure 5.7: Distribution of the impact parameter  $b$  along the IR7 TCP at 450 GeV (halo smear:  $0.0015 \sigma$ ) and at 4 TeV (halo smear:  $0.4957 \sigma$ ). In the histogram the blue bars refer to the distribution of  $b$  at 450 GeV and the pink ones at 4 TeV.

Analysing the results of 4 TeV simulations with the new smear, it is emerged that a 20% error is introduced in the inefficiency calculated considering particle losses integrated over about 20 m in the IR7 DS (Fig. 5.8). As concerning the peak loss taken over 10 cm bins along the ring, the error is within the amplitude of the statistical error bars shown in Fig. 5.3. For our purpose we cannot say that the modification to the impact parameter does not affect at all the simulation results, but however the error coming from the constant smear simulations (which Fig. 5.3 refers to) is compara-

ble with the statistical one. Moreover, at intermediate energies between the injection and the end point it is also reasonable to expect an error less than the 20% found in the 4 TeV case. A possible future improvement could be to run simulations where the smear changes as function of energy in order to keep the impact distribution constant at all the energies.

At a later stage, separate simulations have been performed by varying only the energy or the position of the collimator jaws to isolate the effects of the energy dependence of the particle scattering and the collimator movements with respect to the aperture.

### 5.1.2 Collimator Positions Changing Only

In these simulations, the energy of the particles tracked is kept constant at 450 GeV, as well as the impact parameter ( $58 \mu\text{m}$ ), while the collimators are moved like in a normal energy ramp. It means that a collimator, even if the beam energy is 450 GeV, is set to the position (in mm) that it should have at the equivalent energy in the ramp. The collimator half opening is calculated using Eq. 3.3 but where the  $n_\sigma$  is scaled by a factor:

$$n_\sigma = n_{(\sigma, E)} \frac{\sigma_E}{\sigma_0} = n_{(\sigma, E)} \sqrt{\frac{\gamma_0}{\gamma_E}} \quad (5.1)$$

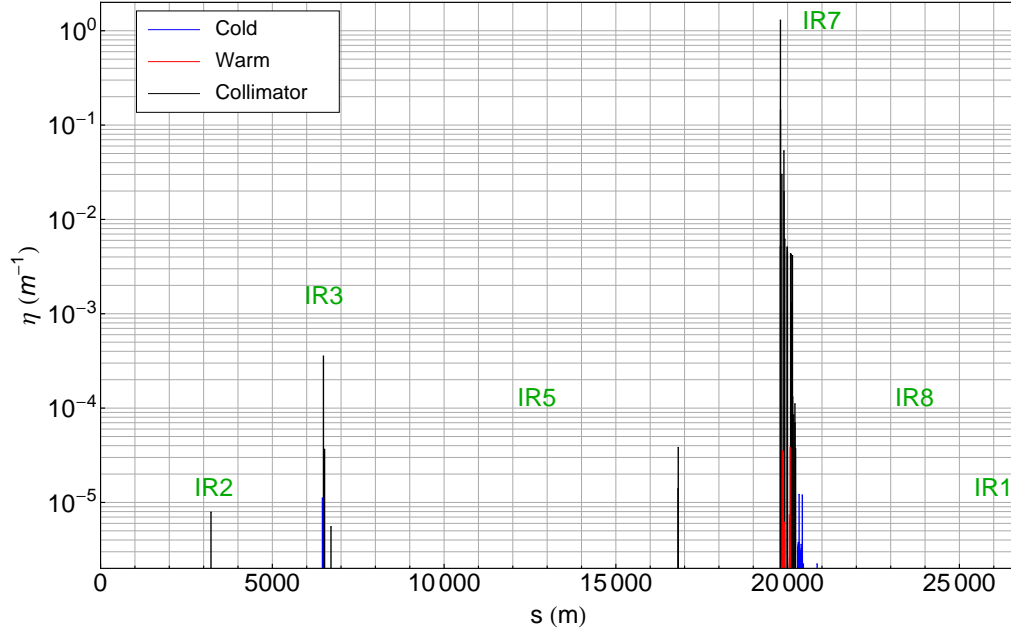
where the subscript 0 refers to 450 GeV and  $E$  to the equivalent energy.

The result of the simulations shows, as expected, a decreasing trend of the cleaning inefficiency with the increase of the equivalent energy (see green dotted line in Fig. 5.9). This can be understood from the fact that the scattering physics is unchanged due to the constant energy, while the collimators move closer to the beam center as in a normal ramp. They are therefore farther away from the aperture, and the scattering angles required to reach the aperture are larger. Protons receive similar kicks in all cases once they hit the primary collimator and, even if not absorbed in the secondaries, they can continue their trajectory—at a lower amplitude than if the collimators would have been more open—without hitting the aperture. They can then be absorbed by the collimators on a subsequent turn.

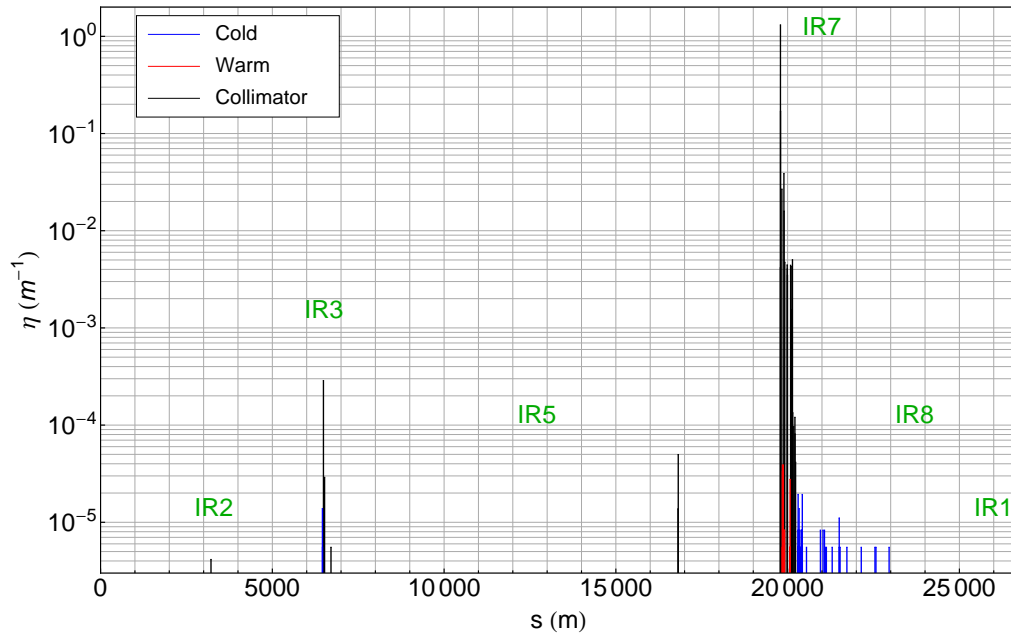
### 5.1.3 Energy Changing Only

An other possibility is to simulate a normal energy ramp, but keeping the collimator half-gaps constant at their position in mm at 450 GeV. Now the  $n_\sigma$  is given by:

$$n_\sigma = n_{(\sigma, 0)} \frac{\sigma_0}{\sigma_E} = n_{(\sigma, 0)} \sqrt{\frac{\gamma_E}{\gamma_0}} \quad (5.2)$$



(a) Simulation at 4 TeV (halo smear:  $0.0015 \sigma$ )



(b) Simulation at 4 TeV (halo smear:  $0.4957 \sigma$ )

Figure 5.8: Simulated beam loss map at 4 TeV for Beam 1 in the horizontal plane with different halo smear parameter.

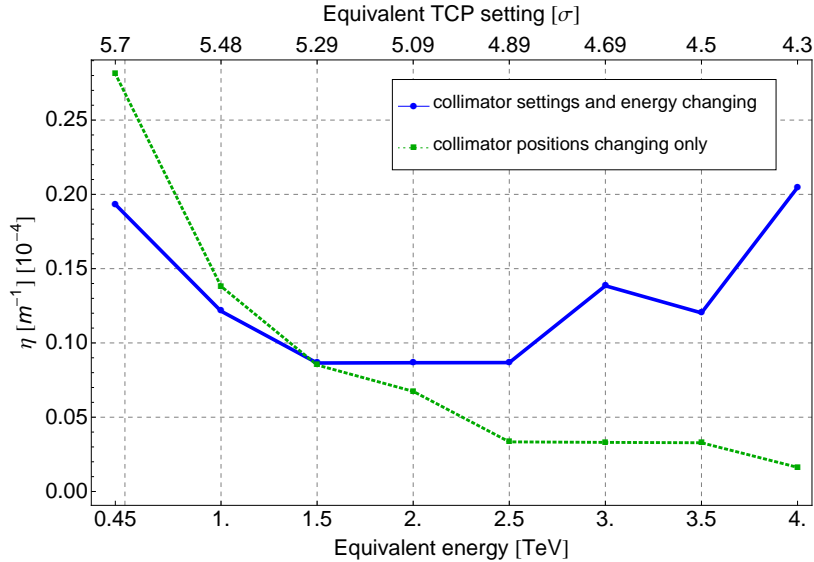


Figure 5.9: Cleaning inefficiency at IR7 DS (Q8) during the energy ramp with standard simulations shown in Fig. 5.3 (blue) and keeping the energy constant but the collimators moving like in a normal ramp (green)

From the analysis of the simulation results, the efficiency of the system worsens with the energy (see red dotted line in Fig. 5.10). The change of the particle-matter interactions inside the jaw could explain this behaviour: the scattering angles from single diffractive and nuclear elastic scattering decrease with energy (meaning a lower probability of scattering onto the TCSs) while the interaction cross-sections increase slightly [11]. The combined effect is that more particles are scattered but at smaller angles, and many of these particles are later lost due to their energy offsets in the DS where the dispersion starts to increase. Therefore, more particles are lost on the aperture and the inefficiency increases. The result is compatible with a related study in Ref. [11].

From the comparison of the three different cases which have been simulated by SixTrack shown in Fig. 5.11, one can qualitatively understand how the two effects (change in collimator settings or scattering physics) counteract each other and that the full simulation is found in between. The starting points of the three lines agree within the statistical error.

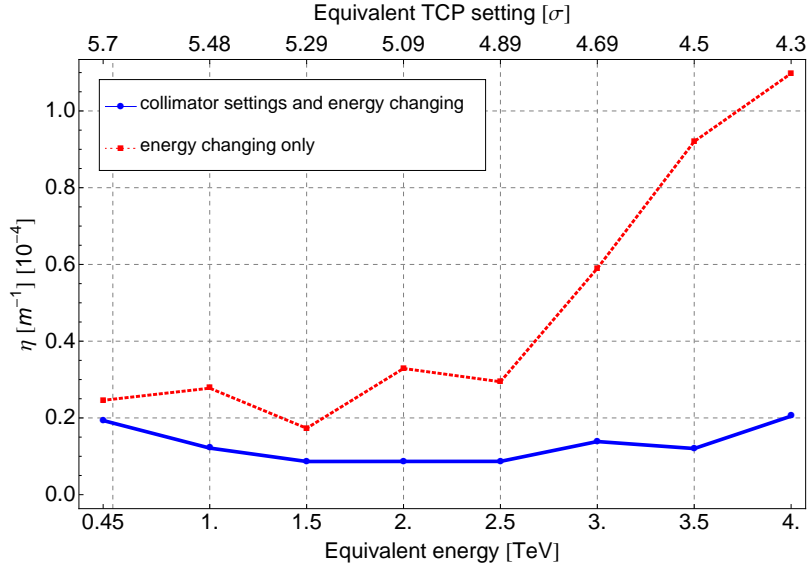


Figure 5.10: Cleaning inefficiency at IR7 DS (Q8) during the energy ramp with standard simulations (blue) shown in Fig. 5.3 and keeping collimator half-gap in mm constant but the energy changing (red).

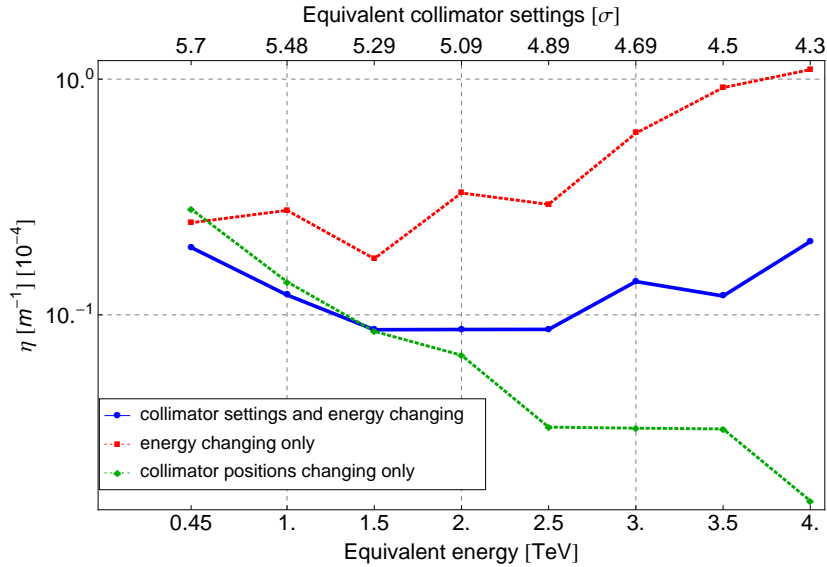


Figure 5.11: Comparison of cleaning inefficiency at IR7 DS (Q8) during the energy ramp in different simulated conditions: standard simulations, energy constant and mm collimator half-gap constant case studies.

## 5.2 Beam loss measurements in the LHC energy ramp

To understand how close the simulation results are to the real behaviour of the machine, data taken during dedicated measurement sessions at the LHC in 2012 have been used to benchmark the simulations.

The measurements were performed by first injecting a low-intensity beam, consisting of a few different bunches, and then accelerate the beam to top energy. During the acceleration, losses can be provoked by with the transverse damper (ADT) [41]: this system provides a bunch-by-bunch excitation that makes the particle amplitudes larger and pushes them onto the collimation system in order to provoke fast beam losses. The excitation can be performed repeatedly during the ramp at several different energies.

The beam loss data were recorded during the excitations by the BLM (Beam Loss Monitor) system [42]: it is composed of ionization chambers, with parallel aluminium electrode plates (see Fig. 5.12), located about 1 m downstream of the most likely loss locations along the ring. The main parameters of the ionization chambers used in the BLM system are listed in Table 5.2.

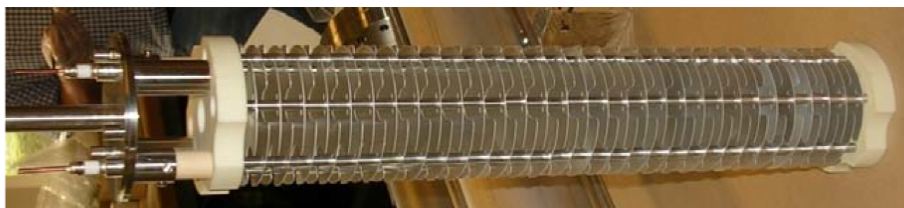


Figure 5.12: Inside of one ionisation chamber of the LHC BLM system [42]. The stack of aluminum electrodes with the insulator ceramics at both ends are well visible.

A first measurement attempt was done in October 2012. The excitation was performed every 0.5 TeV. An example loss map at 2 TeV is shown in Fig. 5.13. As can be seen, the background noise level is in many parts of the ring higher than the losses that need to be resolved. This comes from the fact that the excitation was not strong enough—it has to be tuned well in order to achieve losses well above the background level but not high enough to lose all particles at once or provoke a beam dump.

In order to improve the measurements, a second data taking session was organized in November 2012. In this session, four nominal LHC bunches of  $1.1 \cdot 10^{11}$  protons and four pilot bunches with intensity  $2 \cdot 10^{10}$  were injected.

Table 5.2: Main parameters of the LHC ionization chambers [42].

Parameter	Unit	Value
Diameter	[cm]	9
Length	[cm]	50
Sensitive volume	[l]	1.5
Electrodes material		alluminium
Electron collection time	[ns]	300
Ions collection time	[ $\mu$ s]	80
Filling gas		N <sub>2</sub>
Gas pressure	[mbar]	100
Operation voltage	[kV]	1.5

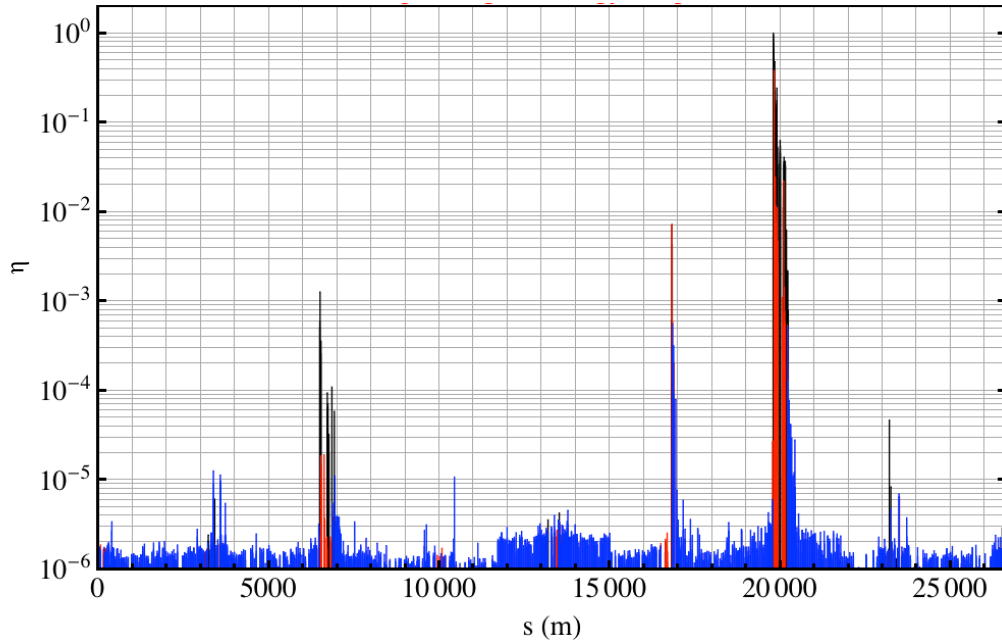


Figure 5.13: Beam loss map at 2 TeV from BLMs signal taken in the LHC in October 2012. The noise background is evident.

For the two beams, repeated excitations at different energies were performed with the transverse damper. As Fig. 5.14 shows, excitations with a duration of four seconds were done in the horizontal plane during the ramp close the energies used in the simulations, alternatively for Beam 1 and Beam 2. For the scope of this work, only the data concerning Beam 1 are analyzed, since the provoked losses in Beam 2 resulted not strong enough to obtain BLM signals sufficiently above the background level.

Fig. 5.15 shows an example of the signal recorded by the beam loss

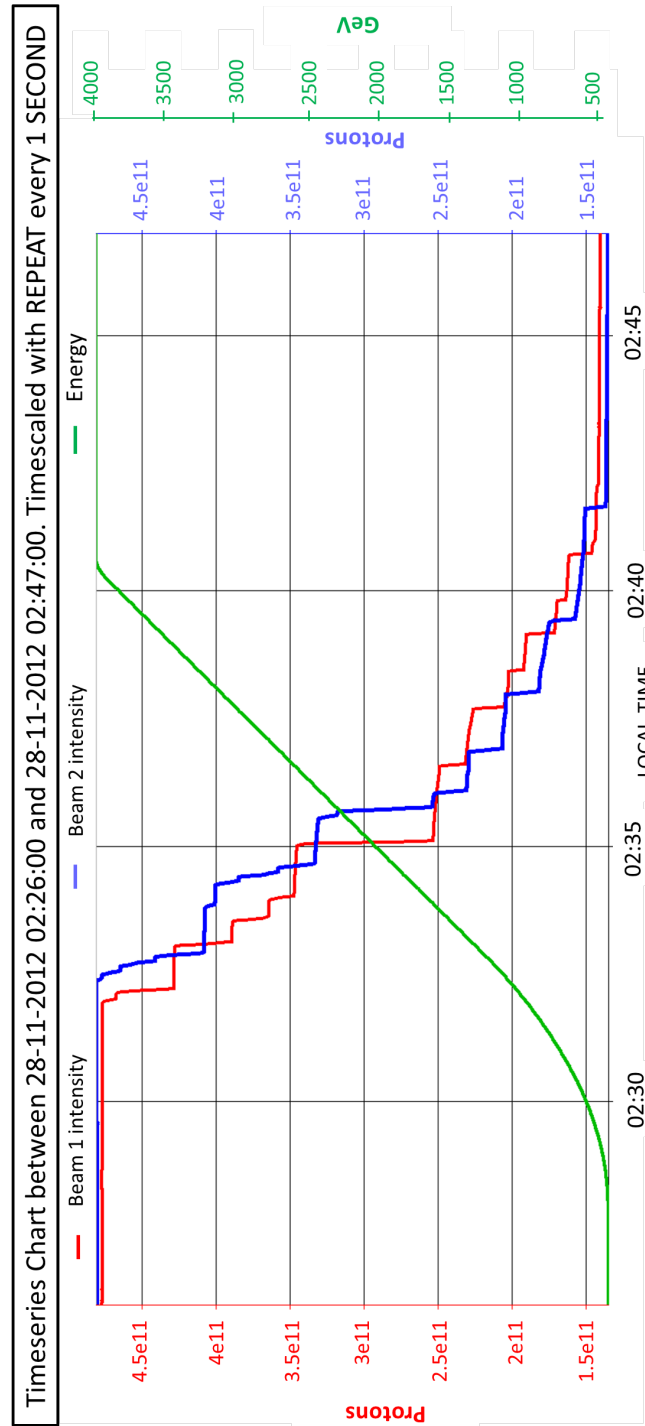


Figure 5.14: Beam intensity as function of time during the ADT excitations in the energy ramp. The red line reproduces the trend of the proton intensity for Beam 1, while the blue line refers to Beam 2. The green curve shows the energy increase during the ramp.

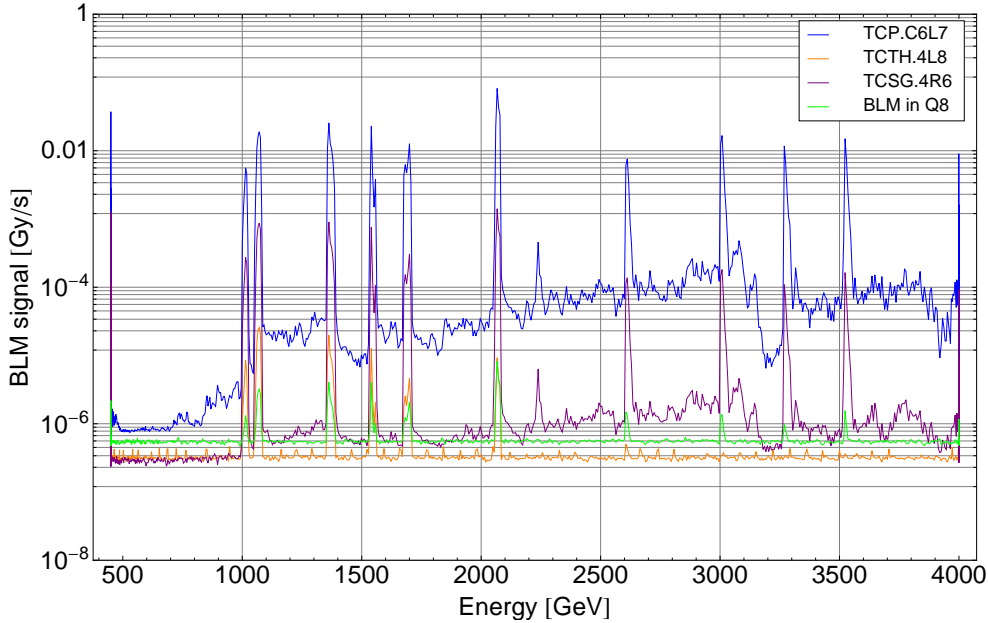
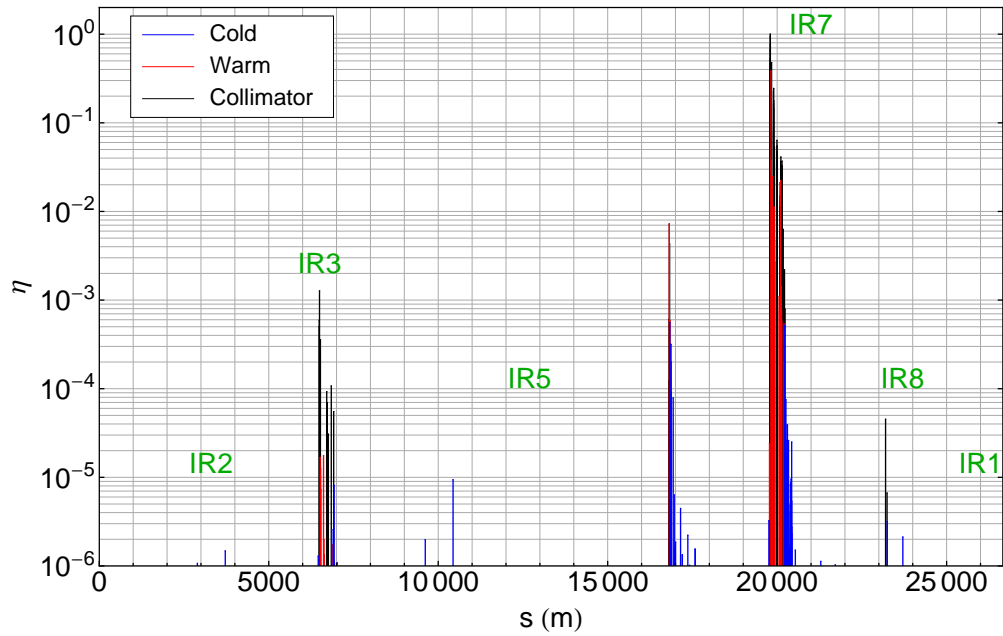


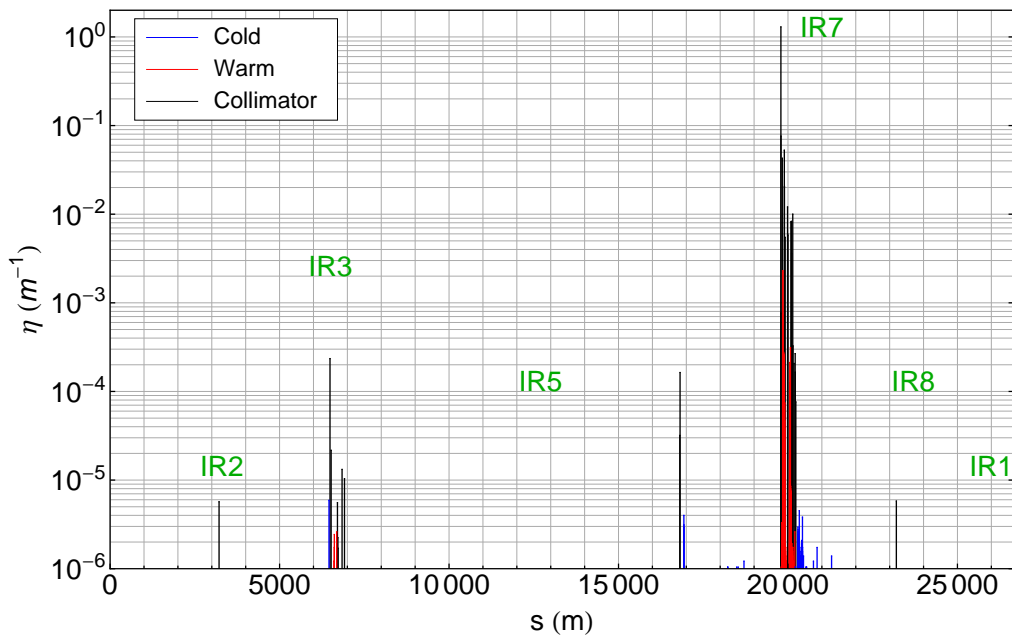
Figure 5.15: Signal from selected BLMs during the energy ramp for Beam 1. The highest peaks are recorded when an excitation by the ADT system occurs.

monitors in some selected locations in the ring during the energy ramp for Beam 1. In Fig. 5.16, instead, the measured loss map at 2 TeV is illustrated: loss levels are reached with approximately the same order of magnitude as in Fig. 5.2, but with a higher leakage to IR6 [38]. The loss maps for all the measured energies are in Appendix B.

The losses as a function of energy in simulation and measurement at selected locations are shown in Fig. 5.17. As already pointed out in the previous chapters, it should be noted that the measured signal coming out from the BLMs is related to the hadronic showers, produced by the protons interaction inside the collimator material. The response of the ionizing chamber cannot be directly compared with SixTrack output that, instead, refers only to the number of particles absorbed in the jaw. Therefore, in order to minimize the effect of the differences in BLM response, a normalization in Fig. 5.17 has been done: for each location the data from the simulations have been re-normalized to the first value of the related measurement. This assumes that the BLM response is independent of the energy, which is not strictly true. The simulations reproduce well the overall behaviour in the machine. The decaying trend in IR6 (purple) seems slightly overestimated by the simulations. The tertiary collimator in IR8 (orange), instead, shows a decreasing slope in agreement with its opening during the ramp.



(a) From BLMs data



(b) From SixTrack simulations

Figure 5.16: Comparison between loss map at 2 TeV from BLMs data taken in the LHC in November 2012 and SixTrack simulations.

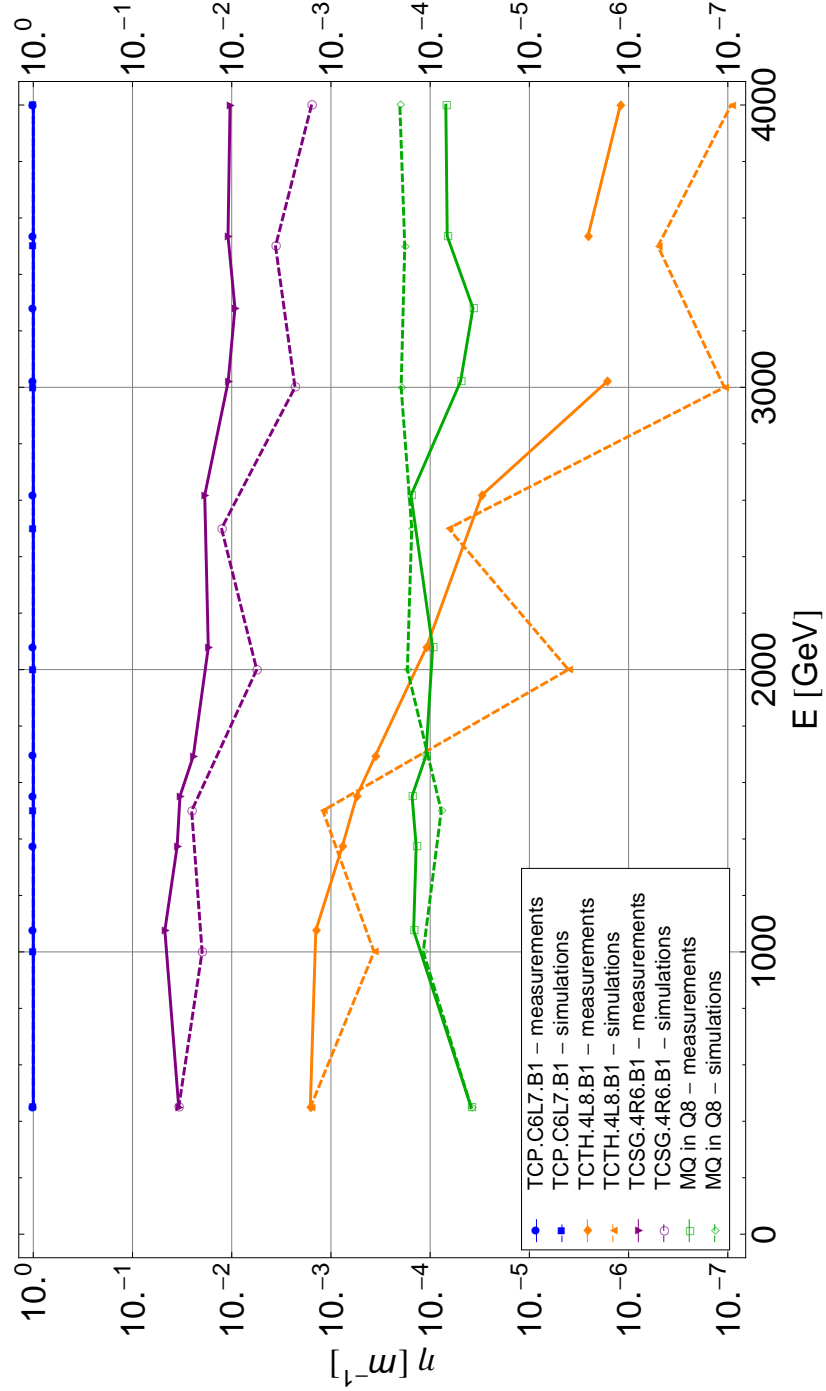


Figure 5.17: Cleaning inefficiency for selected collimators in the energy ramp: measurements and simulation compared. The continue lines refer to the measurements, while the dotted ones to the simulation results.

In the DS (green), the trend is almost constant: the worsening of the cleaning inefficiency due to the energy dependence of the scattering angles is well balanced by the tightening of the collimator. It must be pointed out that so far in all the plots where the cleaning inefficiency as function of energy has been shown,  $\eta_c$  has been calculated taking as  $n_{loss}$  the maximum number of particle lost in one single location around the ring, that sometime can also be outside the DS. In Fig. 5.17, the cleaning inefficiency for the TCTH is the result of an integration of particle losses over 17 m of length close to the placement of the BLM. This has been done, in analogy with Ref. [38], in order make the comparison as accurate as possible—the BLM sees not only one bin of 10 cm but instead the convoluted showers over a larger distance. The found discrepancies between measurements and simulations can be used as a guide to the simulation uncertainty when extrapolating the cleaning performance of the LHC collimation system also at higher energies for future configurations of the accelerator.

When accounting for the uncertainties in comparing the simulated number of locally lost particles with the measured BLM signals, a good correspondence between the measurement of the energy dependence of the cleaning inefficiency and SixTrack results could be established. These results, together with the possibility to estimate the simulation error with respect to the measurements, give an increased confidence in the ability of SixTrack to reproduce the collimation inefficiency as function of the proton energy. Therefore, SixTrack is now well benchmarked to extrapolate the cleaning performance of the LHC collimation system also at higher energies, useful for future configurations of the accelerator.

### 5.3 Looking towards 7 TeV scenario after LS1

An increase in luminosity and energy has been planned for the LHC after the next two years of shut down. The goal is to start operation at 6.5 TeV, with the possibility to increase the energy to the design value of 7 TeV in the future. Obviously this requires a careful prediction of the collimation performance in terms of cleaning inefficiency in this new scenario.

Several proposals for the new beam optics have been done together with the calculation of the collimator settings [43]. Two extreme cases can be identified. In the first option ("nominal" settings) the injection retractions are kept constant in  $\sigma$  in IR7: since the beam size decreases with the energy, consequently  $\sigma$  at 7 TeV is much smaller than at 450 GeV, it implies a smaller gap in mm between the beam and the collimator jaw. On the other hand, more "relaxed" settings can be used with the collimators farther way from the beam. For the details about the positions of the collimators in

Table 5.3: Comparison between collimator half-gaps at injection, 4 TeV (2012 settings) and 7 TeV (nominal and relaxed settings).

Location	Coll. type	Half-gap [ $\sigma$ ]			
		450 GeV	4 TeV 2012 sett.	7 TeV nominal	7 TeV relaxed
IR7	TCP	5.7	4.3	5.7	7.0
	TCSG	6.7	6.3	6.7	10.3
	TCLA	10.0	8.3	10.0	13.0
IR3	TCP	8.0	12.0	12.0	12.0
	TCSG	9.3	15.6	15.6	15.6
	TCLA	10.0	17.6	17.6	17.6
IR6	TCSG	7.0	7.1	7.5	11.1
	TCDQ	8.0	7.6	8.0	11.6
experiments	TCT	13	26	26	26

both configurations refer to Table 5.3.

The SixTrack code has been used to simulate the cleaning performance at different intermediate energies up to 7 TeV.  $6.4 \times 10^6$  and  $64 \times 10^6$  particles have been tracked for 200 turn respectively for the nominal and relaxed settings configurations. In order to calculate the collimator half-gaps at every energies, a linear interpolation between the openings at injection and flat top has been done, according to the values in Table 5.3.

Fig. 5.18 shows the highest local cleaning inefficiency around the ring,  $\eta_c$ , as function of the energy in both cases: the green line is related to the simulation up to 7 TeV nominal settings, while the red one refers to the case with the collimators in relaxed opening. As expected, the two trends are quite different: in the second case, in fact, the inefficiency increases with the energy much faster than the first case, because the relaxed settings keep the collimator jaws more opened with respect to the beam. The simulated efficiency seems in both case to be above early predictions of the equivalent quench limit  $\eta_q^c \approx 1.7 \times 10^{-5} m^{-1}$  predicted for the 7 TeV scenario (0.2 h beam lifetime and nominal intensity) in Ref. [11]: looking at Fig. 5.18 and also at the loss maps in Fig. 5.19, the difference is very small for the nominal case but with relaxed settings the value is 4 times above the threshold. However, it should be noted that this is the peak over a 10 cm bin. The choice to normalize the inefficiency over 10 cm is a conservative approach to leave some margin for possible uncertainties concerning the calculation of the quench limit. Furthermore, if instead the latest FLUKA energy deposition studies [44] in the cold magnets in the IR7 DS are taken into account, together with updated estimates on the power deposition that would quench

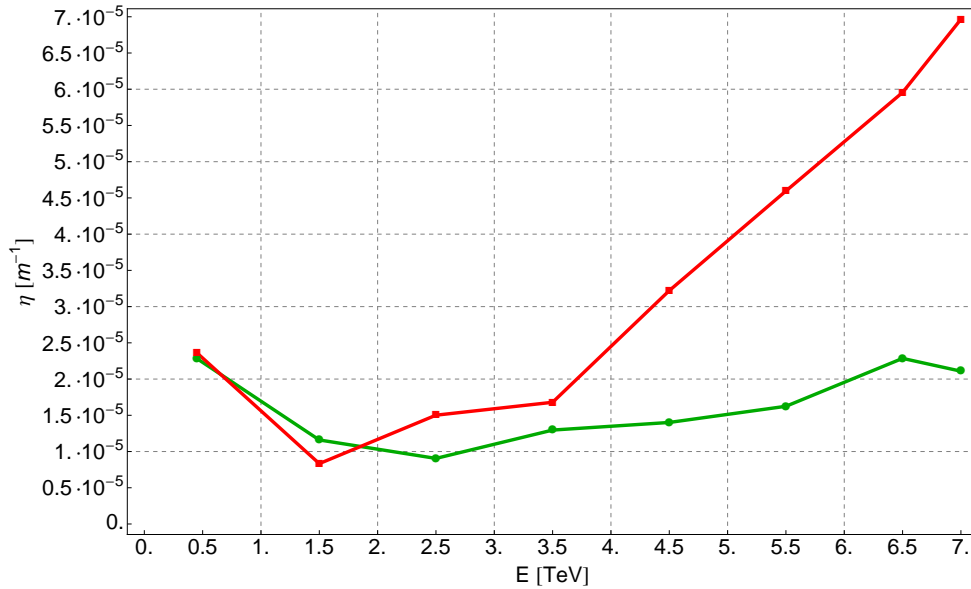
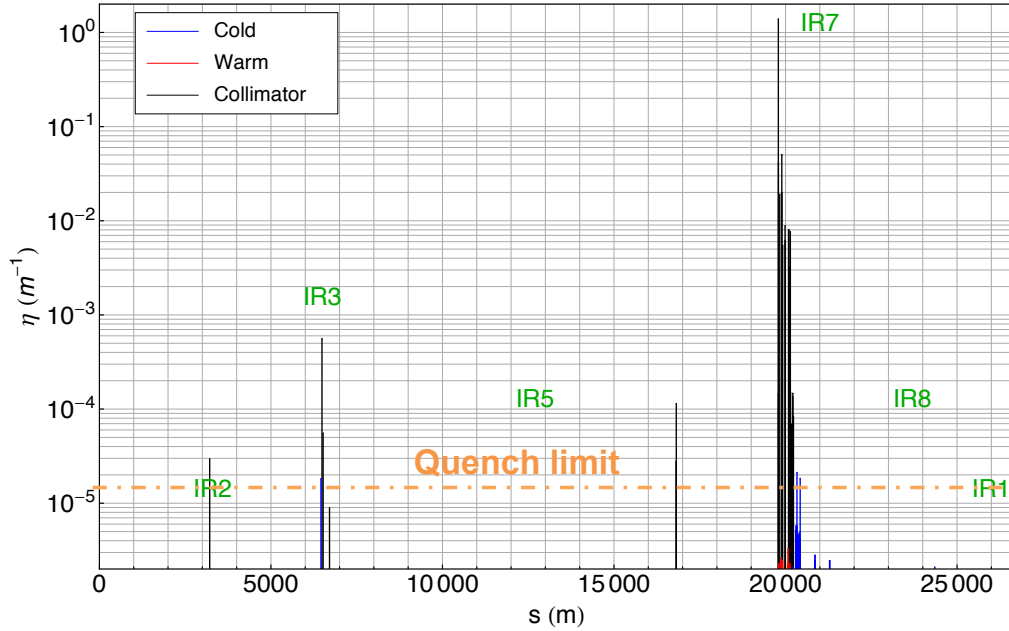


Figure 5.18: Cleaning inefficiency in the IR7 DS (Q8) as function of energy up to 7 TeV in two different scenarios: nominal (green) and relaxed settings (red). The quench limit line refers to the value predicted in Ref. [11].

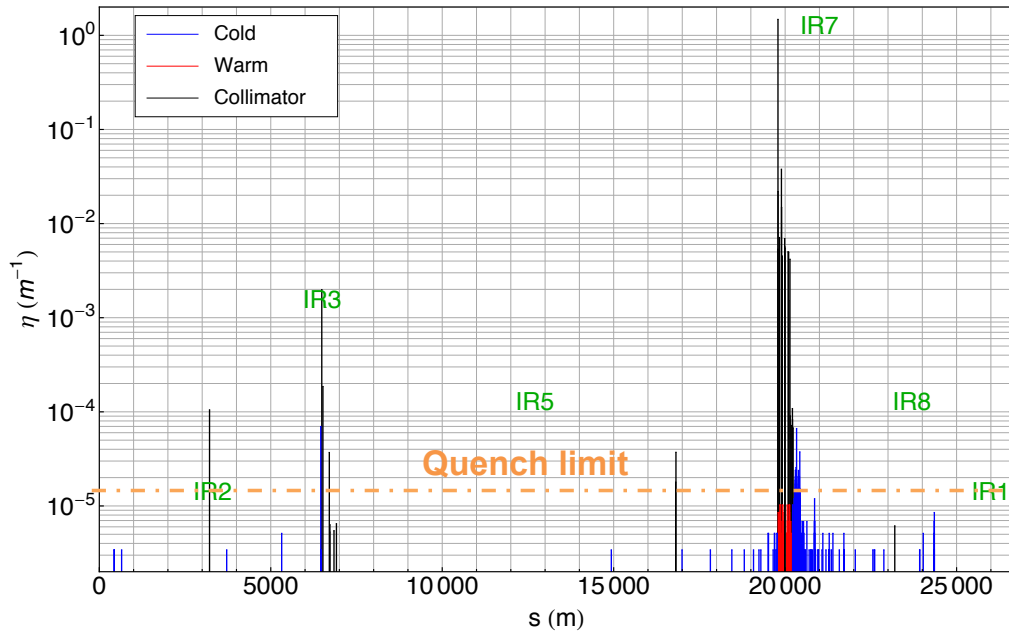
a magnet [45], the estimated heat load in the cold magnets of the DS with relaxed settings (considering a 0.2 h beam lifetime and nominal intensity) is about a factor 2 below the quench threshold. This is not a large margin considering all uncertainties. For nominal settings, the margin is significantly larger.

A comparison of the simulated inefficiency for some collimators in the two configurations just analysed is shown in Fig. 5.20, where the continuous lines are used for the simulations with nominal setting, while the dotted ones for the case of relaxed settings. Once again the inefficiency in the DS is calculated integrating the losses within a 17 m interval. In both cases an increasing trend of  $\eta_c$  is visible from injection to 7 TeV, but the larger openings of the collimators with the relaxed settings worsens the cleaning performance.

Clearly the nominal settings are more efficient in protecting the machine aperture from losses. Therefore, these settings should be the first choice unless other constraints are more important. For example, it might be necessary to open the collimators to relaxed settings in order to keep the impedance down so that the beam does not go unstable [43].



(a) 7 TeV nominal settings



(b) 7 TeV relaxed settings

Figure 5.19: Simulated beam loss maps for two possible 7 TeV scenarios. The quench limit shown refers to the value predicted in Ref. [11].

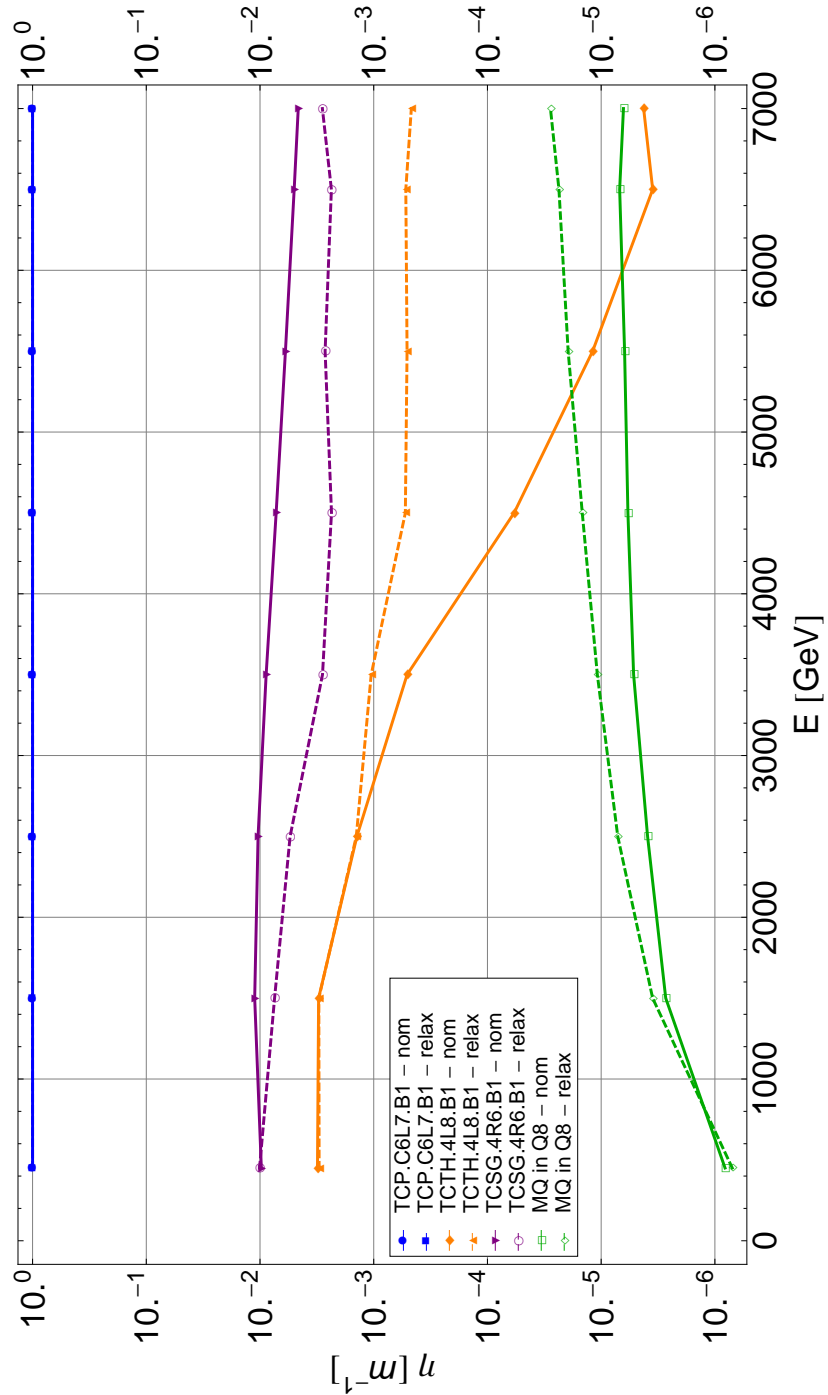


Figure 5.20: Comparison of the cleaning inefficiency for selected collimators in the energy ramp up to 7 TeV. The continue lines refer to the nominal 7 TeV settings, while the dotted ones to the relaxed 7 TeV configuration.

# 6

## Simulation of Off-Momentum Cleaning in IR3 Insertion

---

In the LHC, high-amplitude particles are cleaned by either betatron collimators or momentum collimators. Previously, losses of particles with large betatron oscillations have been studied more in detail [10, 11] since they are considered as a more likely performance limitation of the machine. During the first three years of the operation of the LHC, losses higher than expected have been measured in IR3 [46], which could induce radiation damage to warm magnets [47]. Therefore, the main aim of the study discussed in this chapter is to provide simulated loss maps in IR3. Several physical processes could drive particles onto the momentum collimators. One of them is studied and is the main focus of this chapter: the important contribution from particles that, for any reason, have left the RF bucket and slowly lose energy through synchrotron radiation losses until they hit the collimators. Once the loss distribution is obtained, it can be used for FLUKA [34, 35, 36] studies of energy deposition on the collimator jaws and warm magnets. The results of this study are an important ingredient in assessing the effectiveness of the installation of new passive absorbers to protect the warm magnets. A second but not less important goal is to determine the typical impact parameter distribution in IR3, which will aid in adapting the simulation to other machine scenarios. In the following, simulations are presented of off-momentum particles outside the RF system acceptance, which are driven into the IR3 collimators by radiation damping, in a 7 TeV nominal scenario..

### 6.1 Synchrotron motion in the LHC: basic check of longitudinal particle motion in SixTrack

As seen in Section 2.1.2, particles circulating in a storage ring have an energy that can deviate from the nominal value and thus have an energy offset  $\delta$  (Eq. 2.28). As a consequence of that, particles perform synchrotron oscillations around the nominal energy. Because of the ultra-relativistic energies in the LHC, the relativistic  $\beta \simeq 1$  and hence the momentum is  $p \approx E/c$ . We can therefore use either  $E$  or  $p$  in Eq. 2.28.

Mathematically, the equation of the particle motion in the longitudinal phase space is described by Eq. 2.35. In order to check if the simulation setup includes all the right parameters to reproduce the longitudinal phase motion of off-momentum particles, SixTrack simulations have been performed tracking 64 particles for 1500 turns. In Fig. 6.1 the trajectories corresponding to the analytical solutions of Eq. 2.35 and the simulated results have been plotted together to be compared. To allow a good representation, a

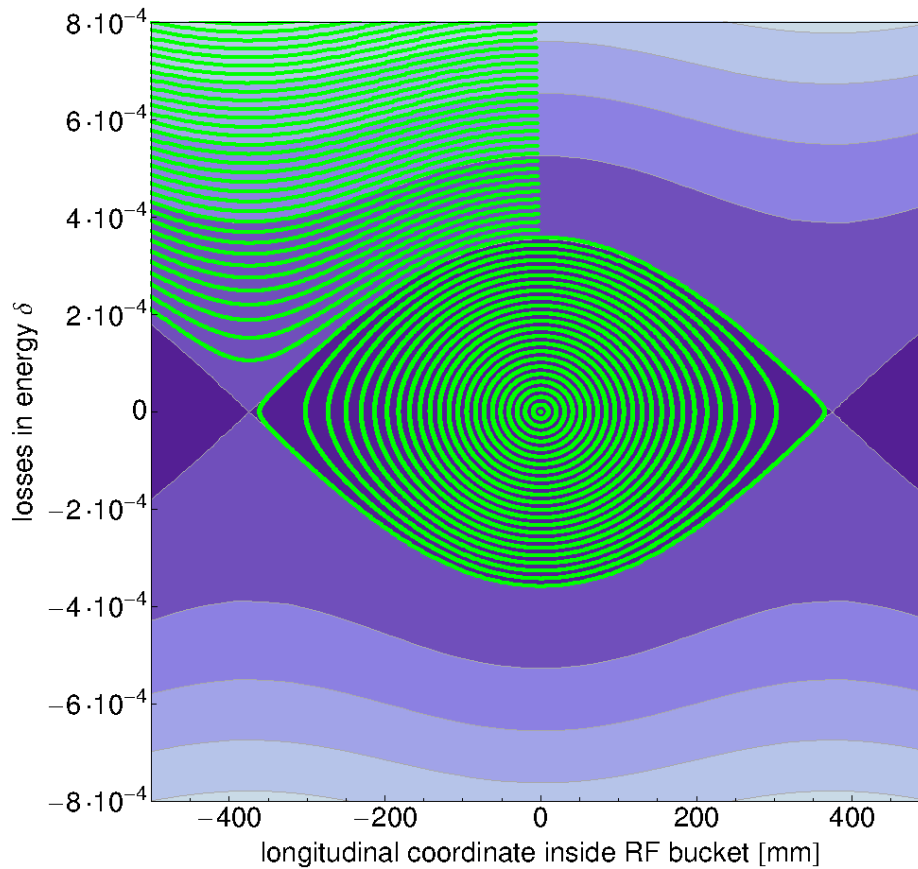


Figure 6.1: Longitudinal phase space motion from analytical formula (contour lines) and SixTrack simulations (in green), without radiation damping.

proper conversion of the variables of Eq. 2.35 in the phase space coordinates ( $\delta$  and longitudinal coordinate inside the RF-bucket  $s$ ) has been done. The contour lines of Fig. 6.1 represent the analytical solution of Eq. 2.35 for different (constant) values of the total energy of the system. Each green line, instead, refers to a particle starting with a slightly different energy offset around 7 TeV that has been tracked by the code, without taking into account the synchrotron radiation effect. Particles with a relatively small  $\delta$

perform a closed and stable trajectory inside the RF-bucket. When the initial energy offset is a value large enough to exceed the bucket acceptance, instead, the particles performs unbound motion. From Fig. 6.1 it can be stated that SixTrack results completely agree with Eq. 2.35.

## 6.2 Off-momentum simulation setup for 7 TeV scenario

To achieve the goals introduced at the beginning of this chapter, SixTrack simulations have been performed at 7 TeV by introducing a simple radiation damping routine inside the code: each tracked particle loses a small amount of energy on every turn due to the emission of synchrotron radiation. Eventually, the energy offset becomes large enough to drive the particles onto the IR3 primary collimator.

The radiated energy through synchrotron radiation is proportional to the fourth power of the relativistic gamma  $\gamma_{rel}$  and is inversely proportional to the square of the radius of the path travelled by the particles [7]. At nominal 7 TeV LHC operation, the energy loss per turn due to synchrotron radiation is 6.71 keV per turn [1]. Since the simulations involve off-momentum particles, an energy loss  $\Delta E_s$  is applied every turn to each particle given by: :

$$\Delta E_s = 6.71 \text{ keV} \cdot \frac{\gamma^4}{\gamma_0^4}. \quad (6.1)$$

Particle starting conditions are randomly generated using a Mathematica script. Betatron coordinates are sampled from a  $3\sigma$  Gaussian distribution; in the longitudinal phase space, instead, since the real distribution of  $\delta$  is not well known, a uniform distribution starting from the RF-bucket limit to 20% outside has been assumed to sample the energy offset values, as shown in Fig. 6.2. This is compatible with the assumptions made in Ref. [48]. The longitudinal coordinate inside the RF-bucket  $s$  is set to 0, since the synchrotron motion anyway makes all particles pass all phases. The script writes all the coordinates in an external file that has to be read by SixTrack in input. To allow that, the first number of line (3) in the *fort.3* input file (see Section 4.1.2) must be set to 4 [30]. For the purpose of this study, the simulation has so far been run only for Beam 1. The main settings of SixTrack simulations are shown in Table 6.1. For the collimators, nominal 7 TeV half-gaps have been used, where the most important ones are shown in Table 6.1. For more details see Table 5.3.

It should be noted that the performed simulations are extremely lengthy and demanding in terms of computing time: due to the very small energy loss on every turn and the phase space conditions chosen as input for the

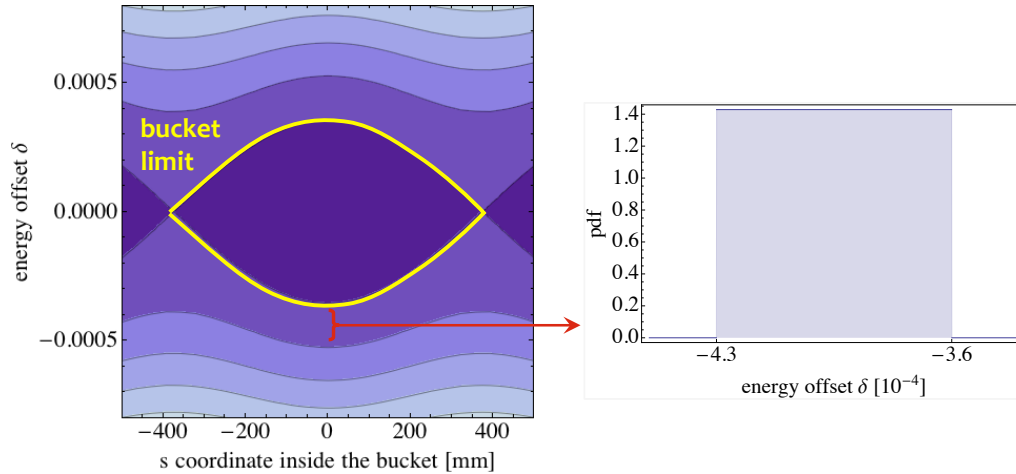


Figure 6.2: Uniform distribution assumed for the initial energy offset  $\delta$ . In the x-axis is shown the interval within  $\delta$  is sample, while in the y-axis the related probability distribution function (pdf).

Table 6.1: Main parameters used for SixTrack simulation.

SixTrack Parameter		Input
Number of particles	[protons]	$1.25 \times 10^5$
Energy	[TeV]	7
Number of turns	[turns]	$> 1.3 \times 10^6$
RF voltage	[MV]	16
RF frequency	[MHz]	400.8
Synchrotron angular frequency	[ $rad/s^{-1}$ ]	144.5
RF-bucket limit (at s=0)		$0.36 \cdot 10^{-3}$
IR3 TCP setting	[ $\sigma$ ]	12
IR3 TCSG setting	[ $\sigma$ ]	15.6
IR3 TCLA setting	[ $\sigma$ ]	17.6
IR7 TCP setting	[ $\sigma$ ]	6
IR7 TCSG setting	[ $\sigma$ ]	7
IR7 TCLA setting	[ $\sigma$ ]	10

simulations, more than  $10^6$  turns are needed for particles to propagate from the RF bucket to the momentum cut of the IR3 TCPs (see Fig. 6.4). Actually, about 4 computing days are needed to terminate a single 64 particles simulation. Moreover, although only  $1.25 \times 10^5$  particles have been tracked by the code, using several parallel simulations on a cluster, it is sufficient to have good statistics for the hits on collimators, but insufficient to resolve the small losses in the cold regions.

In the perspective of additional future studies concerning off-momentum particles in the LHC a significant improvement would be to find a way to make the simulations faster but with equivalent results. Ways to speed up the simulation and obtain higher statistics are discussed in Section 6.4.

## 6.3 Main results

### 6.3.1 Particle loss distribution in the ring

The distribution of the simulated losses around the ring on collimators, as simulated by SixTrack, is shown in Fig. 6.3 together with a zoom in IR3 cleaning insertion. As expected, the highest losses are observed in the off-momentum cleaning but significant peaks appear also in IR7.

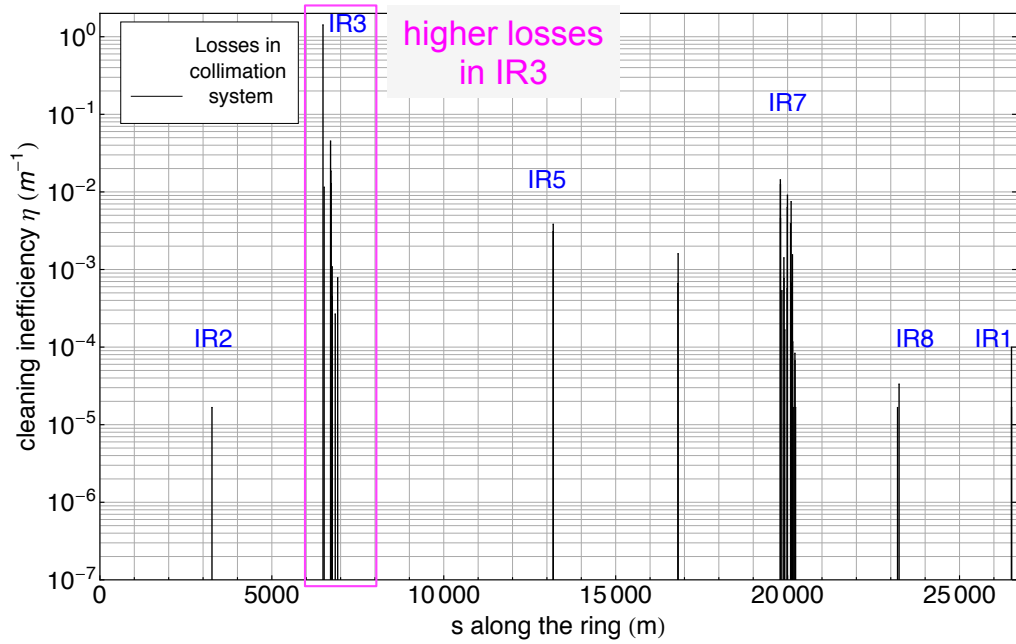
From these simulations no losses on the cold and warm magnets are observed: the reason is still not completely understood but maybe the statistics of  $1.25 \times 10^5$  particles used for the simulations give an insufficient resolution of losses in the aperture. However, the total fraction of simulated particles reaching the aperture is generally of the order of  $10^{-3}$ : in the 4 TeV case discussed in Section 5.1.1, for example, the global inefficiency  $\eta_g$  (Eq. 2.44), which refers only to the particles lost in the aperture, is about  $4.2 \times 10^{-4}$ . Multiplying this value by the number of particles tracked in the case in analysis in this chapter, instead, we find that a bit more than 50 particles are lost in the aperture at 4 TeV.

So, the losses in the aperture can be considered as a negligible correction to the results on the collimators shown Fig. 6.3, which therefore can be trusted.

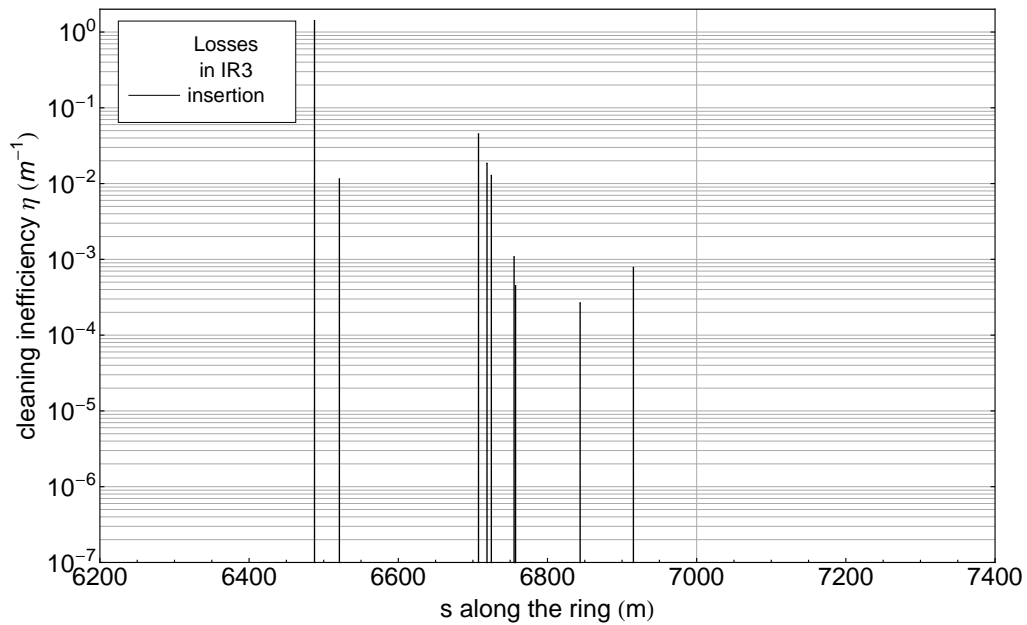
### 6.3.2 Particles distribution in the IR3 TCP jaw

From the analysis of the *FirstImpacts.dat* files, all the tracked particles hit first the primary collimator in IR3. Since particles are losing energy through synchrotron radiation, only one TCP jaw has been hit. The following figures summarize the simulated results concerning the IR3 TCP. The distribution of the turn of the hit (Fig. 6.4) shows that about  $9 \times 10^5$  turns are needed before a particle hits the TCP jaw driven by radiation damping at this energy and RF configuration. In Fig. 6.6 the particle impact distribution along the collimator length is illustrated. The average impact parameter  $b$ , instead, is about  $2 \mu\text{m}$  (Fig. 6.6). The average impact angle on the collimator jaw (Fig. 6.7),  $-0.0439 \text{ mrad}$ , is in perfect agreement with the value calculated from Eq. 2.40 (see Table 6.2).

The resulting spatial distribution of inelastic interactions in the IR3 primary collimator is shown in Fig. 6.8. Most particles are absorbed in the



(a) Full ring.



(b) Off-momentum cleaning insertion IR3.

Figure 6.3: Beam loss map from SixTrack simulations at 7 TeV with synchrotron radiation effect.

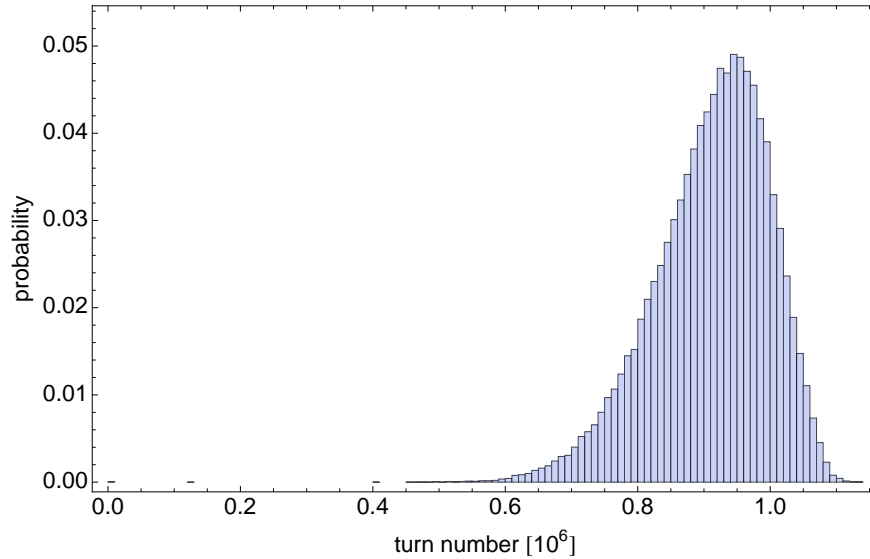


Figure 6.4: Distribution of the turn when the first hit at IR3 TCP occurs.

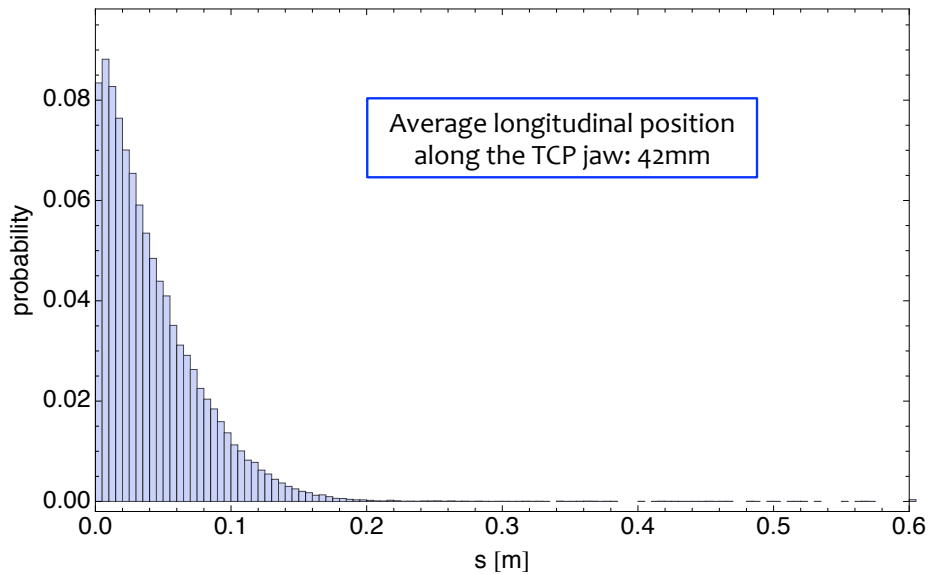


Figure 6.5: Distribution of the longitudinal position along IR3 TCP jaw where the first impact occurs.

first hundred micrometers of transverse depth, mainly concentrated in the first half length of the jaw, and the number decreases going deeper in the material. However, some blue spots, representing one single particle, are seen up to 1.5 mm depth. All the coordinates of first hit and absorption for each particle in the IR3 primary collimators are now available: they can be used as input for further FLUKA dose studies in the collimator material

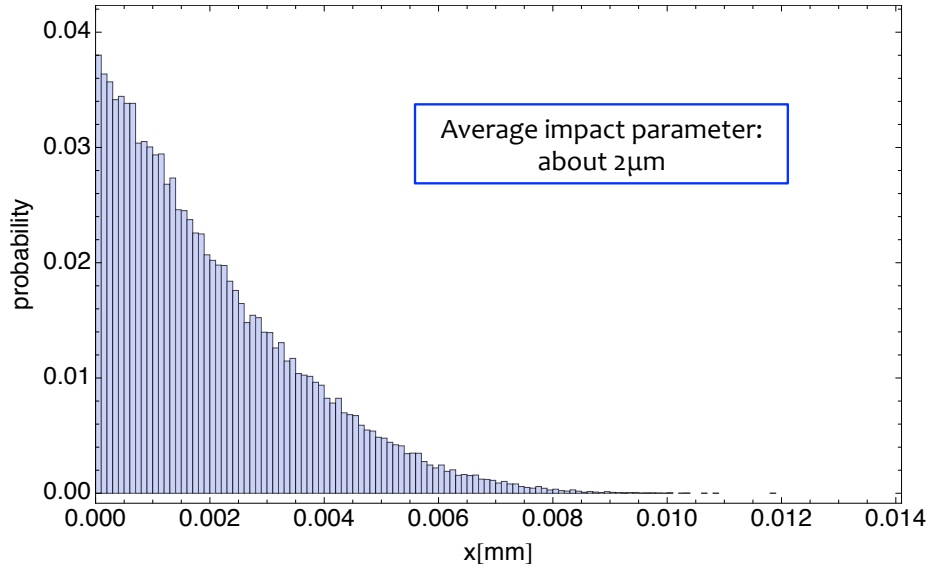


Figure 6.6: Distribution of the impact parameter in IR3 TCP jaw.

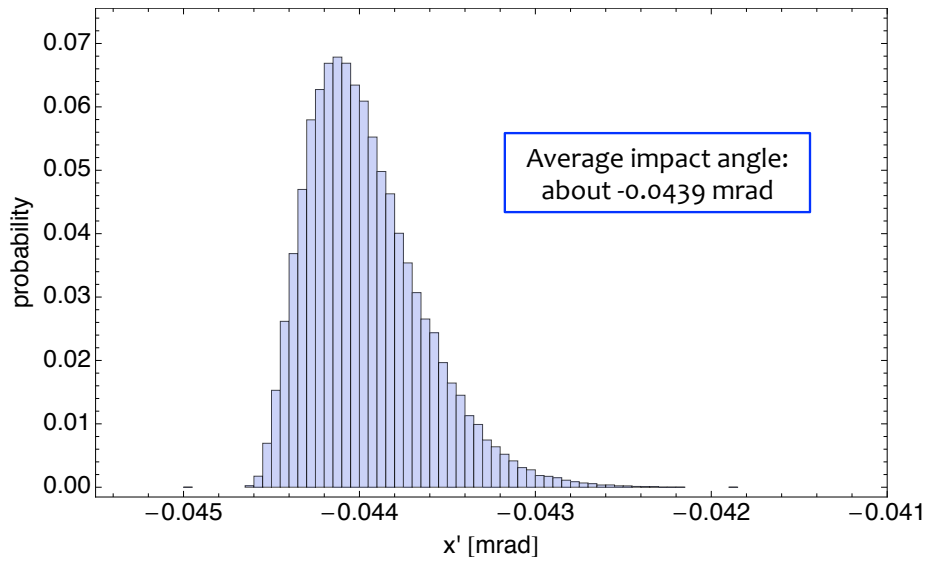


Figure 6.7: Distribution of the impact angle in IR3 TCP jaw.

and the warm magnets. This is, at the time of writing, an ongoing study in the EN/STI group at CERN.

### 6.3.3 Choice of the initial $\delta$ distribution

One relevant aspect to discuss is the choice of the initial energy offset  $\delta$ .

To justify the assumptions done in Section 6.2, the results of the sim-

Table 6.2: Impact angle at TCP.6L3.B1 at 7 TeV.

TCP.6L3.B1		
Parameter	Unit	Value
Jaw x-coordinate	[mm]	2.9808
Dispersion function	[m]	2.28
$\delta$		0.0013
Dispersion function derivative	[rad]	-0.034
<b>impact angle</b>	<b>[mrad]</b>	<b>-0.0444</b>

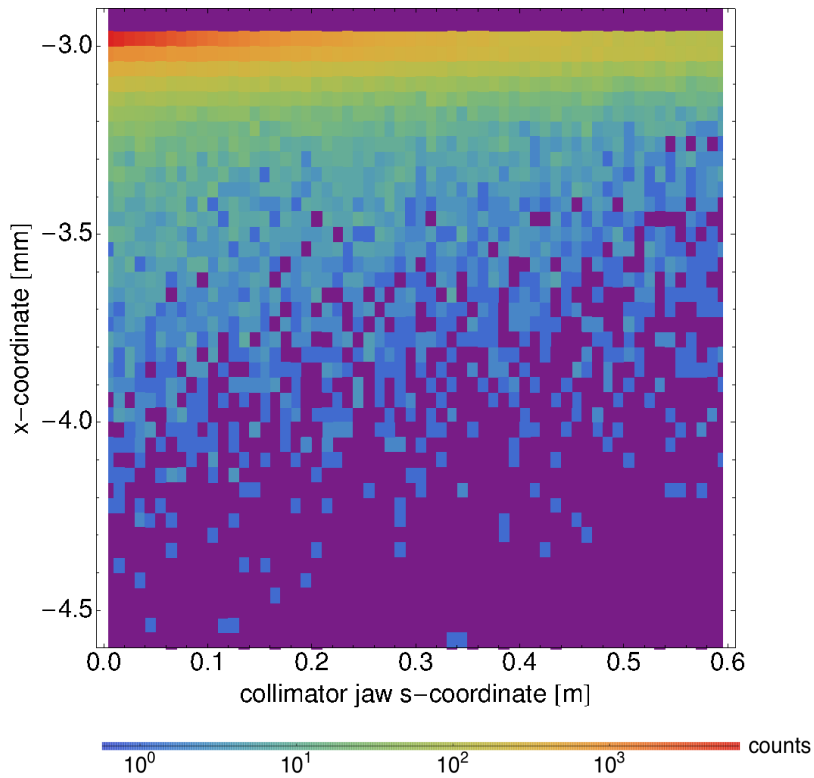


Figure 6.8: Density plot of coordinates of particle inelastic interactions as function of longitudinal coordinate in IR3 TCP right jaw.

ulations have been used to study the correlation between the initial  $\delta$  and the impact coordinates on the IR3 TCP. As shown in Fig. 6.9 and 6.10, no clear correlation can be identified: due to  $\delta$ , the particles will reach the collimator at different time but it does not influence their distribution inside the jaw. Therefore, the choice of a uniform initial distribution in  $\delta$  does not affect the final result in terms of particle impact distribution.

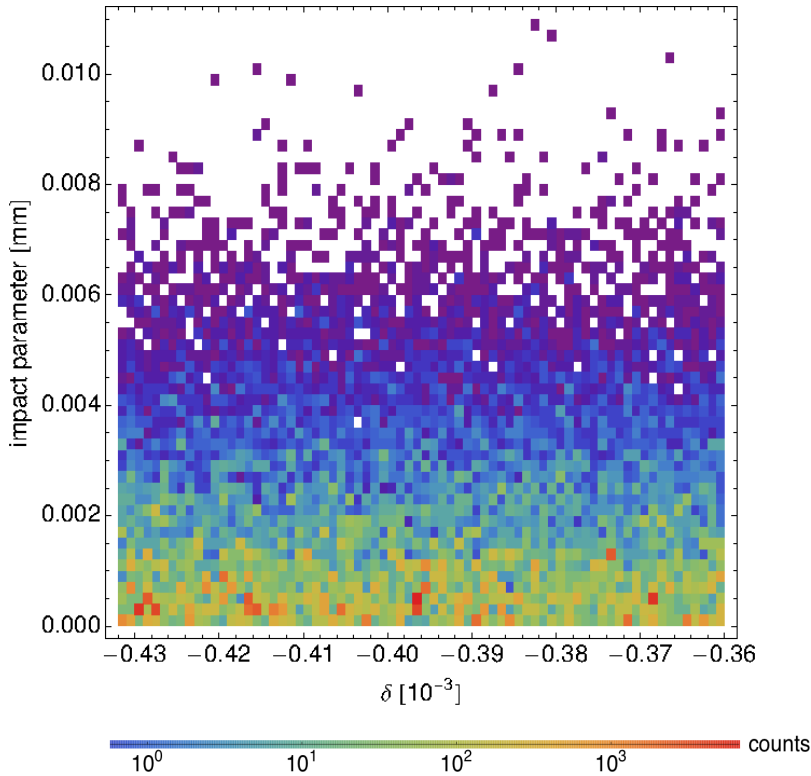


Figure 6.9: Correlation between the initial energy offset  $\delta$  and the impact parameter  $b$  at IR3 TCP.

## 6.4 Further studies

So far, particles have been tracked by SixTrack taking into account an energy loss per turn of 6.71 keV per turn, then scaled with the forth power of the energy of the particle itself. The amount of energy lost turn by turn is quite small and the particle has to travel many turn around the ring before hitting the jaw of the primary collimator in the momentum insertion.

Several possible ways of speeding up the simulation can be envisaged. One of them is to modify the SixTrack radiation damping routine in order to apply a larger (unphysical) energy loss per turn to a particle far from the jaws of the IR3 TCP, and once it is close, apply the realistic small energy loss. In order to have the particle driven into the collimator by the radiation damping in the same way as in the longer simulation, we want it to perform at least two synchrotron oscillations with the realistic energy loss before reaching the jaw, which may happen in an interval of  $10^{-4}$  m. Thus, as long as the distance between the particle and the TCP jaw is greater than  $10^{-4}$  m, a large energy loss (of 6.71 Mev per turn) is applied, and once the distance is smaller than  $10^{-4}$  m, the code switches to the realistic small loss.

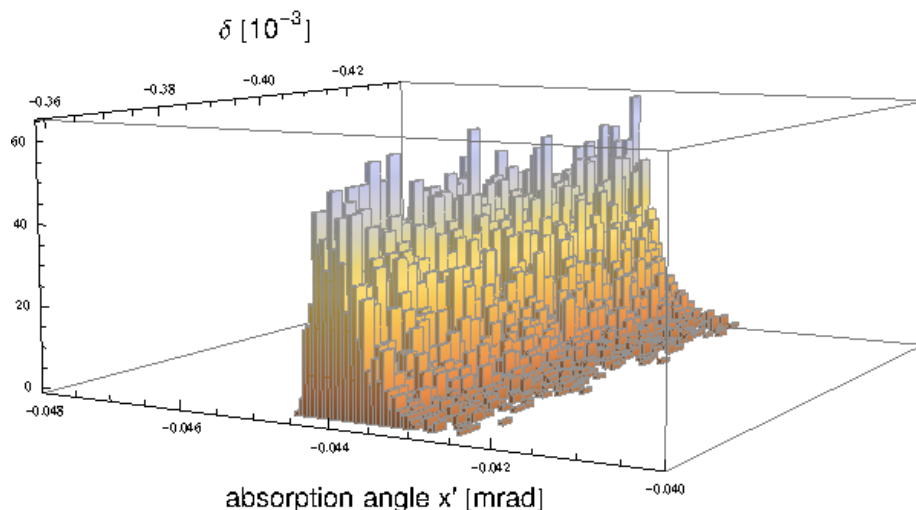


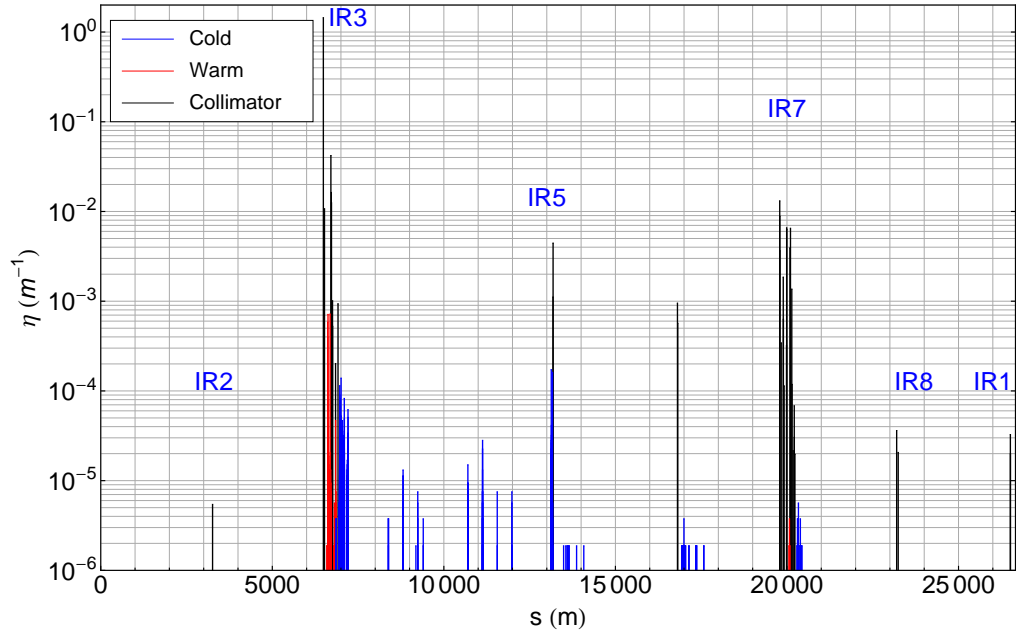
Figure 6.10: Correlation between the initial energy offset  $\delta$  and the impact angle at IR3 TCP.

As a consequence of that, much fewer turns are needed to hit the primary collimator in IR3, which decreases the needed computing time and allows for increased statistics.

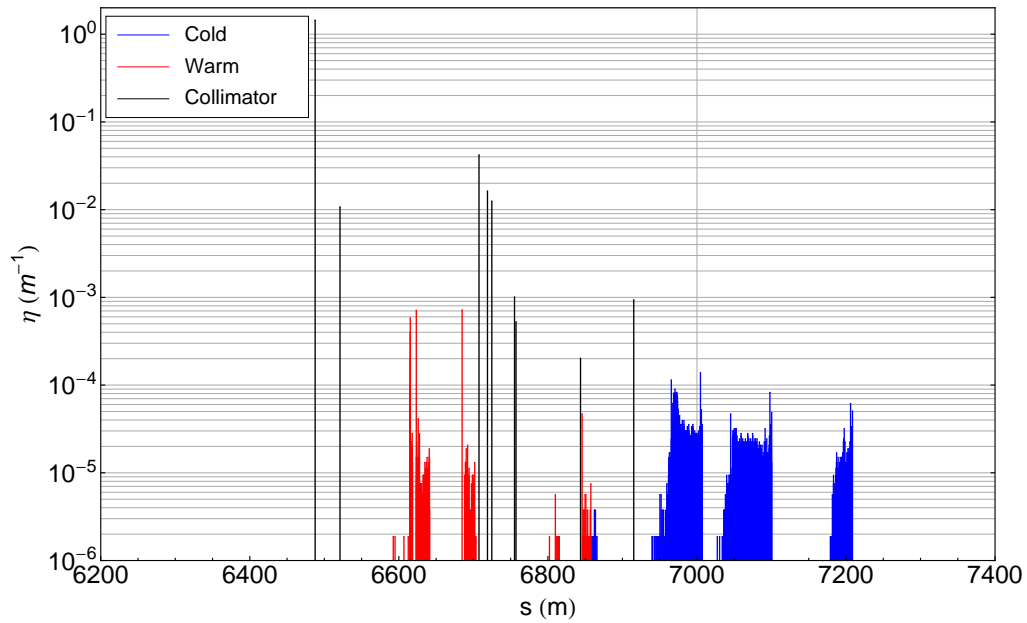
With the modified code, a new set of simulations has been performed:  $9.5 \times 10^6$  protons (more than one order of magnitude respect to the previous simulations have been tracked for 5000 turns. The energy, RF parameters and collimator settings are the same as the ones listed in Table 5.3 and the initial energy off-set for each particle is sampled from the same distribution used in the previous simulations.

Looking at the new simulated loss map along the ring and the zoom in the momentum cleaning insertion (Fig. 6.11) and comparing it with Fig. 6.3, it is easy to see that the losses on collimators occur in the same locations and with the same magnitudes. It means that a very good agreement can be established between the "old-slow" and the "new-fast" simulations in terms of loss distribution. The new distribution of the turn on which the particles reach the TCP for the first time is shown Fig. 6.12. Now only about 1000 turns or a little more are needed, which is an improvement in terms of computing time of about three orders of magnitude.

On the other hand, the results for the impact distribution at the IR3 TCP show some differences with respect to the longer simulation: From Fig. 6.6 and Fig. 6.14 it is evident that, in the fast simulation, particles hit deeper in the TCP jaw (average impact parameter of  $8.5 \mu\text{m}$ ) and from Fig. 6.13 that particles hit closer to the end of the jaw (the average longitudinal coordinate along the jaw length is now 12.6 cm). The average impact



(a) Full ring.



(b) Off-momentum cleaning insertion IR3.

Figure 6.11: Beam loss map from SixTrack simulations at 7 TeV with synchrotron radiation effect (faster simulations). Statistics:  $9.5 \times 10^6$  particles.

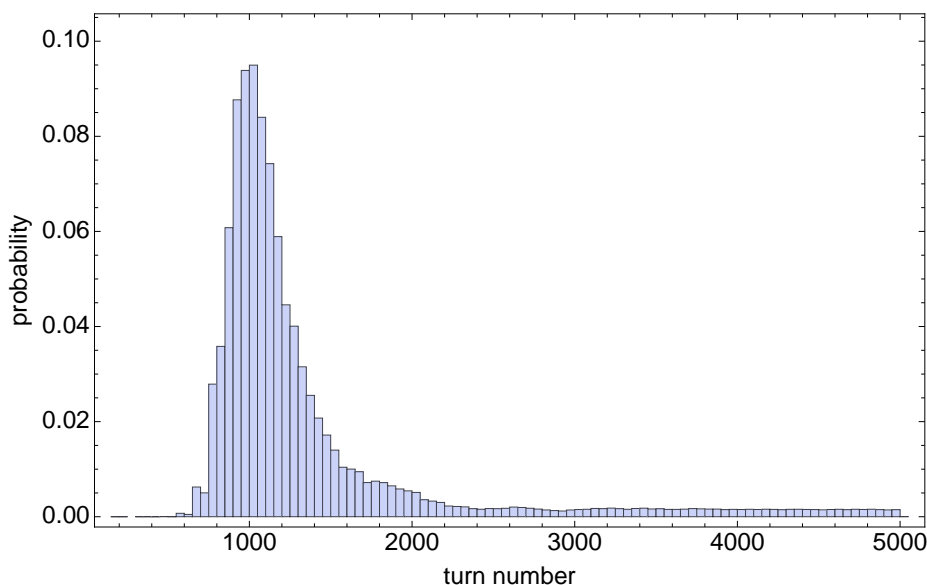


Figure 6.12: Distribution of the turn when the first hit at IR3 TCP occurs (faster simulations).

angle, instead, is not changed and stays around  $-0.044$  mrad, as illustrated in Fig. 6.15. Differences appear also in the  $x - s$ -distribution of inelastic interactions (Fig. 6.16): comparing this figure with Fig. 6.8, it is clear that the particles now penetrate so deep in the material that a not negligible amount of inelastic interactions can take place at more than 1 cm depth.

As in the previous simulation, no relevant correlation has been found between the initial  $\delta$  and the final impact distribution of the particles, as shown in Fig. 6.17 and Fig. 6.18. It is possible to conclude, hence, that the new and faster simulations of off-momentum particles reproduce well the distribution of the losses along the ring obtained in Section 6.3.1, saving also a large amount of computing time. However, the new results show some differences from the "old-slow" simulation in terms of particle impact distribution at the primary collimator in IR3. A possible improvement to the faster simulations could be to increase the distance from the TCP jaw at which the code switches to the small energy loss, but of course at the price of CPU time. Actually, a likely cause of the discrepancy found in the impact distribution is that with the non-linear dynamics at high amplitudes, some particles do not manage to performed the two synchrotron oscillations in spite of the  $100 \mu\text{m}$  distance.

Alternative methods for achieving higher statistics could be to use the output of the longer simulation as a starting point for a second simulation. Particle coordinates can be sampled with high statistics directly from the distributions in Fig. 6.6 and Fig. 6.5 and the simulation can then start

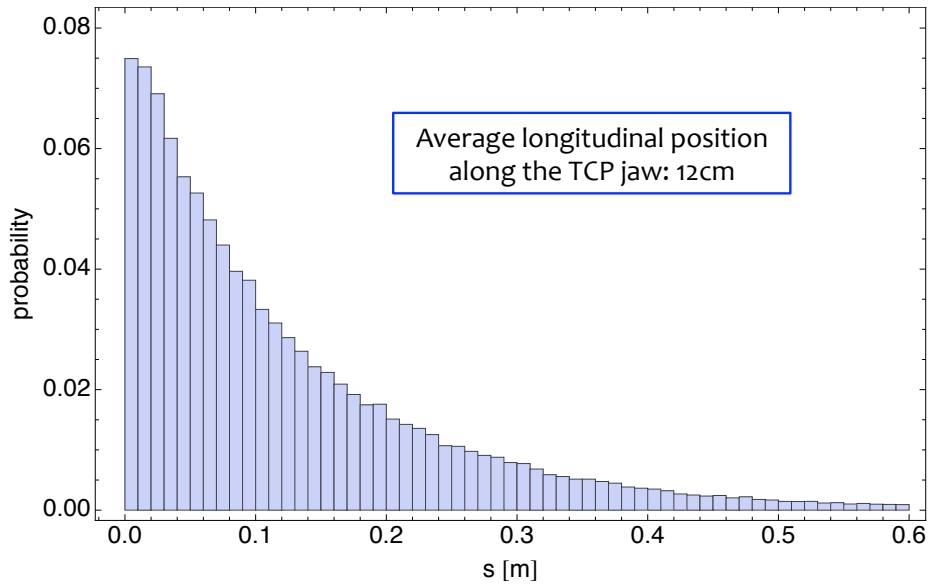


Figure 6.13: Distribution of the longitudinal position along IR3 TCP jaw where the first impact occurs (faster simulations).

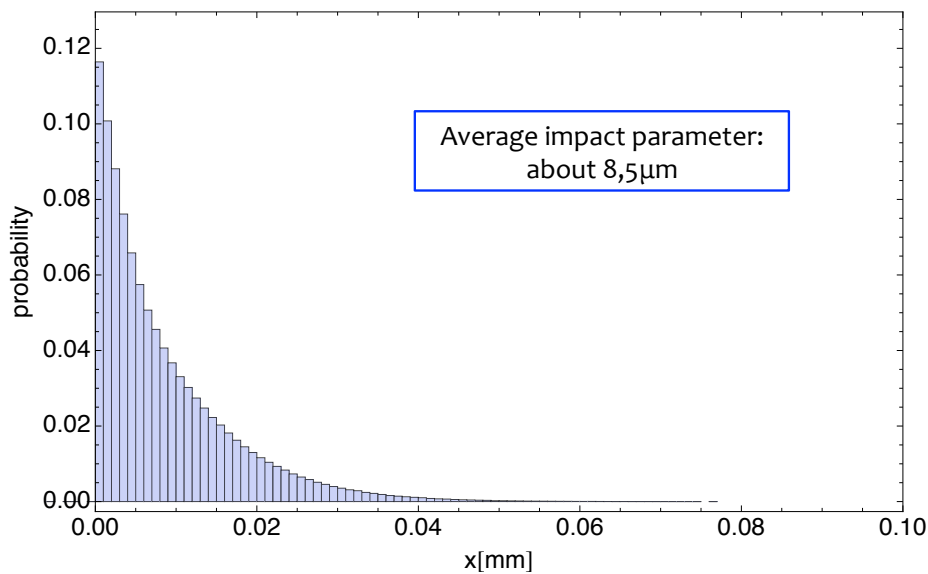


Figure 6.14: Distribution of the impact parameter in IR3 TCP jaw (faster simulations).

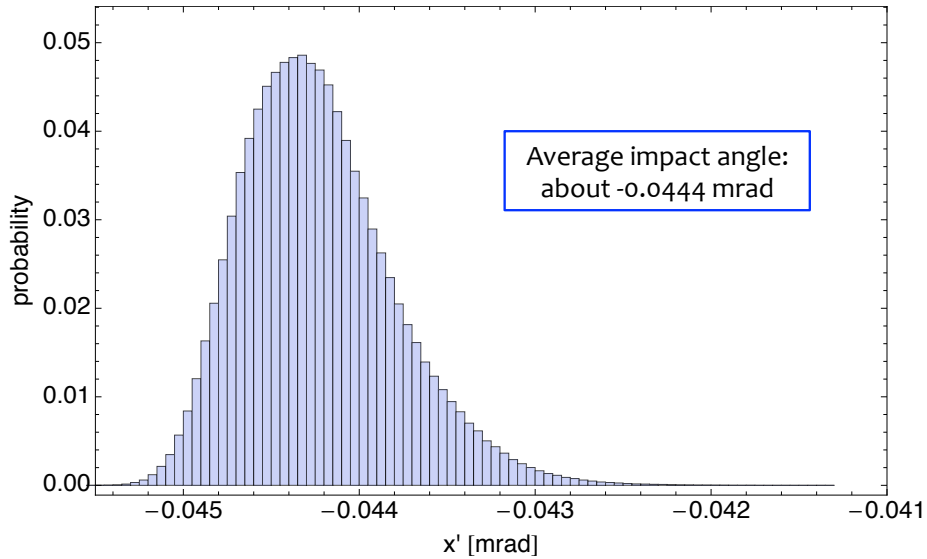


Figure 6.15: Distribution of the impact angle in IR3 TCP jaw (faster simulations).

directly at the IR3 TCP. Another method could be to analytically sample a starting distribution around the cuts of the IR3 TCPs in the synchrotron phase space, given an assumption on the impact parameters which could be deduced from the long simulation. This approach could make the simulations significantly faster but leading eventually to identical outcomes. These studies are left as future work.

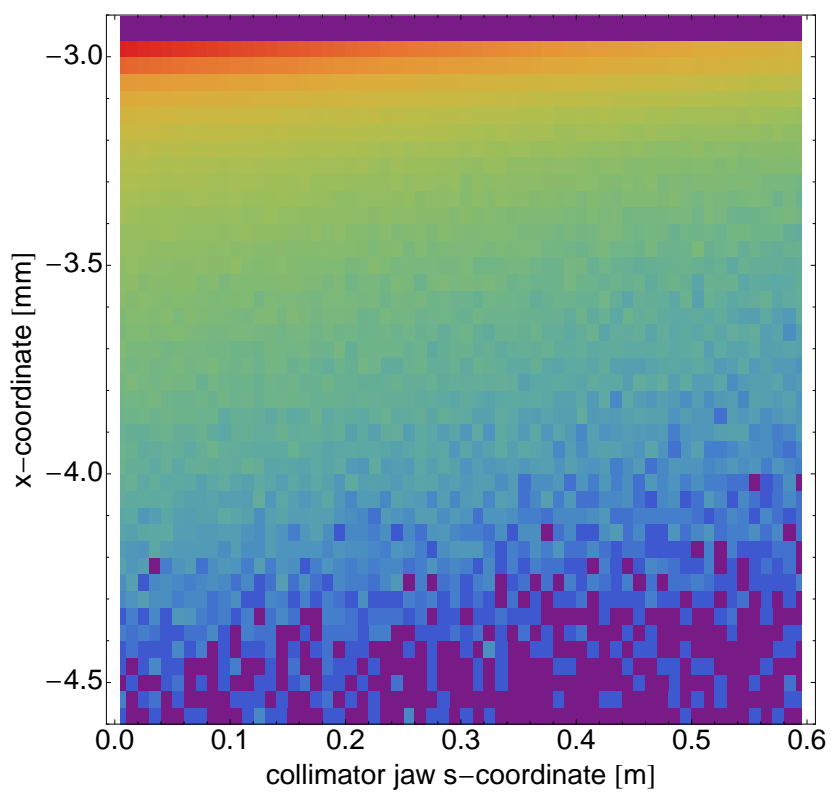


Figure 6.16: Density plot of particle impact parameter as function of longitudinal coordinate in IR3 TCP right jaw (faster simulations).

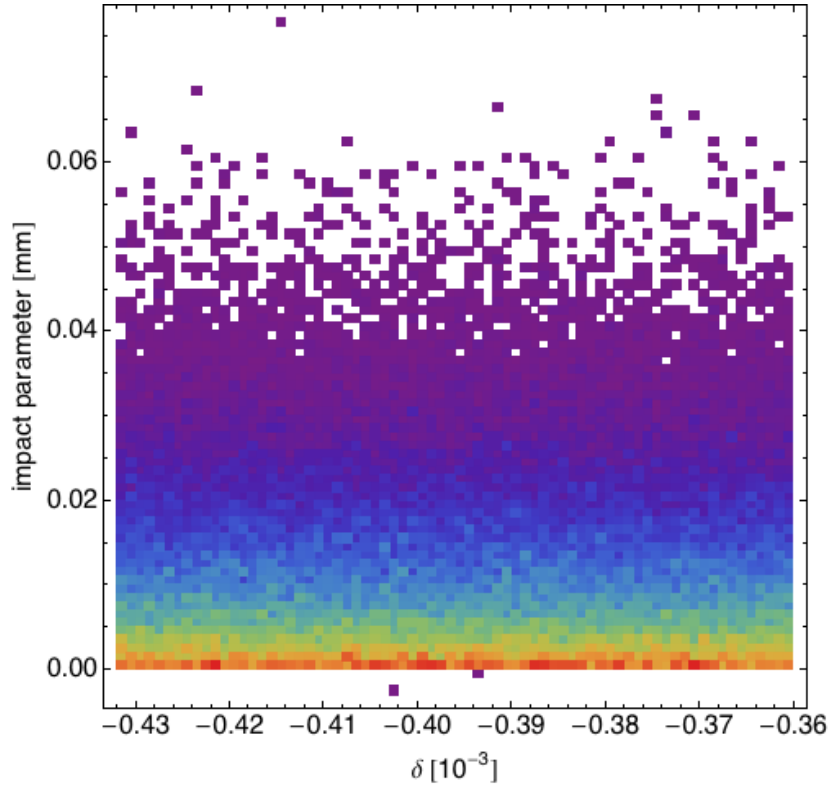


Figure 6.17: Correlation between the initial energy offset  $\delta$  and the impact parameter  $b$  at IR3 TCP (faster simulations).

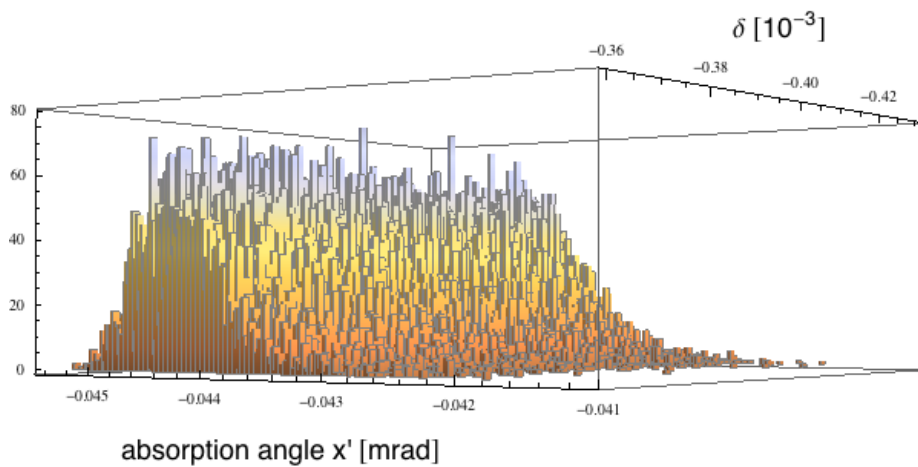


Figure 6.18: Correlation between the initial energy offset  $\delta$  and the impact angle at IR3 TCP (faster simulations).



# Conclusions

---

The Large Hadron Collider (LHC) at CERN is the largest particle accelerator ever built in the world and represents a large-scale, worldwide scientific cooperation project. It is a ring designed to accelerate two counterrotating beams and put them in collision inside experimental detectors.

According to the design parameters, the LHC has been built to handle an energy up to 360 MJ. This energy must be always monitored and kept under control: a deposition of about  $5 \text{ mJ s}^{-1} \text{ cm}^{-3}$  due to beam loss is already enough to quench one of the superconducting magnets located all around the ring.

A sophisticated system of collimators is thus installed in selected locations in the accelerator to intercept and absorb unavoidable particle losses. A collimation system with high cleaning performance is an essential requirement to guarantee a smooth and safe operation of the machine. Because of that, during the commissioning and the first years of the operation of the LHC, the cleaning inefficiency of the collimation system has been extensively studied with the main purpose to limit the number of particles escaping from this system. This master thesis aims to study the cleaning inefficiency of the LHC collimation system in different scenarios.

The design energy (7 TeV for each beam) has not been achieved yet: in March 2013, the maximum achieved energy of the LHC was 4 TeV. One of the goals to reach at the restart of the machine after the next two years of shutdown is to eventually increase the energy and the number of particles circulating in the ring up to the nominal values. As the energy per lost particle increases, and the margin to the quench limit decreases, the demands on the collimation system will be higher than in the previous run. Therefore, the prediction of the cleaning inefficiency at higher energies is the focus of the first part of this thesis. In the past, in fact, several studies have been done about the collimation performance, focusing on the beam injection energy and on the energy reached after the acceleration process. In this thesis, instead, the collimation performance at intermediate energies has been investigated through measurements and simulations with the Six-Track code. Different scenarios at intermediate energies (between 450 GeV and 4 TeV) have been simulated: the study of the separate influence of the the beam energy and the collimator settings has shown that the two effects counter-act in terms of the cleaning inefficiency of the system. The uncer-

tainty coming from the impact parameters is of the order of 20%. Then, the simulation results have been compared with measurements of beam losses taken in the LHC in November 2012: in spite of the uncertainties from comparing the simulated number of locally lost particles with the signals from ionization chambers around the machine, a qualitatively good agreement between simulations and experimental data was found. The increased confidence in SixTrack to reproduce the cleaning performance as function of the proton energy allowed us to make an extrapolation of the inefficiency up to the design energy: the outcomes give a first idea of the behavior of the collimation system in terms of beam cleaning in the perspective of a future energy upgrade. The discrepancies between simulations and measurements can be taken as a guide to the expected uncertainty in other configurations.

Among the tasks of the collimation system is also the cleaning of off-momentum particles, i.e. particles with a large energy offset with respect to the ideal energy. When a particle travels in the ring, it loses continuously a very small fraction of its energy due to the emission of synchrotron radiation: therefore, a particle not captured by the RF system, drifts away from the beam centre and is eventually lost. To safely intercept these particles, a collimation insertion in the LHC is dedicated to the momentum cleaning. Even though the presence of off-momentum losses has so far not been considered as a performance limitation for the accelerator, measurements during the operation of the LHC have shown losses higher than expected also in the momentum insertion, which might pre-maturely induce radiation damage to warm magnets. An important aspect of our work, hence, has been to simulate off-momentum particles, driven into the momentum collimators by radiation damping losing energy turn by turn. From a first set of simulations at 7 TeV, the distribution of the losses on the different collimators around the ring has been shown. As expected, most of the losses are concentrated in the momentum collimators. Moreover, the impact distribution of the particle in that insertion has been obtained: the results shows that the interactions between the particles and the collimator mainly occurs in the first hundred micrometer depth in the material and in the first half length of the collimator jaw. All the impact coordinates have been made available to the another team at CERN to be used for further studies of radiation dose in the warm magnets and collimator material. This is an ongoing study. The results of this study will be an essential element in assessing the effectiveness of new passive absorbers that could shield locally the warm magnets and increase their lifetime.

The high demands on required computing time of the performed simulations has been a limitation preventing to obtain large statistics. In a first attempt to speed up the simulation, a larger energy loss is applied to the particle as long as it is far away from the collimator jaws, and when the

---

distance has decreased down to a value given value, the small and realistic energy loss is used until the particle eventually hits the jaw. This new approach allows to run simulations with higher number of particles, gaining significantly in computing time. The obtained losses around the ring are in perfect agreement with the outcomes of the previous and slower simulation. Concerning the impact distribution on the collimators, instead, the new results deviate slightly from the longer simulation. Other proposals to improve the simulation method, left as future work, are under discussion.



---

# Bibliography

---

- [1] O. S. Brüning, P. Collier, P. Lebrun, S. Myers, R. Ostojic, J. Poole, and P. Proudlock (editors). LHC design report v.1 : The LHC main ring. *CERN-2004-003-V1*, 2004.
- [2] R.W. Assmann. Collimators and Beam Absorbers for Cleaning and Machine Protection. *LHC Project Workshop - 'Chamonix XIV'*, page 261, 2005.
- [3] R.W. Assmann *et al.* The Final Collimation System for the LHC. *Proc. of the European Particle Accelerator Conference 2006, Edinburgh, Scotland*, page 986, 2006.
- [4] F. Schmidt. SixTrack. User's Reference Manual. *CERN/SL/94-56-AP*, 1994.
- [5] M. Martini. An introduction to transverse beam dynamics in accelerators. *CERN/PS 96-11*, 1996.
- [6] M. Sands. The physics of electron storage rings. *SLAC report 121*, 1970.
- [7] H. Wiedermann. *Particle Accelerator Physics*. Springer, 3rd edition, 2007.
- [8] K. Wille. *The Physics of Particle Accelerators, an introduction*. OXFORD University Press, first edition, 1996.
- [9] S. Baird. Accelerators for pedestrians. *CERN-AB-Note-2007-014 OP*, 2007.
- [10] G. Robert-Demolaize. *Design and Performance Optimization of the LHC Collimation System*. PhD thesis, Universite Joseph Fourier, Grenoble, 2006.
- [11] C. Bracco. *Commissioning Scenarios and Tests for the LHC Collimation system Resistive transition and protection of LHC superconducting cables and magnets*. PhD thesis, EPFL Lausanne, 2008.
- [12] A. Piwinski. The Touschek effect in strong focussing rings. *DESY 98-179*, 1998.

## BIBLIOGRAPHY

---

- [13] <http://lhc-collimation-project.web.cern.ch/>.
- [14] Passage of particles through matter. The Review of Particle Physics: 2005 Reviews Tables and Plots, Particle Data Group web page ”<http://www.test.org/doi/>”.
- [15] Glenn F. Knoll. *Radiation Detection and Measurement*. John Wiley and Sons Inc, 4rd edition, 2010.
- [16] H.A. Bethe. Moliere’s theory of multiple scattering. *Physical Review* 89, pp.1256-1266, 1953.
- [17] Cern - the search for the higgs boson. <http://home.web.cern.ch/about/physics/search-higgs-boson>.
- [18] Cern - towards a superforce. <http://home.web.cern.ch/about/physics/unified-forces>.
- [19] LHC project. <http://lhc-proj-qawg.web.cern.ch/lhc-proj-qawg/LHCQAP/Instructions/MS-TD-guide.html>.
- [20] ATLAS Collaboration. The ATLAS experiment at the CERN Large Hadron Collider. *JINST*, (3):S08003, 2008.
- [21] CMS Collaboration. The CMS experiment at the CERN LHC. *JINST*, (3):S08004, 2008.
- [22] LHCb technical proposal. *CERN/LHCC 98-4, LHCC/P4*, 1998.
- [23] ALICE Collaboration: F. Carminati, P Foka, P Giubellino, A Morsch, G Paic, J-P Revol, K Safarik, Y Schutz, and U. A. Wiedemann (editors). Alice: Physics performance report, volume i. *Journal of Physics G: Nuclear and Particle Physics*, 30(11):1517–1763, 2004.
- [24] <http://inspirehep.net/record/1222129/plots>.
- [25] W. Scandale. Crystal collimation as an option for the lhc. *Proceedings of International Conference on Charged and Neutral Particles Channeling Phenomena, Frascati, Italy*, 2006.
- [26] D. Mirarchi, V. Previtalli, S. Redaelli, W. Scandale. Layout for crystal collimation tests at the lhc. *Proceedings of IPAC13, Shanghai, China*, 2013.
- [27] J. Smith, R. Assmann, V. Previtalli, V. Shiltsev, A. Valishev. Prospect for integrating a hollow electron lens into the lhc collimation system. *Proceedings of the 23rd Particle Accelerator Conference PAC09, Vancouver, Canada*, 2009.

- 
- [28] J. Resta Lopez, R. Assmann, S. Redaelli, G. Robert-Demolaize, D. Schulte, F. Zimmermann, A. Faus-Golfe. An alternative non linear collimation system for the lhc. *LHC-Project-Report-939, proceedings of the European Particle Accelerator Conference EPAC06, Edinburgh, UK*, 2006.
- [29] T. Weiler et al. Beam cleaning and beam loss control. *Proceedings of Advanced Beam Dynamic Workshop on High-Intensity, High-Brightness Hadron Beams, Nashville, TN, US*, 2008.
- [30] G. Robert-Demolaize, R. Assmann, S. Redaelli, and F. Schmidt. A new version of sixtrack with collimation and aperture interface. *Proc. of the Particle Accelerator Conf. 2005, Knoxville*, page 4084, 2005.
- [31] T. Trenkler and J.B. Jeanneret. K2, a software package evaluating collimation systems in circular colliders (manual). *CERN SL/94105 (AP)*, 1994.
- [32] R. Assmann, F. Schmidt, and F. Zimmermann. Equilibrium beam distribution and halo in the LHC. *Proc. of the European Particle Accelerator Conf. 2002, Paris, France*, page 1326, 2002.
- [33] S. Redaelli, R. Assmann, and G. Robert-Demolaize. Lhc aperture and commissioning of the collimation system. *Proceedings of the LHC Project Workshop Chamonix XIV*, 2005.
- [34] A. Fasso, A. Ferrari, J. Ranft, and P. R. Sala. FLUKA: a multi-particle transport code. *CERN Report CERN-2005-10*, 2005.
- [35] A. Fasso *et al.* The physics models of FLUKA: status and recent developments. *Proc. of the Computing in High Energy and Nuclear Physics 2003 Conf., La Jolla*, 2003.
- [36] G. Battistoni, S. Muraro, P. R. Sala, F. Cerutti, A. Ferrari, S. Roesler, A. Fasso, and J. Ranft. The fluka code: Description and benchmarking. *Hadronic Shower Simulation Workshop 2006, Fermilab 6–8 September 2006, AIP Conference Proceeding*, 896:31–49, 2007.
- [37] S. Redaelli, G. Arduini, R. W. Assmann, and G. Robert-Demolaize. Comparison between measured and simulated beam loss patterns in the CERN SPS. *Proc. of the European Particle Accelerator Conf. 2006, Edinburgh, Scotland*, page 1810, 2006.
- [38] R. Bruce, R.W. Assmann, V. Boccone, C. Bracco, M. Cauchi, F. Cerutti, D. Deboy, A. Ferrari, L. Lari, A. Marsili, A. Mereghetti, E.

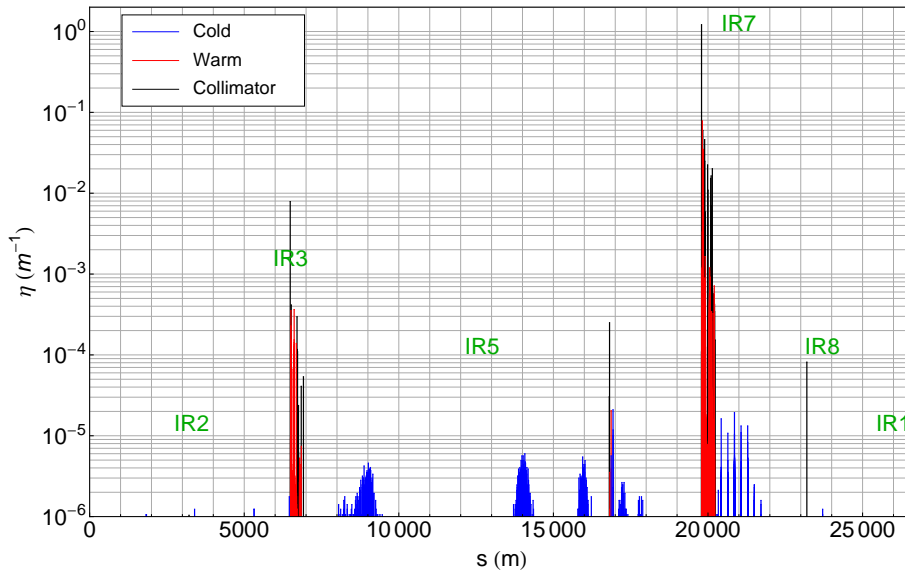
## BIBLIOGRAPHY

---

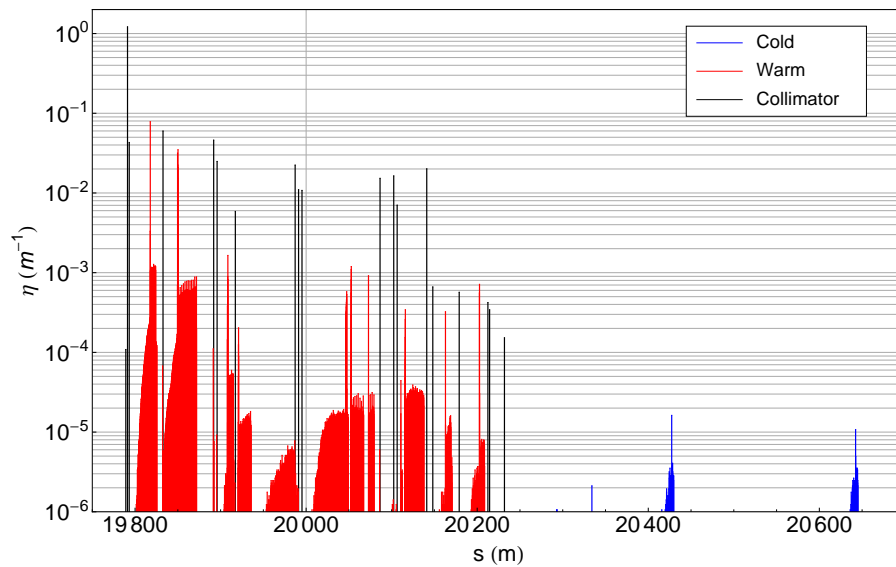
- Quaranta, S. Redaelli, G. Robert-Demolaize, A. Rossi, B. Salvachua, E. Skordis, G. Valentino, T. Weiler, V. Vlachoudis, D. Wollmann. Simulations and measurements of cleaning with 100MJ beams in the LHC. *Proceedings of IPAC13, Shanghai, China, 2013.*
- [39] R. Bruce, R.W. Assmann, and S. Redaelli. Principles for generation of time-dependent collimator settings during the LHC cycle. *Proceedings of IPAC'11, San Sebastian, Spain, 2011.*
- [40] R. Bruce and R.W. Assmann. LHC  $\beta^*$ -reach in 2012. *Proceedings of the 2011 LHC beam operation workshop, Evian, France, 2011.*
- [41] S. Redaelli R. Schmidt D. Valuch D. Wollmann M. Zerlauth W. Hofle, R. Assmann. Controlled Transverse of high-energy proton beams for aperture measurements and loss maps. *Proceedings of IPAC12, N. Orleans, USA, 2012.*
- [42] B. Dehning, E. Effinger, J. Emery, G. Ferioli, G. Guaglio, E. B. Holzer, D. Kramer, L. Ponce, V. Prieto, M. Stockner, C. Zamantzas. The lhc beam loss measurement system. *Proceedings of PAC07, Albuquerque, New Mexico, USA, 2007.*
- [43] R. Bruce *et al.* Collimator hierarchy limits: assumptions and impact on machine protection and performance. *LHC MPP workshop 2013, Annecy, France, 2013.*
- [44] A. Lechner A.Mereghetti E.Skordis, F. Cerutti. FLUKA energy deposition simulations for quench tests. *presentation in the LHC Collimation Review on March,30th 2013, 2013.*
- [45] B. Auchmann A. Verweij.
- [46] B. Salvachua, R. Bruce, M. Brugger, F. Cerutti, and S. Redaelli. Estimate of warm magnets lifetime in the betatron and momentum cleaning insertions of the LHC. *Proceedings of the International Particle Accelerator Conference 2013, Shanghai, China, 2013.*
- [47] F. Cerutti. Considerations on warm magnet measured doses. *presentation in the LHC Collimation Working Group, 2011.09.03., 2011.*
- [48] E. Chapochnikova. Longitudinal motion of uncaptured particles in the LHC at 7 TeV.

## Appendix A

This appendix contains the loss maps for Beam 1 simulated by SixTrack at selected energies during the LHC energy ramp. The parameters used for the simulations are discussed in Section 5.1.

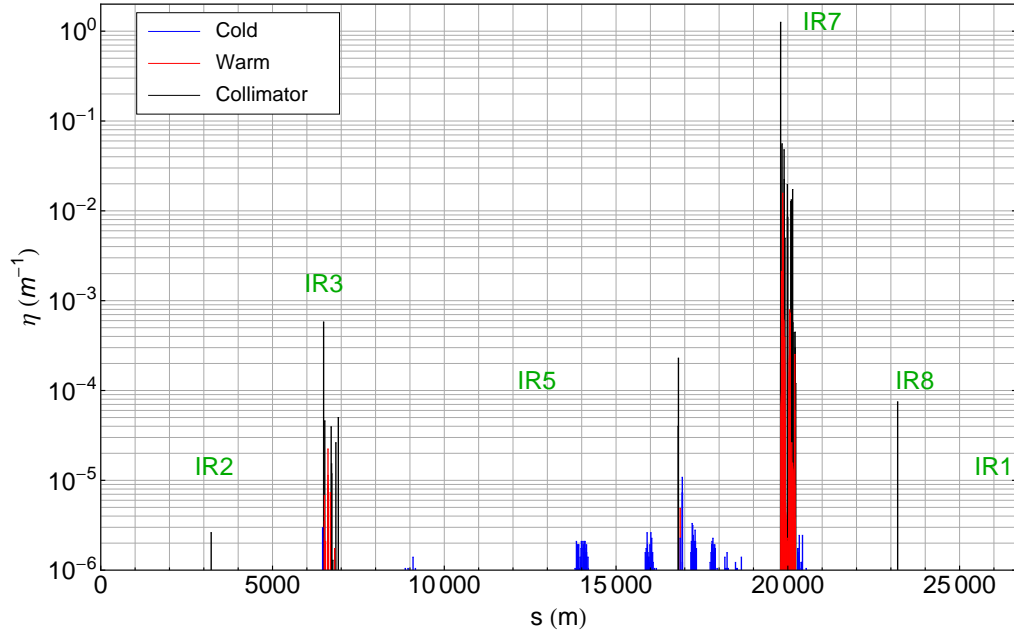


(a) Full ring

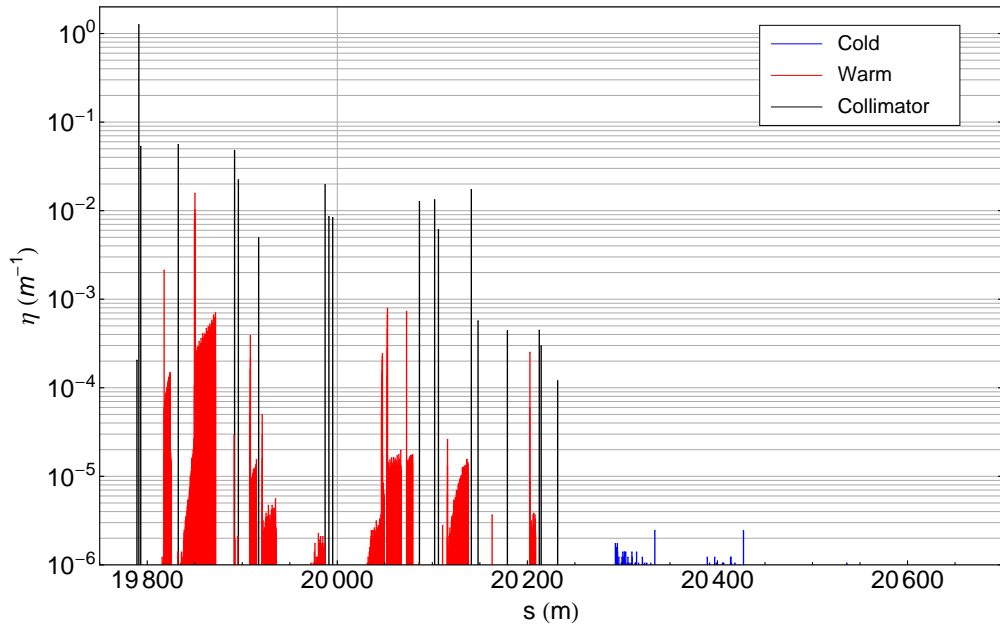


(b) Betatron cleaning insertion IR7

Figure 7.1: Simulated beam loss map at 450 GeV for Beam 1 in the horizontal plane.

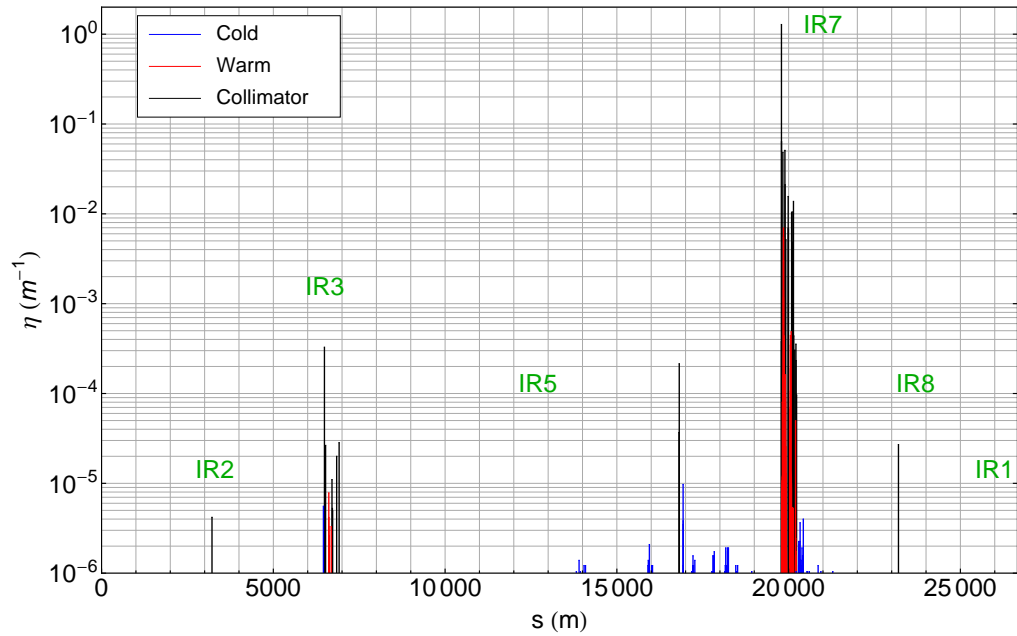


(a) Full ring

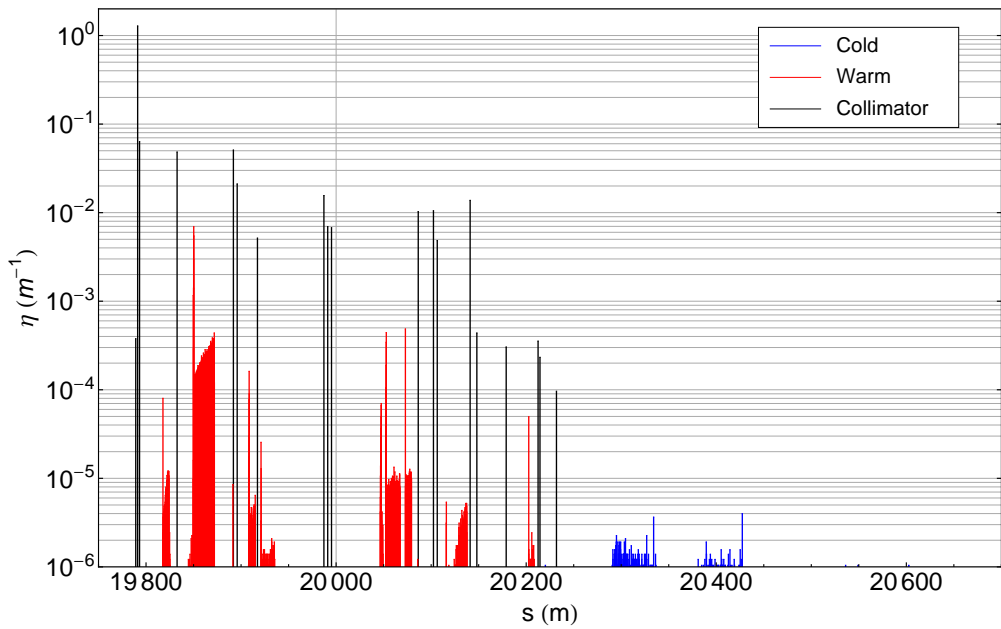


(b) Betatron cleaning insertion IR7

Figure 7.2: Simulated beam loss map at 1 TeV for Beam 1 in the horizontal plane.

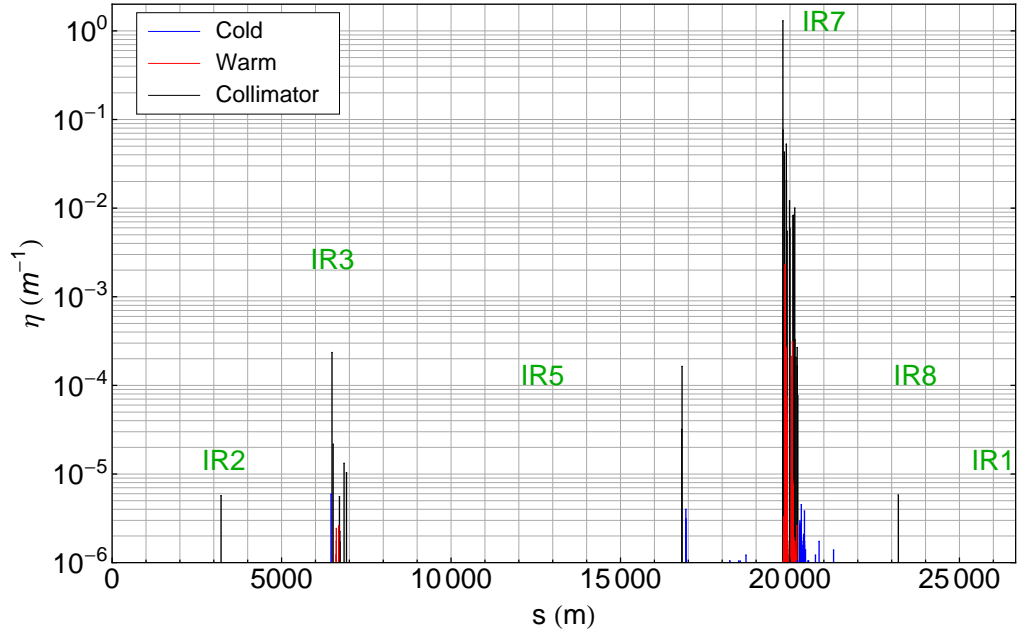


(a) Full ring

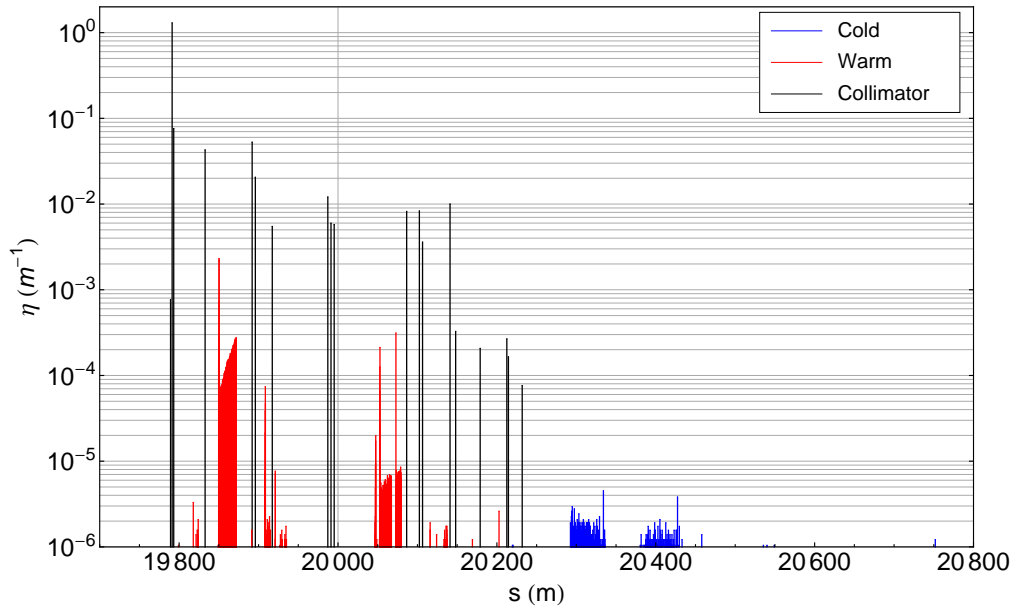


(b) Betatron cleaning insertion IR7

Figure 7.3: Simulated beam loss map at 1.5 TeV for Beam 1 in the horizontal plane.

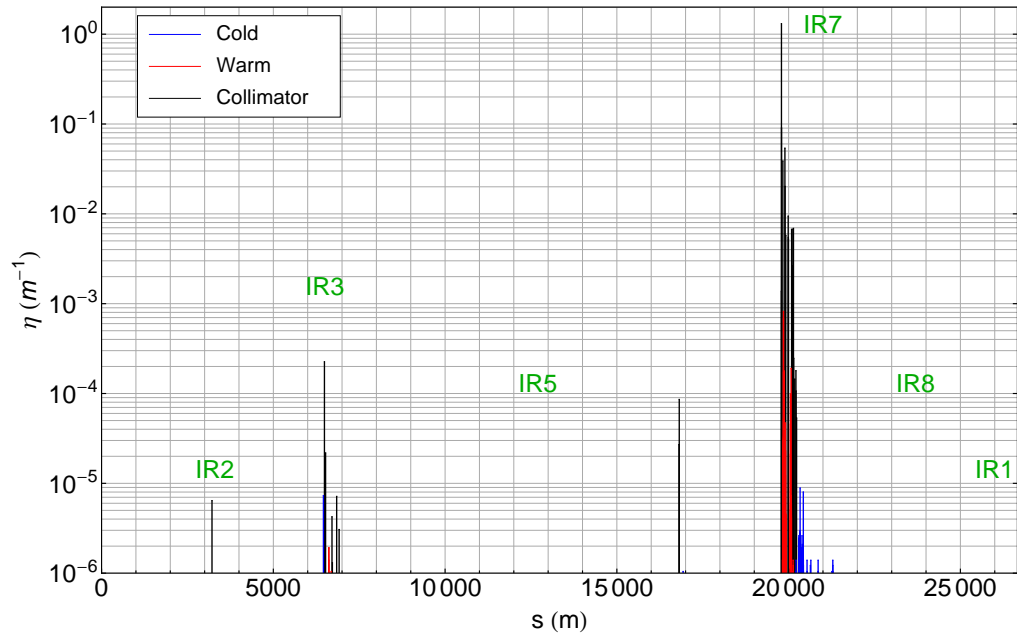


(a) Full ring

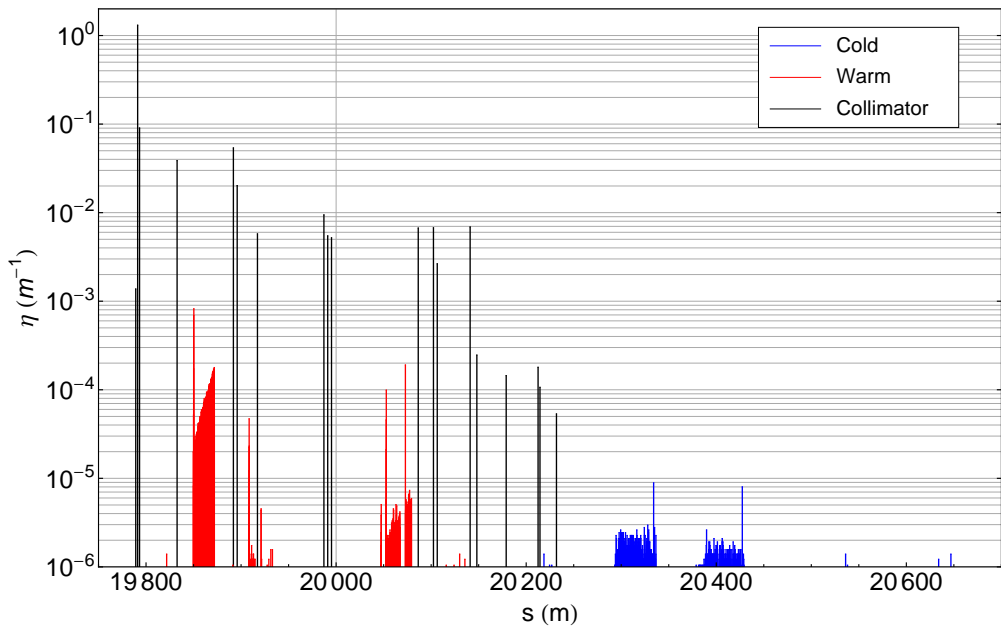


(b) Betatron cleaning insertion IR7

Figure 7.4: Simulated beam loss map at 2 TeV for Beam 1 in the horizontal plane.

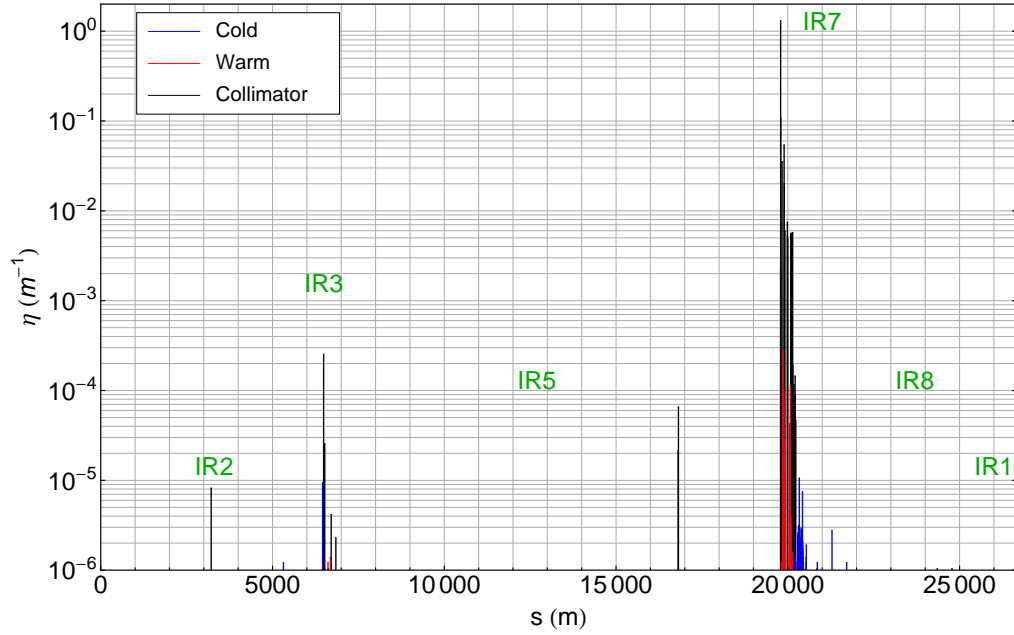


(a) Full ring

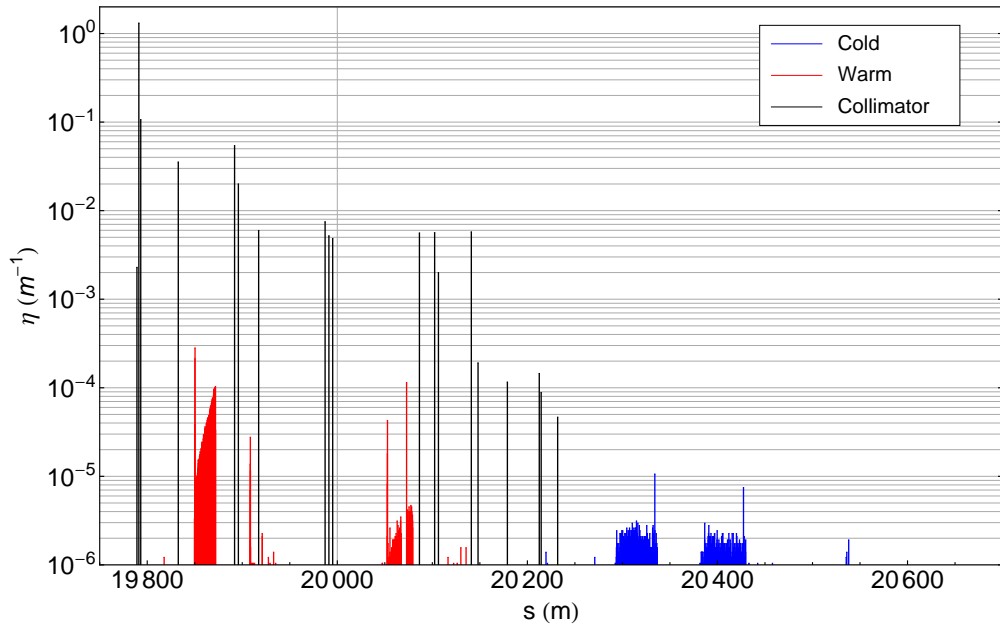


(b) Betatron cleaning insertion IR7

Figure 7.5: Simulated beam loss map at 2.5 TeV for Beam 1 in the horizontal plane.

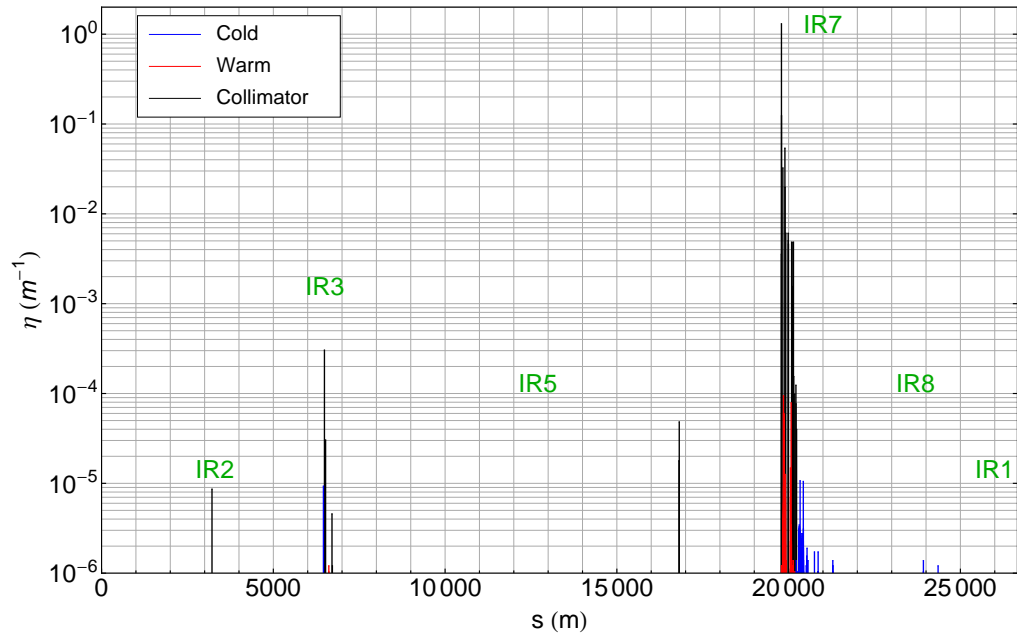


(a) Full ring

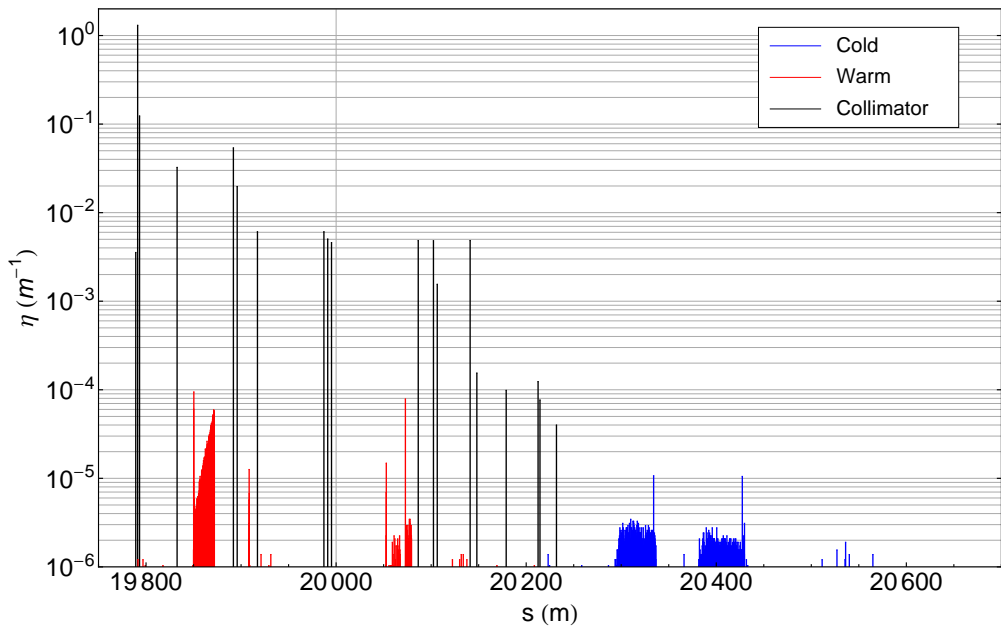


(b) Betatron cleaning insertion IR7

Figure 7.6: Simulated beam loss map at 3 TeV for Beam 1 in the horizontal plane.

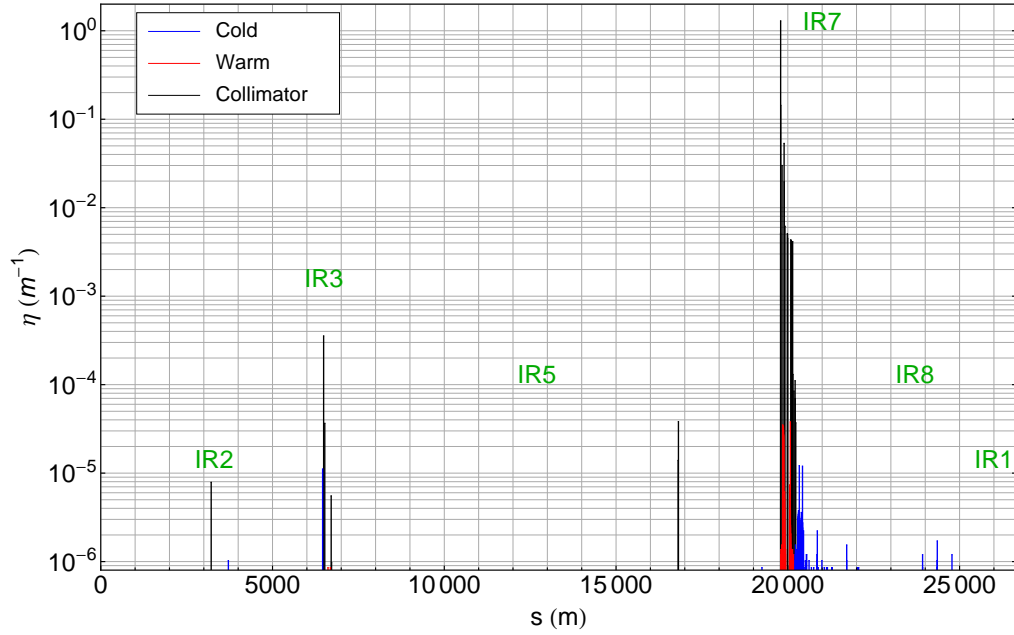


(a) Full ring

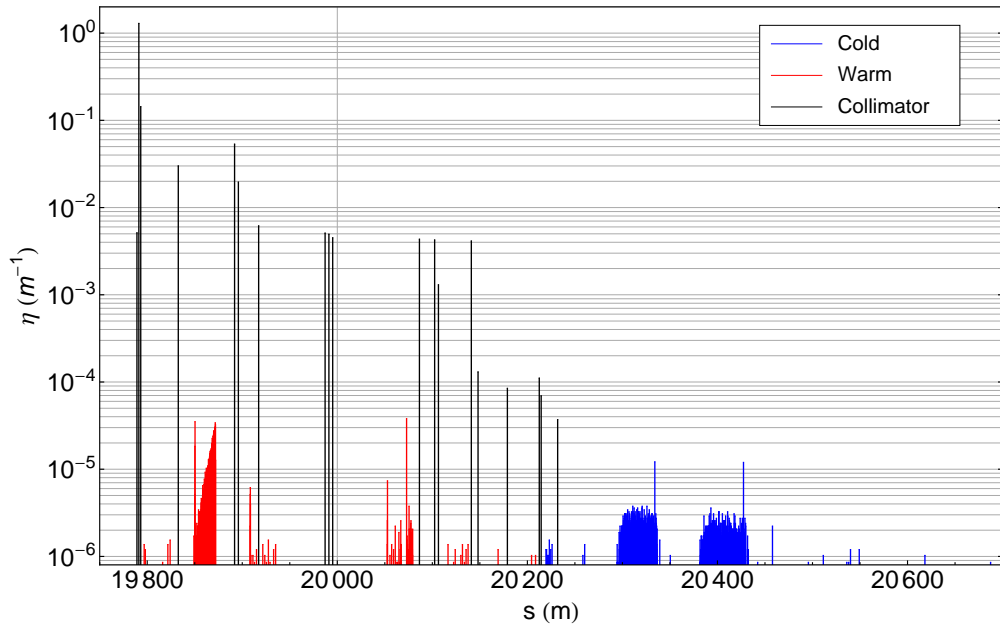


(b) Betatron cleaning insertion IR7

Figure 7.7: Simulated beam loss map at 3.5 TeV for Beam 1 in the horizontal plane.



(a) Full ring



(b) Betatron cleaning insertion IR7

Figure 7.8: Simulated beam loss map at 4 TeV for Beam 1 in the horizontal plane.

## Appendix B

This appendix contains the loss maps obtained from the BLMs signal recorded during measurements of provoked beam losses in the LHC energy ramp in November 2012. The data refers only to Beam 1.

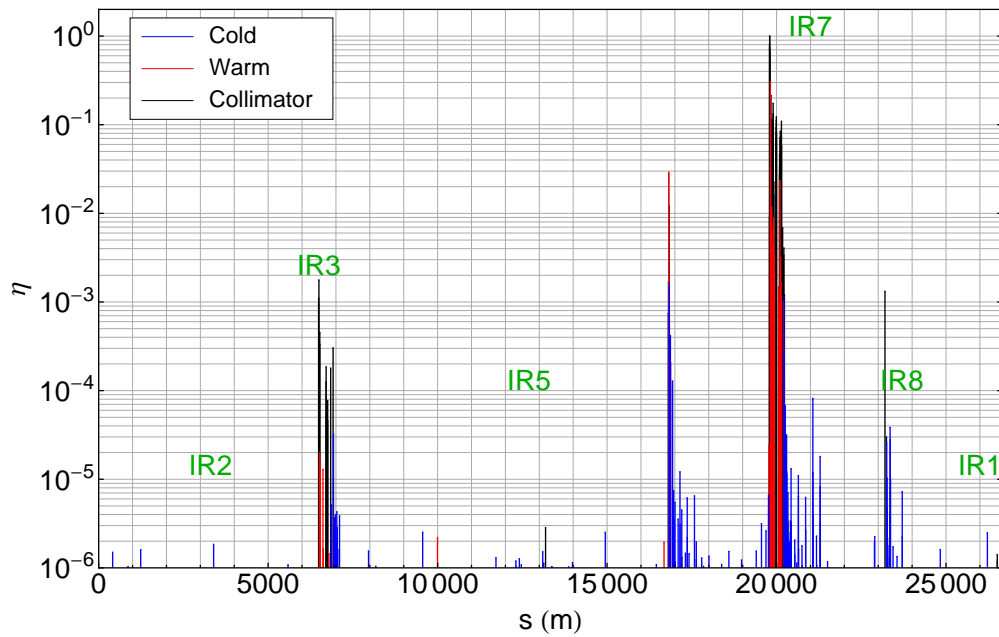


Figure 7.9: Measured beam loss map at 450 GeV for Beam 1 in the horizontal plane.

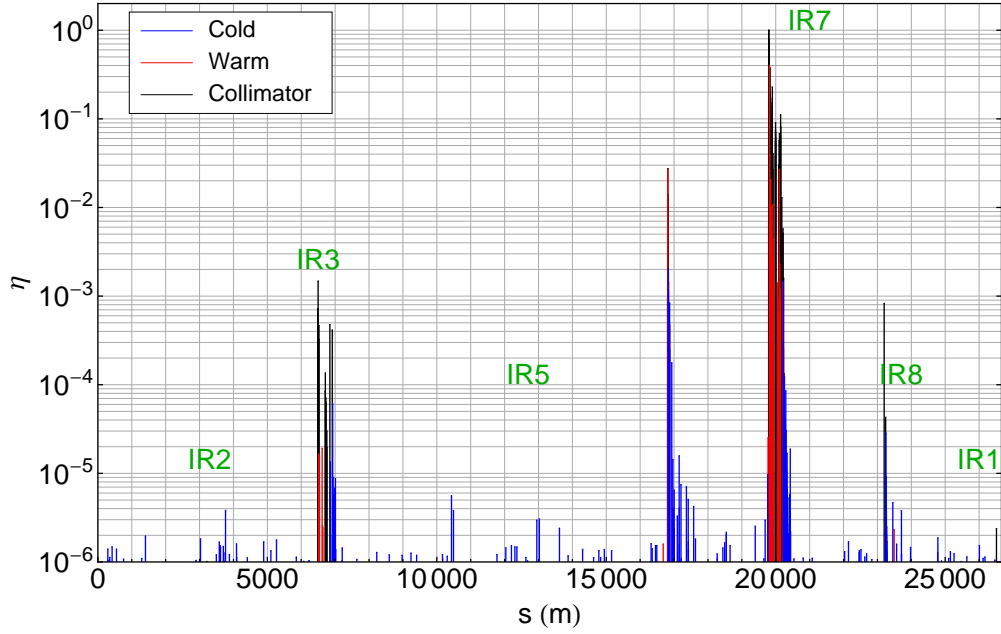


Figure 7.10: Measured beam loss map at 1 TeV for Beam 1 in the horizontal plane.

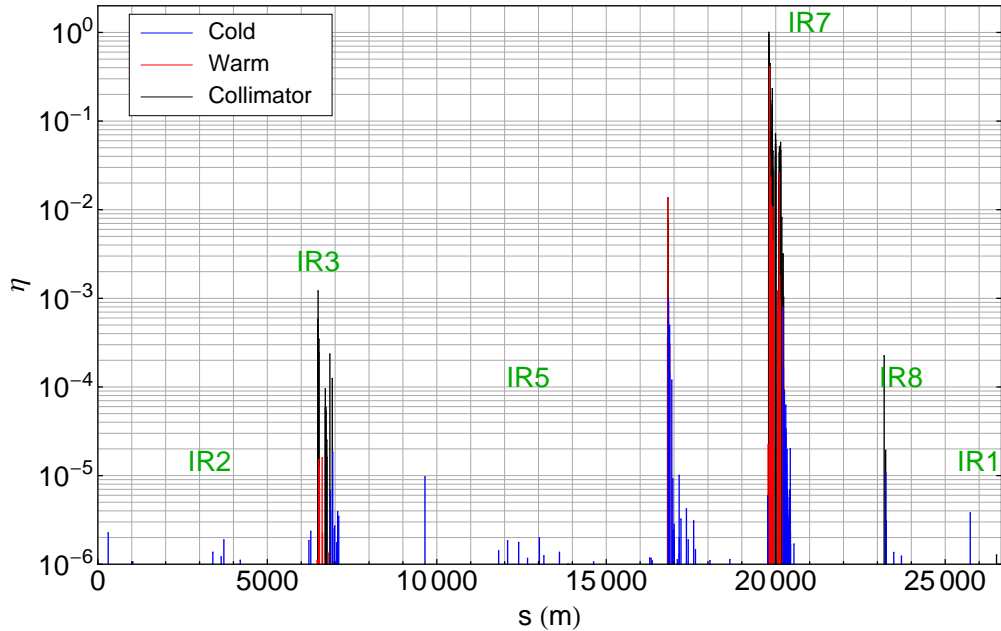


Figure 7.11: Measured beam loss map at 1.5 TeV for Beam 1 in the horizontal plane.

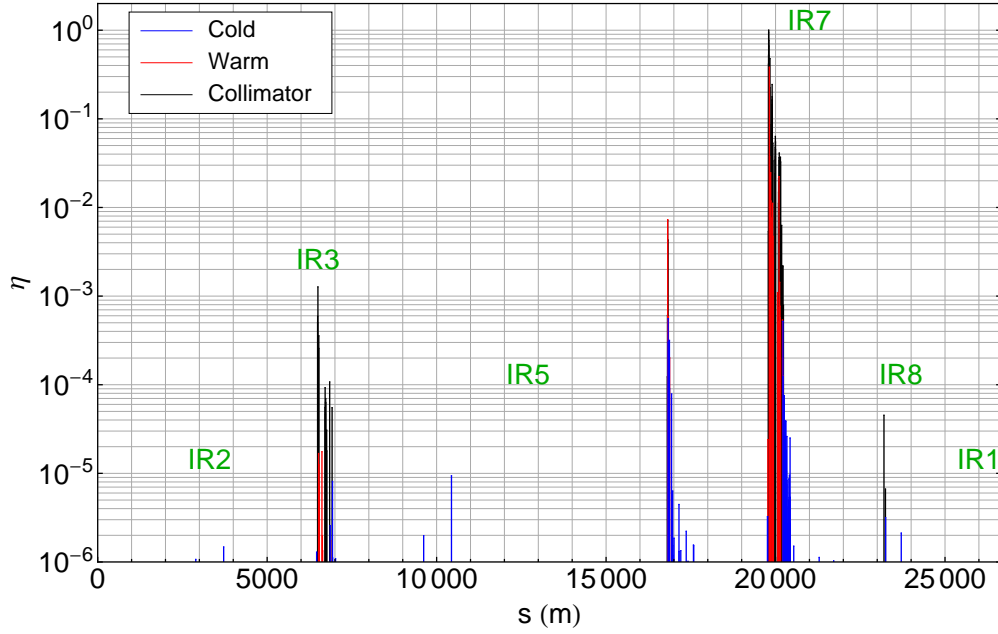


Figure 7.12: Measured beam loss map at 2 TeV for Beam 1 in the horizontal plane.

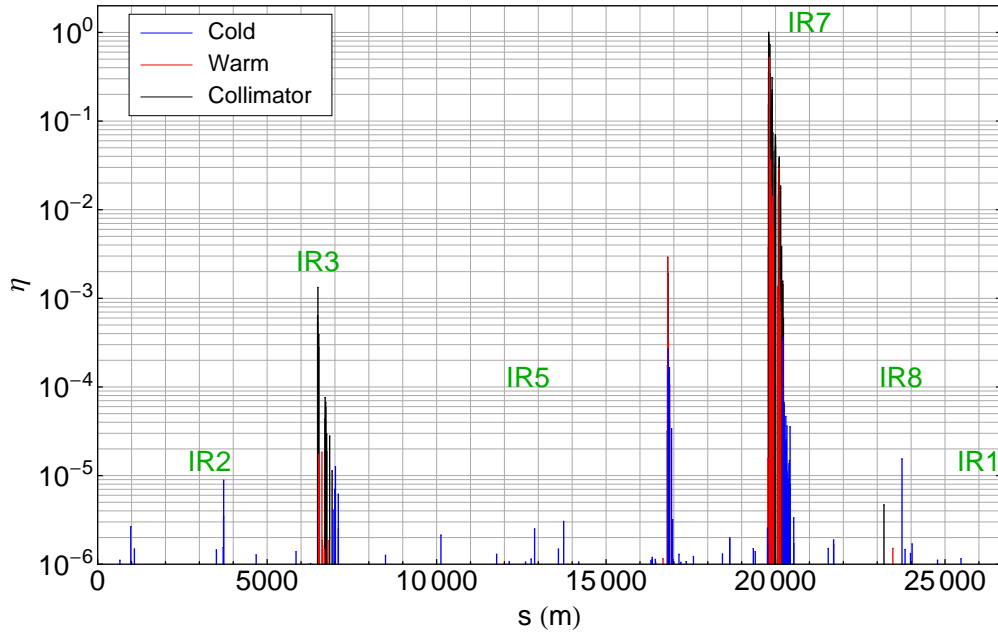


Figure 7.13: Measured beam loss map at 2.5 TeV for Beam 1 in the horizontal plane.

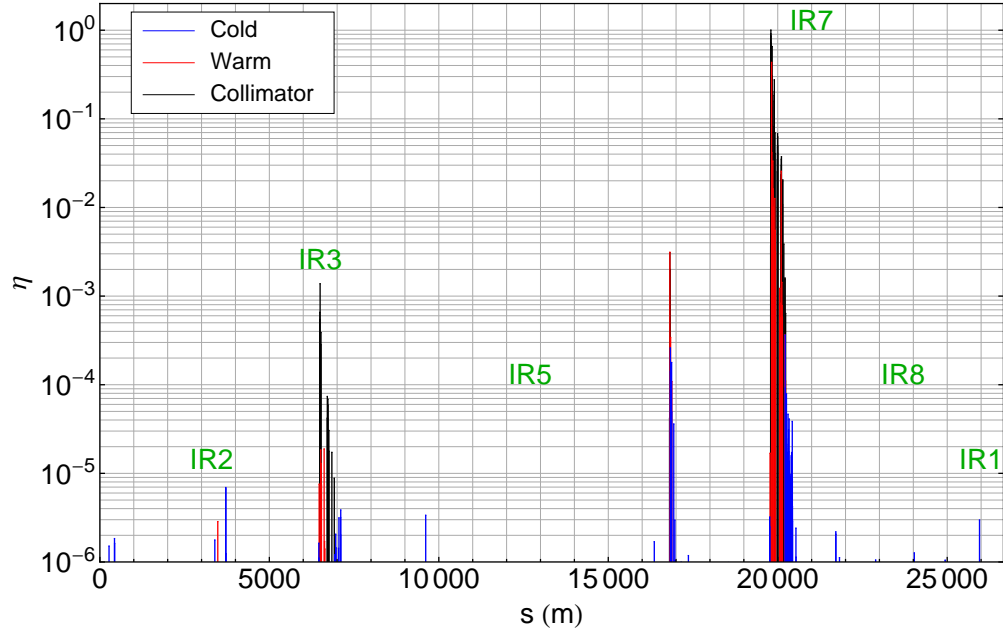


Figure 7.14: Measured beam loss map at 3 TeV for Beam 1 in the horizontal plane.

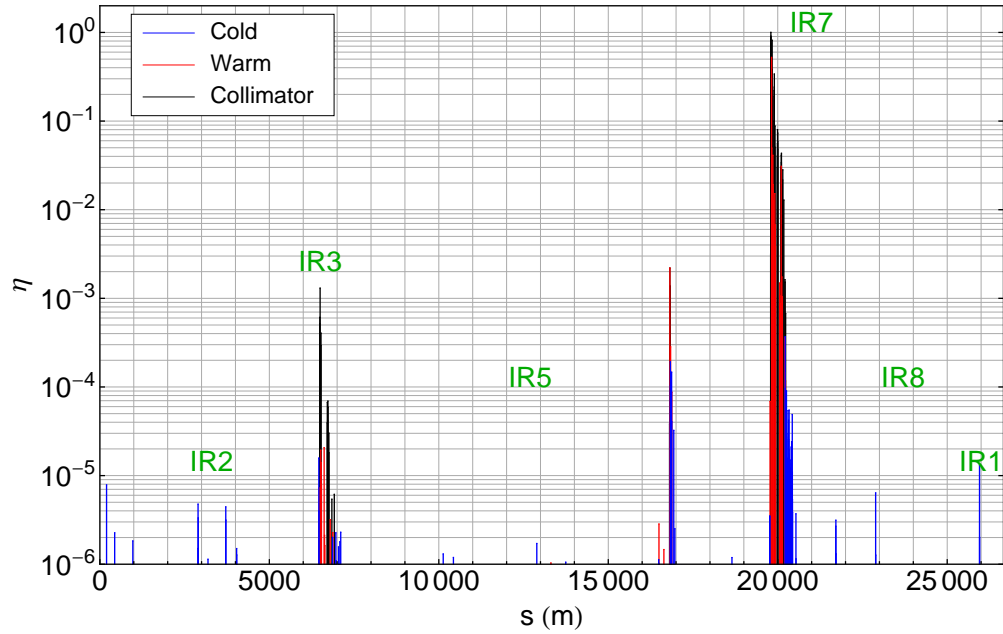


Figure 7.15: Measured beam loss map at 3.5 TeV for Beam 1 in the horizontal plane.

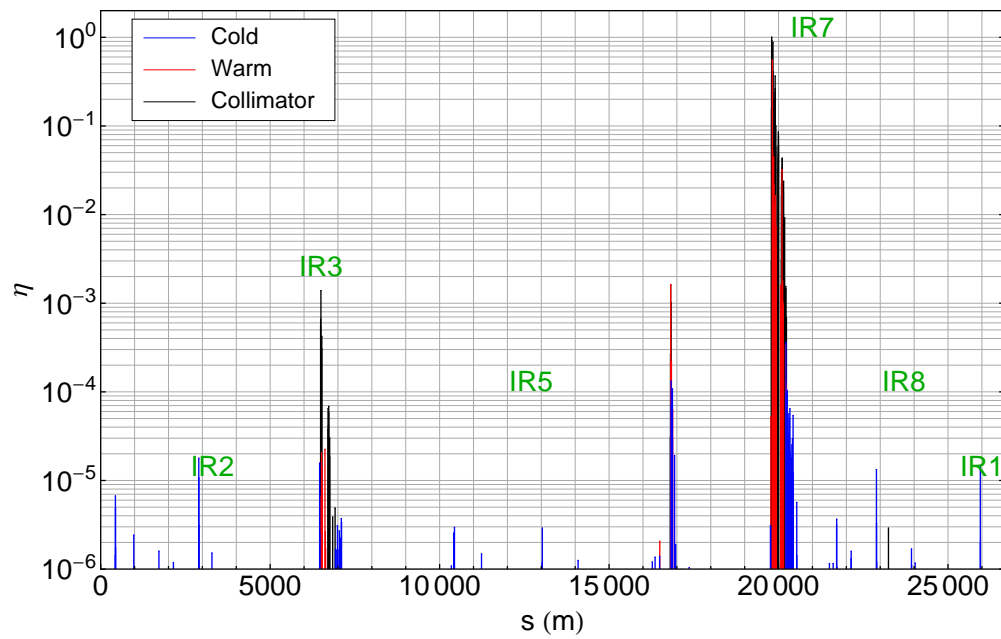


Figure 7.16: Measured beam loss map at 4 TeV for Beam 1 in the horizontal plane.

BIBLIOGRAPHY

---

# Acknowledgement

---

... and now it is time to thank all those have made this work possible.

It is surely my supervisor at Cern, Roderik Bruce, the main person to whom my warmest thanks are addressed. When my adventure at Cern began just over a year ago, I was certainly not an expert in the field of accelerators, but Roderik has been able to take me by the arm and with patience, devotion and a strong passion for his work, he taught me all the secrets of this world quite unknown for me so far. The path was plenty of difficulties, but his presence was always reassuring to me: he saw my tears, my smiles and eventually he spent many nights to revise my thesis. So I guess the best way for me to thanks him is to do it in his language: tack såmycket!

Many thanks to my professor Stefano Agosteo, who accepted to follow me in this experience.

Special thanks also to Stefano Redaelli, the leader of the LHC collimation project: it is mainly thanks to him that the doors of the collimation team slid open for me. I found there an international and friendly family, professional during the work time, but also able to have fun after leaving the office. Furthermore, a great thanks is addressed also to my Italian officemates, Tatiana e Daniele, who always helped me to solve problems and answer hundreds of questions.

Now, international readers please do not be offended if I switch in Italian because the thesis is just the top of a large pyramid which many people have contributed to build over time.

È innanzitutto grazie alla mia famiglia che ho potuto raggiungere la cima della piramide. Seppure a tanti chilometri di distanza, mamma, papà e nonni mi hanno permesso di porre solide fondamenta alla base e, con amore, forza e tanto tanto sudore, mi hanno aiutato nella costruzione aggiungendo un prezioso mattoncino ogni giorno.

Certamente dietro una grande opera c'è sempre anche l'aiuto di un bravo ingegnere. Quindi un grazie lo devo a Federico, con cui ho percorso un lungo e bellissimo viaggio: ha fatto scoprire ad una salentina quanto di bello possa esserci nel cuore di un "polentone".

Devo anche ringraziare il mio team di ingegneri nucleari (o, se preferite, "nucleari"), Antonio, Andrea, Federica, Edoardo, Marta e Lorenzo, con cui ho condiviso ore di lezioni infinite, nervosismi pre e festeggiamenti post-esame.

L'arrivo a Ginevra ha sicuramente dato una volta alla fase di costruzione della piramide: ogni persona che ho incontrato mi ha dato un forte slancio

## ACKNOWLEDGEMENT

---

verso il raggiungimento della vetta. Sin da subito ho conosciuto “lo zio” Vincenzo e la sua costiera (meh!), alla cui pazienza anche l’impaginazione di questa tesi deve molto, e di lì a poco “la zia” Claudia, a cui devo dire grazie per il suo costante supporto, ma soprattutto devo chiedere scusa per tutte le volte che si è fatta carico delle mie incertezze e paranoie. Ovviamente, parlando di zii, non posso certo dimenticarmi di zio Giorgino che sa sempre sorprendere trovando nel suo cilindro la soluzione ad ogni problema. Grazie a Davidone e Robertone, pur se momentaneamente in trasferta. E se temevo di sentire la mancanza del calore mediterraneo in questa città circondata da laghi e montagne, l’arrivo di Giorgia mi ha fatto tornare a respirare un po’ d’aria di casa. Grazie anche a te, Roberto, per tutte le nostre chiacchierate, le prove di pasticceria e per avermi fatto scoprire la torta al pistacchio. Un ringraziamento speciale va senza dubbio a Davide, che mi ha insegnato come la grinta nella vita sia un ingrediente fondamentale per raggiungere ciò che si vuole.

Et pour finir, un immense merci à Christiane, Enès, Shaina et Bobol: ma “famille genevoise” qui m’a toujours encouragé pendant la montée vers le haut de la pyramide.

---